Modelling Extended Defects in Neutron Irradiated Graphite

Submitted by

James Boone

to the University of Sussex as a thesis for the degree of
Doctor of Philosophy in Chemistry in the School of Life Sciences

I certify that all the material in this thesis which is not my own work has been identified and that no material is included for which a degree has previously been conferred on me.

Acknowledgements

The author would like to express their gratitude to EDF energy for funding the work presented in this thesis.

Thanks are owed to my supervisor, Prof. Malcolm Heggie for his continued support and informative scientific discussions regarding the radiation damage model in graphite, to whom I wish the best of luck in their new post. Thanks are also due to Dr. Chritopher Latham for his unparalelled knowledge of the computing system and LaTeX.

The time at Sussex during this DPhil has been made an enjoyable one by all of the colleagues in room 3R513, affectionately known as "The play room".

I would also like to dedicate this thesis to my parents Peter and Alison, and my brother Richard who have always been there to offer moral support.

Abstract

This thesis is a contribution towards modelling extended defects in nuclear graphite. Programmatic tools have been created which allow the implementation of displacement fields for basal and prismatic dislocations in graphite using the anisotropic elastic equations. These dislocation displacements have also been used to accommodate other defects which may be represented using dislocation formalisms. Structures such as prismatic loops, dislocation dipoles, folds, surface ridges and turbostratic graphite have been created for the purpose of generating structures for modelling.

We have investigated the X-ray diffraction simulations resulting from the various structures containing defects and compared these directly with experimental results from samples of neutron irradiated graphite. We have shown that some of the line defects, such as the ruck and tuck fold, reproduce characteristic diffraction phenomena as seen in the literature, providing evidence for the existence of such defects in the relevant temperature range. Powder diffraction patterns also show diffraction peaks at small angles, in line with what is expected from long range disorder. With the use of molecular modelling software with interatomic potentials, we have shown that the spiro interstitial defect, which binds adjacent layers, may not be a sufficient barrier to prevent the glide of partial basal dislocations past one another, especially when the shear constant for graphite is reduced by the presence of disregistry or stacking faults. In addition, we have shown that basal dislocations with large Burgers vectors (superedge dislocations) give rise to delamination across the glide plane, whereas a 90° partial basal dislocation does not.

Finally we treat graphene as a continuum membrane, performing calculations of the formation energy due to free bending, and compared the results for the nanotube with Density Fucntional Theory (DFT) calculations with good agreement. As such, the same method has been applied to other, more exotic structures for layer deformations, such as a buckles, folds and a wave packet like structure representing a local ripple in a layer, thought to occur when dislocation motion is inhibited and in-plane strain is relieved as out-of-plane deformations.

Contents

Chapter 1

Introduction

Graphite structure and bonding

Graphite is an anisotropic, layered material and is the most stable form of carbon. The structure of graphite crystals was first investigated by Hull in 1917 [1] without conclusive results, and later the hexagonal, layered nature was proposed by Bernal in 1924 [2]. Individual layers of graphite, now referred to as graphene sheets, are comprised of carbon atoms arranged in a tesselating hexagonal array. The bonds between atoms in each layer are hybridised sp^2 bonds, comprised of s, p_x and p_y orbitals leaving the p_z orbital normal to the basal plane, the lobes of which contribute to the π bonds between adjacent carbon atoms, further strengthening the in-plane bonding. The forces binding layers together are less well understood but a combination of π system overlap and Van der Waals attraction is currently the most accepted theory [3]. The layers of graphite stack upon one another in such a fashion that creates two unique lattice sites. One atom site lies directly above another, denoted an α atom, and the other is located above the centre of a hexagon, a β atom. This stacking configuration is denoted AB stacking, the most stable and hence, lowest in energy (fig. 1.1). The smallest irreducable unit of graphite is a cell that contains four atoms, two for each layer. The three vectors

that define the unit cell of graphite are $\mathbf{a_1}, \mathbf{a_2}$ and $\mathbf{c}$. The angle between $\mathbf{a_1}$ and $\mathbf{a_2}$ is 120°, and the $\mathbf{c}$ parameter defining the interlayer distance is orthogonal to both of these. The length of each of the vectors are $a_1 = a_2 = 0.244$ nm and $c = 0.68$ nm [2]. The nearest neighbour bond length between carbon atoms is 0.142 nm.

Although AB stacking is the predominant stacking formation, there exists other possible configurations such as AA, ABC (also known as rhombohedral) and turbostratic. AA graphite is the least stable structure and consists of all the atoms in one layer located directly above and below atoms in adjacent layers. Turbostratic graphite involves a relative rotation between layers. This rotation induces a stacking landscape in which the stacking configuration varies throughout the layer creating regions ranging from close to AA and close to AB like [4]. The bonds between the carbon atoms that make up the individual graphene layers are substantially stronger than those binding the layers together. This contrast can be seen when considering the elastic constants, where the in-plane elastic constant, C_{11} is 1060 GPa compared with that of the c-axis, C_{33} which is about 36 GPa [5]. Any deviation from AB stacking decreases the strength of the bonding between layers resulting in a reduced elastic shear constant C_{44} from 4.5 GPa to almost zero [6]. This gives rise to unique mechanical properties, such as the ability to use graphite as a solid lubricant, taking advantage of the ease with which layers are able slide past one another.

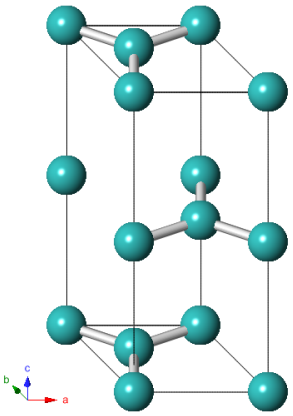

Figure 1.1: The primitive unit cell of AB stacked graphite

Allotropes of carbon

Allotropes of carbon include diamond, fullerenes, graphene and nanotubes (see figure 1.2), each of which have unique material properties. Diamond, which is colourless unless it contains defects or impurities [7], is comprised purely of sp^3 bonds and is the hardest known material, often used in industry as a cutting tool. It has an extremely high thermal conductivity and electrical resistivity. Synthetic diamond is readily made by a Chemical Vapour Deposition (CVD) process, which is more cost effective for some uses in industry than natural diamond. Nanotubes may also be grown by CVD, or a method called arc discharge [8, 9]. They have a huge tensile strength attributed to the very strong C-C bonds along their axis, their electrical properties vary with chiral vector [10]. The chiral vectors govern the tube radius and how tight the spiral of hexagons are along the tube. They also determine the shortest possible repeat length of the tube. The applications for nanotubes are currently being developed, with nanotube reinforced polymers being one area of focus, increasing material strength whilst adding negligible bulk [11].

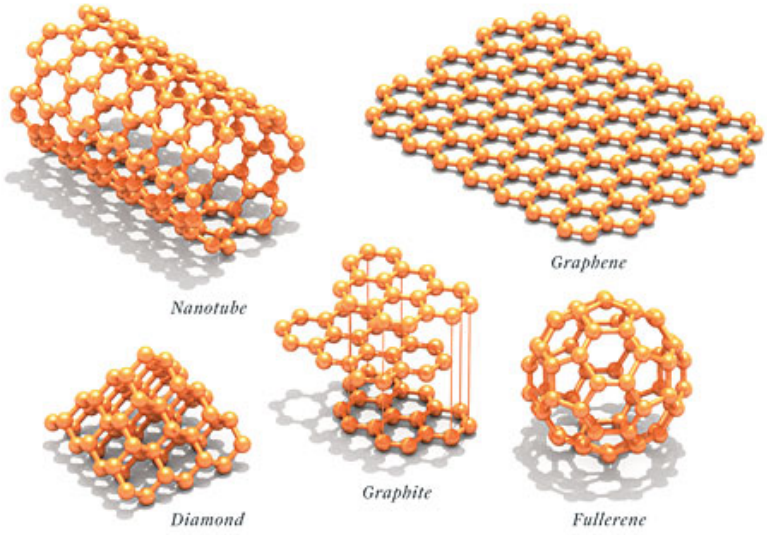

Figure 1.2: Allotropes of carbon. (Source http://spectrum.ieee.org/image/1721488)

Nuclear graphite

Many currently operating nuclear power stations (e.g. Hinkley point B in Somerset, an Advanced Gas-cooled Reactor (AGR) run by EDF energy) rely on graphite as a moderator of fast neutrons, as well as a structural component of the reactor core. The nuclear fission process generates high energy neutrons with typical energies of the order 1MeV [12]. High velocity neutrons have a long mean free path in the graphite due to their lack of charge and have to be slowed down considerably to maintain a chain fission reaction in the uranium fuel. This is achieved by enclosing the fuel rods in large graphite bricks. A series of inelastic collisions with the lattice cause the neutrons to impart their energy to the carbon lattice. However, this transfer of momentum to the graphite causes various mechanisms of damage to its structure. These forms of damage range from point defects like interstitial atoms to extended ones such as basal edge dislocations (see figure 1.3)[13]. The graphite in a reactor core is made from granular crystalline powder, mixed with pitch and filler. This gives the final material an isotropic nature and helps to prevent accentuating any one property change associated with the single crystal caused by irradiation. With such an important role in the reactor regarding both safety and power generation, the graphite degradation is carefully monitored and managed. One such property that is carefully monitored is the dimensional change. During the initial irradiation process, the graphite bricks shrink in size, where an increase in crystallite size is accommodated initially by small pores in the graphite bricks. This shrinkage of the bricks stops after a certain neutron fluence, when these small pores have closed, and the graphite begins to expand. The point at which this occurs is known as turnaround. The core is engineered to operate within a certain margin, and turnaround poses a concern because of the reversed direction of internal stresses.

Nuclear graphite is created by taking raw disordered carbon materials (coke) and using chemical and heat treatments to obtain the final polycrystalline product. A

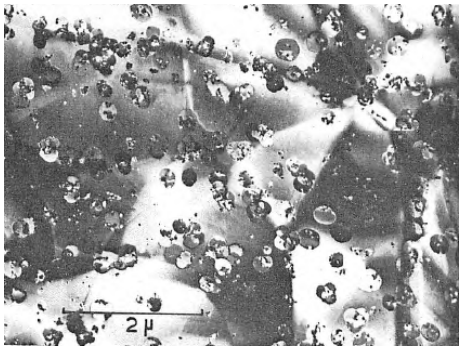

Figure 1.3: Interstital and vacancy loops shown in TEM of graphite irradiated at 1350^{o}C to 11.7x10^{20} neutrons cm^2. Image reproduced from [13]

combination of pitch, a complex mixture of polynuclear aromatics formed from heat treatment of coal tar or petroleum tar, and coke is heated and calcined, the process of removing volatile materials and moisture. The heating causes the material to form crystalline structures, and exposure to temperatures of up to 1500 K results in a material referred to as the "green article". At this point the green article is shaped into the desired form for the final nuclear graphite by a process of extrusion, where it is pushed through a die with specific dimensions. After this process the material is heated to drive off impurities and create a solid material. The gases that are driven off create channels and pores in the material, which have a detrimental effect to the structural rigidity of the final graphite. Additional pitch is introduced to fill these voids to ensure the final product is as structurally sound as possible. The final stage in creating the nuclear grade graphite is a heat treatment up to around 3500 K over a time period of many days. Finally, gas treatment at about 2300 K with a Halogen is performed to remove unwanted gases, for example the graphite may not have more than 10ppm of Boron impurity. The use of graphite in a power station as a neutron moderator automatically increases the material quality requirement for safety reasons. It is often used as a structural component in the core such as having fuel and cooling channels designed into the bricks [14]. It is therefore of very high importance to understand the behaviour of graphite as it is exposed to high energy neutron radiation.

Radiation damage in graphite

The standard model for radiation damage in graphite states that the collisions between neutrons and carbon atoms causes cascades of damage comprised of vacant atom sites and interstitial atoms. This collision process results in carbon atoms occupying regions between the planes of graphite causing expansion in the crystal's **c** direction. At higher temperatures, the theory attributes the aggregation into loops or clusters of these interstitials and vacancies to the dimensional change. The vacancies form lines, which are able to heal across their width accounting for some basal plane contraction. Various point defects have been observed in TEM micrographs of irradiated graphite. However, single crystals of graphite behave very differently when irradiated at temperatures either side of about 500 K, as reported by Kelly [15] (figure 1.4). There is a clear distinction between the low and high temperature regions in that the change in dimension of the **c** direction is dramatically greater when irradiation takes place below 500 K. The explanation provided by the standard model does not quantitatively account for the difference in these two regimes, implying that new theory and understanding is required to explain the phenomenon.

Self interstitials and vacancies are defects which are thought to play key roles in the behaviour of irradiated graphite and the subsequent property changes [16, 17, 13]. Interstitials have, in the past, been assumed to be non-interacting with surrounding material [18], but it is well known that isolated carbon atoms are a highly reactive species. Recent publications have employed more accurate modelling methods such as *ab initio* computations which show that, contrary to prior belief, the self interstitial in graphite bonds strongly between layers and has a much higher activation energy, around 1-2 eV [19, 20], an order of magnitude higher than previously thought [13]. The spiro interstitial, taking its name from the similarly shaped spiro-pentane molecule, is four-fold coordinated having bonds form with two atoms in each adjacent layer. The spiro interstitial is forced to bond with a 60°

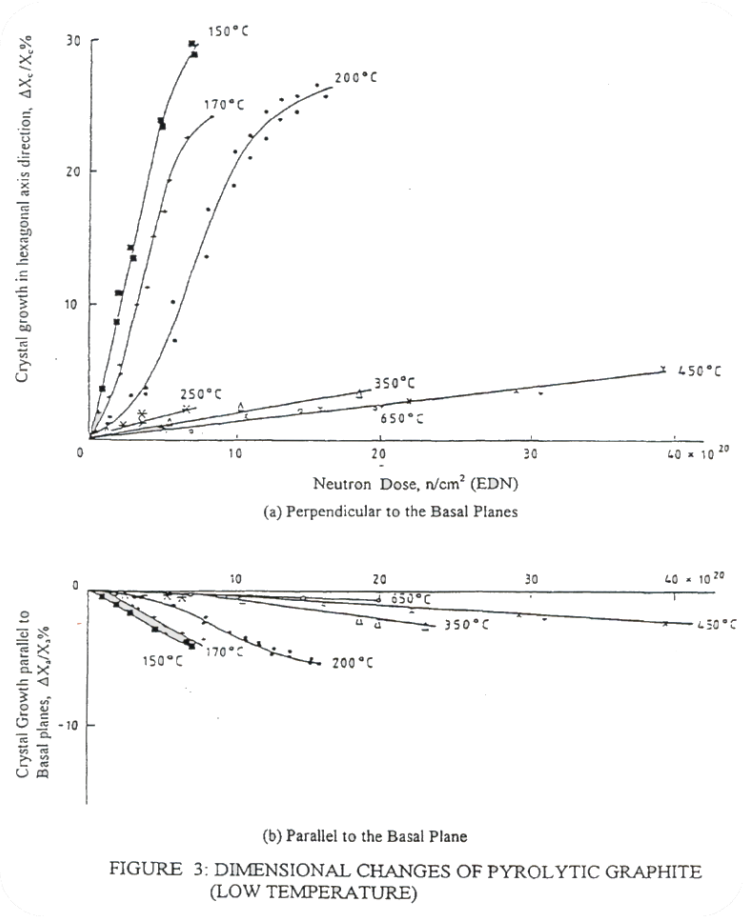

Figure 1.4: Graph showing the temperature dependence of dimensional change in neutron irradiated graphite. Of particular interest is the dramatic difference in dimensional change during irradiation either side of 200°C. Image reproduced from [15].

relative rotation between either end of the structure, complying with the relative angle between bonds forming the sides of hexagons in each layer. The prediction of a higher activation energy for the interstitial would rule out the possibility of the atoms being mobile at the temperatures in which large dimensional change takes place [15]. A graph from experimental data clearly showing this contrast in behaviour at different temperatures is shown in figure 1.4. In turn, this rules out the mechanism of new plane growth from the aggregation of carbon interstitials between the basal planes at low temperatures, an important process proposed by the current radiation damage model.

When defects such as interstitials and vacancies are created in a crystal by high energy collisions, the total energy of the system is raised because the resultant

structure is energetically less favourable. A common method by which defects may be removed from crystals is annealing, a process during which the material is heated up in an attempt to thermally overcome the activation barrier of defects, enabling them to return to a lower energy state. The energy from defect annihilation is expelled as heat from chemical bond formation and resulting thermal vibrations of the lattice. The amount of heat expelled depends on the concentration and nature of defects in the structure. In the case of the 1957 Windscale disaster, the graphite reached a critical temperature of about 500 K during operation, the thermal activation energy for migration of point defects [16], which generated enough heat to cause a runaway temperature increase and the fuel to catch fire.

A new model proposed by Heggie *et al.* introduces the concept of buckling and folding of graphite layers [21]. The hypothesis exploits the layered nature of graphite where defect motion is very much restricted to between the basal planes. It is thought that neutron irradiation induces buckling defects in the layers for the temperature range below 500 K, where interstitial atoms are immobile and stitch together the graphene sheets by bonding to atoms in adjacent layers. This stitching impedes the shear of layers past one another causing restricted motion of defects such as basal dislocations. The pinning and subsequent interaction of these dislocations deposits extra material locally in the layer, introducing internal stresses. Buckling and folding of layers is a much more favourable process than compressing or stretching surrounding planes to accommodate the added material. Individual layers of graphene have been shown to crumple and fold, creating stuctures much like the proposed ruck and tuck defect. The occurence of buckling and folding is extensive in many other fields of science, including organic membranes, rucks in a rug and geological phenomena [22, 23, 24]. For illustration, an image of this occurrence in rocks is provided in figure 1.5.

Figure 1.5: Recumbent folds of rock in Breinz, Switzerland. Image reproduced from [25]

Chapter 2

Modelling graphite systems with GULP

The General Utility Lattice Program (GULP) is a software package designed for simulating properties of materials. Its primary function has been as a means of structural optimisation of large graphite structures containing various defects. The reason for using GULP in conjunction with a molecular mechanics potential is due to the computational savings as compared to running higher level Density Functional Theory (DFT) calculations. Even though breakthroughs have been made in applying DFT techniques to increasingly large systems, calculations approaching 10^4 atoms are still computationally demanding [26]. It is thought that the use of a molecular mechanics potential for extended defects will reproduce the necessary physics at the scale of interest.

GULP has the ability to implement a wide range of potentials to cater for a variety of systems and levels of computational accuracy [27]. The potential which has been employed here for modelling extended defects in graphite is the combination of a set of harmonic potentials tuned to known parameters of graphite such as bond length and angle, whilst a Lennard-Jones governs the longer range inter-layer binding. The equilibrium bond length for the in-plane C-C bonds is 0.142 nm and

the angle between three nearest neighbours, 120°. The Lennard-Jones function containing the chosen parameters is shown in equation (2.1). The three-body interaction relates to bond-bond repulsion and bond angles. These are modelled using a harmonic potential which penalises for deviations from a given bond angle, as shown in equation (2.2).

$$E_{LJ} = 3.73E^{-3}\left[\left(\frac{3.71}{r_{ij}}\right)^{12} - \left(\frac{3.71}{r_{ij}}\right)^{6}\right] \tag{2.1}$$

$$U_{ijk} = \frac{1}{2}k(\theta - \theta_0)^2 \tag{2.2}$$

Where r_{ij} is the distance between atom i and atom j. U_{ijk} denotes the energy cost as a function of angle between atoms i, j and k. θ_0 is the equilibrium angle and θ is the measured angle.

GULP does not explicitly treat individual electrons in the system, but combines their effect into contributions from each atom. For molecular mechanics force fields, the coulombic interaction is subtracted for neighbouring interactions according to connectivity, such that parameters in two and three body potentials may be directly compared with observable quantities from experiment, such as bond length, bond angles and vibrational frequencies [27].

2.1 Molecular dynamics

A molecular dynamics (MD) simulation is a technique used to evolve a system over time subject to each atom being given an initial velocity and allowed to move according to the laws of classical Newtonian mechanics, constrained by the implemented potentials which govern the properties of the model. At the beginning of a simulation, each atom is allocated a random velocity. This velocity may be obtained from the Maxwell-Boltzmann distribution, where a particle i of mass m_i

has a certain probability of having a velocity v_{ix} in the x direction at a certain temperature T. The random velocity is typically chosen from a normal distribution with a mean $\langle x \rangle$ and variance σ^2. The probability of choosing a value x from this distribution is given by equation (2.3). The initial velocities are also adjusted along each direction, such that the net momentum of the system is necessarily zero.

$$p(x) = \frac{1}{\sqrt{2\pi\sigma^2}} \exp\left[-\frac{(x - \langle x \rangle)^2}{2\sigma^2}\right] \tag{2.3}$$

Once the initial velocities have been set, the force must be calculated at each step by differentiating the potential function. Once the model is initiated, the trajectory of the particles are evolved for a finite length of time. The amount of time the simulation needs to run to have sufficiently sampled available configurations is difficult to ascertain because an MD simulation has no final state due to thermal vibrations of the lattice. However, it has been used to allow the model to overcome small energy barriers due to corrugation and to allow some movement away from the interlayer equilibrium. MD has been used as a form of simulated annealing, allowing transitions over small but not negligible energy barriers in the potential energy surface, whereas a 0K optimisation may become stalled by local minima and result in a final state that does not properly represent a realistic structure. A finite temperature allows the system to access lower energy states.

2.2 Structural optimisation

After running MD simulations, the models were structurally optimised. Once the total internal energy of the system is calculated, the optimisation routine attempts to move atoms along paths in order to find successively lower minimum energy configuration. This minimum is unlikely to be the global minima of the system, as such a task is intractable for anything more than the most simple of

systems. At a given point in the structure, the energy may be expressed as a Taylor expansion. This expansion is often truncated at first or second order due to harmonic behaviour near a local minimum. The collection of second derivatives is used to construct the Hessian matrix, which stores information about the curvature of the local potential surface. The calculations presented here use the conjugate gradient optimisation routine, which only requires calculation up to the first order term of the Taylor expansion. Although the Broyden-Fletcher-Goldfarb-Shanno (BFGS) optimisation method is more efficient in reaching the final structure in fewer iterations because more information is known about the local potential energy surface, the computation and storage of the inverse Hessian matrix for many thousand atom systems can become a time and resource limiting procedure, especially if the system is far from an equilibrium state.

2.3 Partial dislocation dipoles

Partial dislocation dipoles were introduced into large supercells for the purpose of understanding how isolated dislocations behave in graphite. The dislocations employed here are 90 degree partials, the direction and magnitude of which are $\frac{1}{3}\{10\bar{1}0\}$, making them pure edge in character. The core width of a single 90° partial basal dislocation in graphite has been calculated to very wide, about 4nm [28]. Confinement to regions smaller than their core width is of interest with regard to the study of dimensional change, as dislocation motion can be hindered by the presence of other defects [29].

The first attempt to confine the dislocations was the use of single interstitial atoms bonded into adjacent layers across the slip plane of the dipole, effectively stitching them together. The simulations using a molecular mechanics potential would not allow bonds in the system to be changed (created or broken) from their initial state, hence the dislocations could not slip past the defect. Using an interstitial as a pinning point required a change to the specified interatomic

harmonic potential, because the spiro pentane like structure involves 60° bond angles, and an additional condition was added for the interstitial and the in-plane atoms involved in bonding to it. It was found that using the interstitial as a method for confining the dislocations allowed enormous dislocation sizes without the system showing signs of fracturing (see figure 2.1). An extreme case was implemented to test the model, in which twelve 90° partial dislocations were present at each core. To introduce such a large dislocations using the displacement field equations (3.24) and (3.25), a different method was required because of undesirable core distortions. For the case of large Burgers vectors generating undesirable core distortions, the Burgers vector was split up into equal parts and each of the smaller dislocations applied at equal intervals along the slip plane such that the large core was spread out over a wider region. After running the simulations, the distortions appeared confined to the two layers either side of the slip plane, which led to the conclusion that the method of pinning with interstitials was effectively only trapping the ends of each dislocation, leaving the rest to disperse throughout the cell. A visual explanation of this proposed occurrence is shown in figure 2.3. This did not produce the desired confinement of the dislocations and is thought to have occurred as a result of the Lennard-Jones potential underestimating the shear constant C_{44}. However, the value for C_{44} in graphite is small ($\sim$ 5 GPa) for a perfect crystal, and even lower between layers that have a disturbance to their registry.

A function in GULP allows the user to specify an instruction to hold desired atoms in place during MD or structural optimisation. After the failure of the use of interstitials to confine the dislocations over more than one layer, atoms residing in planes at the centre and edge of the cell were held fixed to prevent slip beyond half the cell width. This ensured that the undesired pinning of just two layers in the spiro-interstitial case did not take place.

The simulations performed here confine each dislocation to a width of approximately 5.2 nm, half the length of the unit cell. The locations of the dislocations within

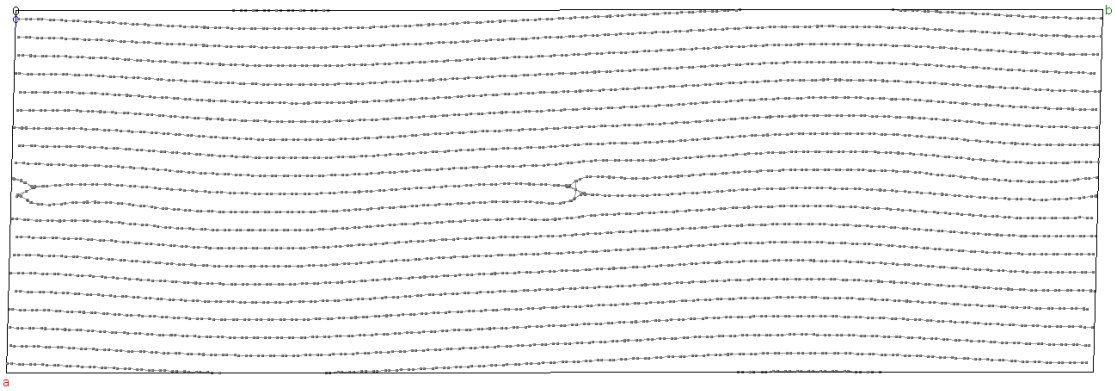

Figure 2.1: A dipole of twelve 90° partial basal dislocations in a large supercell. Final structure after optimisation shows buckled central layers, but relatively unperturbed surrounding layers. Figure 2.3 shows the full interpretation of the result using dislocation notation.

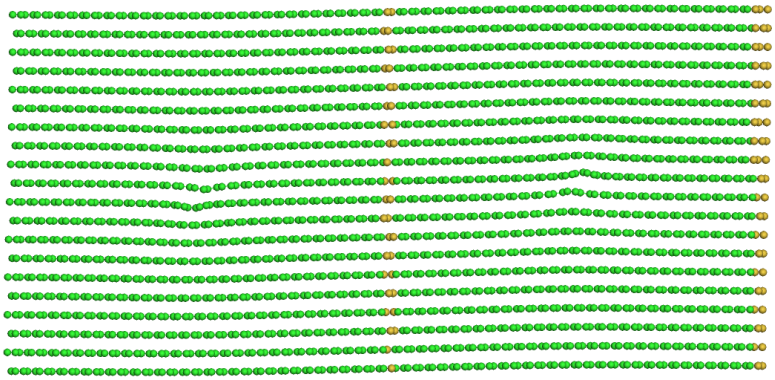

Figure 2.2: Initial structure containing basal dislocations $\mathbf{b} = 0.57$ nm ξ along $(10\bar{1}0)$. The fixed planes of atoms constraining the dislocations shown in orange.

the cell are such that they are separated by half the cell length from one another in the scheme of a super lattice (see figure 3.16). Two planes of atoms between the dislocations were frozen in place during optimisation runs to prevent the annihilation of dislocations with one another, or the structure would return to perfect AB stacked graphite upon an MD run. Several sizes of dislocations were tested in the simulations ranging from one to seven times the 90° partial $\frac{1}{3}\{10\bar{1}0\}$. It was expected that at some size of confined dislocation, the large in-plane strength of the individual layers may be able to overcome the relatively weak interlayer binding, and in doing so induce a crack to relieve strain induced in the basal plane

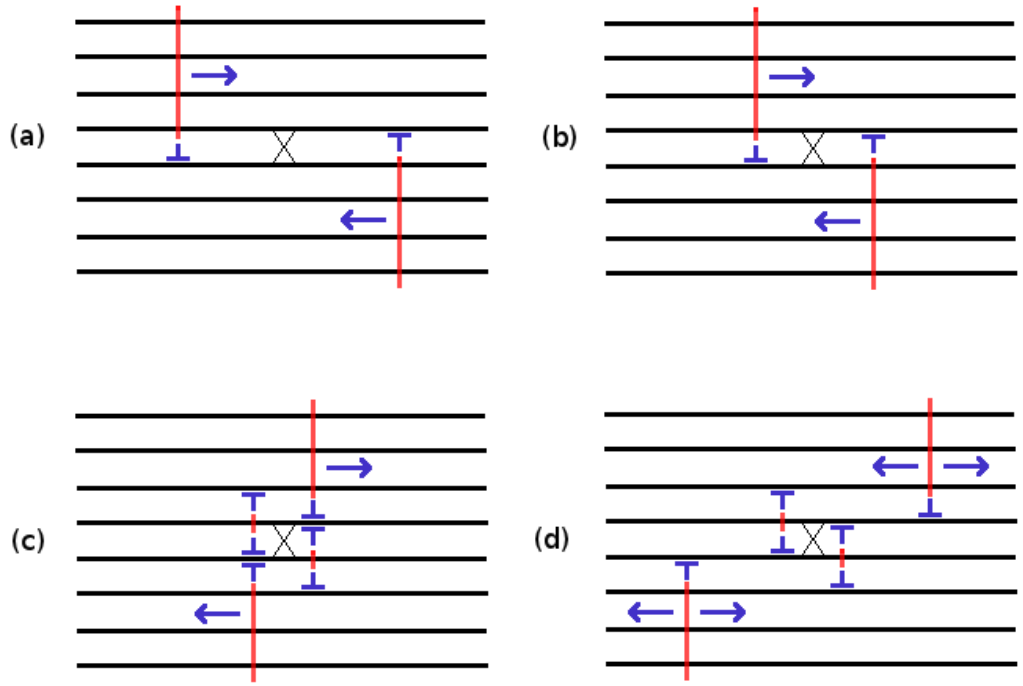

Figure 2.3: Proposed reaction for dislocation dipole pinned using interstitial at slip plane. Dislocations are represented by red lines terminated with T symbols, and the cross in the centre represents the interstitial atom bonded into adjacent graphite planes. (a) The initial dislocation dipole configuration. (b) The dislocations attract, moving towards the pinning point. (c) The ends of the dislocations become trapped in place either side of the interstitial and the dislocations climb by $\mathbf{c}/2$ (d) Deposited material from dislocations remain at the pinning point causing distortion of the two central planes, while the climbed dislocations move to find a lower energy arrangement.

by the extra material. Such cracks or voids are often seen in neutron irradiated graphite over various length scales, appearing to be fractal in nature, but their origin is not well understood [30].

The starting structures, generated with the use of the anisotropic displacement field for a straight edge dislocation, were modelled using a short molecular dynamics (MD) simulation. The temperature of these runs was 10 K and the simulation allowed to evolve for 1 ps. Even at this low temperature, local minima inhibiting the shear of layers would be overcome by small thermal vibrations and allow the system to achieve less accessible states than at zero temperature. The structure resulting from the MD simulation was then allowed to optimise at constant pressure

using a conjugate gradient minimising algorithm.

The structure containing just one pair of opposite sign partial dislocations has shown little structural distortion or signs of cracking, the additional material laying in the slip plane of the dipole has been accommodated by slight bending of the layers as well as small distortions to in-plane bond angles. Increasing the size of the dislocation by one additional 90° partial, it can be seen that the bending of the layers begins to accentuate, and in-plane distortions are generating stresses that are relieved by curvature of the layers. When there are three such dislocations at each core, the layers begin to buckle and the balance between in-plane strain and retaining the natural interlayer spacing is on the threshold of cracking. The separation of the layers, causing cracks relieves the in-plane stress and buckles begin to materialise. These buckles are further accentuated by adding more dislocations, analogous to a pile up that may be caused by the pinning of some dislocations and subsequent interaction with mobile ones. The properties of the buckles as a function of the magnitude of the Burgers vector has been summarised in table 2.1. The amplitude of the buckles has been provided as the difference between equilibrium interlayer spacing, 0.326 nm and the amplitude at the peak of the buckle. The energy stated in the table is per unit cell. The input structure and optimised final structure for the case of four confined dislocations are shown in figure 2.7, with the remaining images shown in the appendix B. Some of the cells show asymmetry in their distortion, such that one of the confined dislocations results in greater buckling than the other. This has arisen due to the method by which the dislocations had been fixed for the optimisation. One of the fixed planes of atoms lies at the centre of the cell, and another at one of the edges (this was sufficient due to the periodicity of the model to confine both dislocations). However, this leaves slightly less than half the remaining cell width for one of the dislocations, resulting in marginally unequal confinement regions. A more symmetric system would be produced if an additional plane of atoms were fixed at the opposite edge of the cell. This was not imperative for these calculations,

n x b_{90}	Amplitude	**c** expansion (%)	energy
1	0.00 nm	0.19	4.6 eV
2	0.01 nm	0.25	13.9 eV
3	0.10 nm	0.57	31.78 eV
4	0.33 nm	1.6	52.8 eV
4*	0.19 nm	0.85	57.9 eV
7	0.34 nm	2.22	100 eV
7*	0.36 nm	2.0	131.9 eV

Table 2.1: Table showing properties of buckles resulting from the confinement of dislocations using fixed planes of atoms. b_{90} is the size of a single 90° partial basal dislocation, 0.142nm.

as the investigation concentrated on confining multiple dislocations, and not on the symmetry of the system.

When four dislocations are confined within half the cell width there is a clear delamination at the slip plane. This has arisen to accommodate the additional material and out-of-plane bending becomes more favourable than in-plane distortion of the C-C bonds. The threshold for layer buckling in the smaller of the two supercells is at three partial dislocations, where 0.42 nm of additional material needs to be accommodated in a region 6.5 nm wide. Moving to an extreme situation of having seven dislocations confined to a region which is about 50% larger than the core width of a single dislocation, buckling amplitude increases so much that it becomes energetically favourable for the buckle to divide into two. The dissociation of the buckle has been investigated to determine whether this is an artifact of the cell size. Table 2.1 contains two entries marked with an asterisk. These two simulations are repeat calculations of the corresponding number without an asterisk, but using a super cell 50% larger in width. The size of the confining region for each dislocation is increased in these larger cells to approximately 9.8 nm. However, the increased cell size did not prevent the buckle from dissociating into two. This indicates that either the cell is still not sufficiently wide enough to accommodate the core width of each dislocation, or that there is a threshold of

buckle size at which point the collapse into two smaller buckles is a more stable configuration. The largest increase in **c** parameter occurred when a dipole of seven dislocations were contained in the smaller of the two unit cells. This was to be expected since the threshold for buckling was just three dislocations, and further confinement of greater numbers of dislocations requires accommodation of more material in a fixed volume, resulting in cell expansion.

When comparing the results from the two cell sizes in which four dislocations were present, an interesting observation is that an increase in confining width resulted in a reduction in **c** axis expansion (1.25% as opposed to 2.5%) but a slight increase in energy (about 53 eV to 58 eV). This might be interpreted as the energy due to in-plane strain being much greater than the energy gain by reducing out-of-plane displacement. The same trend may be seen for the case of seven dislocations, except the reduction in **c** axis expansion is not as great as that of four dislocations (3.1% to 3.4%), and the energy increase is greater relative to the smaller cell (increasing from about 100 eV to 130 eV).

2.4 Folds

Folds in graphite cells have been modelled by using the same methods as for the dislocation dipoles except without any restriction on atom motion. The cells were produced using the displacement field for a climb dipole of prismatic edge dislocations each of Burgers vector **c**/2 as previously shown in chapter 3. The program for generating supercells containing a ruck and tuck is designed to create a fold along any desired chiral direction. This chirality introduces some additional conditions on the supercell and its periodicity. As shown before in chapter 2, defining a direction in graphite using chiral indices introduces a larger periodic repeat distance along the basal plane. This also introduces a new minimum periodic width for the cell. The periodic width of a ribbon correpsonding to a specific chiral vector has been calculated by Jishi *et al.* and is given by equations

(a) The initial structure as defined by anisotropic displacement field equations

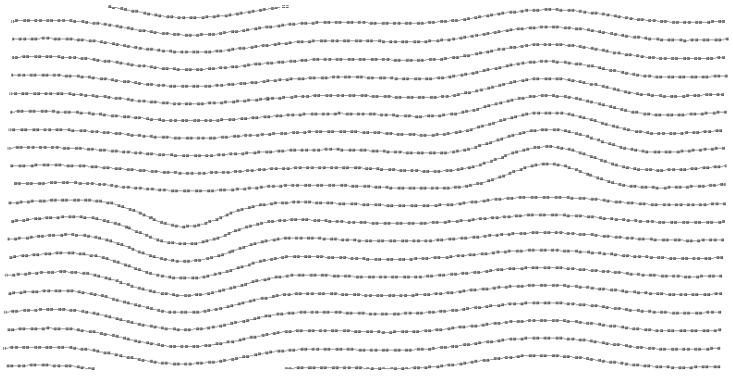

(b) The final structure after MD and molecular mechanics optimisation

Figure 2.4: Optimised structures from gulp containing confined dislocations.

(2.5).

$$L = \frac{\sqrt{3}c_h}{d} \qquad \text{if n - m is not a multiple of 3d} \tag{2.4}$$

$$L = \frac{c_h}{\sqrt{3}d} \qquad \text{if n - m is a multiple of 3d,} \tag{2.5}$$

where $\mathbf{c}_h$ is the chiral vector defined by $(n\mathbf{a_1} + m\mathbf{a_2})$ and d is the highest common divisor of the two chiral indices, n and m. The requirement of periodicity for a unit cell demands two simultaneous conditions from the model. Firstly, the length of the cell must be an integer number of chiral lattice vectors, $\mathbf{c}_h$, and secondly the

total arclength of the layer containing the fold must also be an integer number of chiral vector lengths. By inference, this means the difference between the length of the flat layer and the folded layer is also a whole number times $\mathbf{c}_h$. Scaling factors a and W in the definition for the parametric equation of the fold (table (6.1)) were carefully chosen such that the dimensions of the fold would represent a viable model, such as the interlayer spacing at the points of closest approach for the function and the radius of curvature at the turning points.

The fold was created from a strip of graphene, which was cut out along the direction defined by the chiral lattice vector and with a width associated with the repeat distance for this chiral direction. The folded ribbon was then inserted into the bulk material after a displacement field had been created by using a pair of prismatic dislocations of appropriate size and location. The folded layer was created using the function mapping method developed in chapter 6. The unit cell to accommodate the fold was defined as monoclinic in order to avoid stacking of the folds periodically in the $\mathbf{c}$ direction where displacements are greatest. This allowed the displacements arising from defects in periodically repeated cells to be commensurate and with least interaction. The optimised structure containing a fold is shown in figure 2.5.

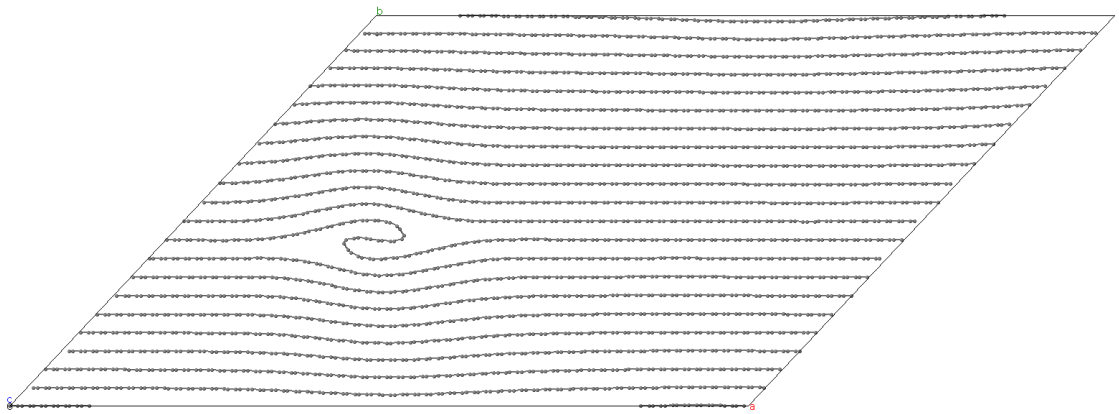

Figure 2.5: Ruck and tuck defect generated using the displacement field of a climb dipole of prismatic edge dislocations, combined with a fold for which atomic coordinates were mapped onto the surface of the representative parametric equation. Structurally optimised in GULP

The changes in the optimised structure as compared to the starting structure are quite small. The fold has shown to be stable during optimisation in that it has not overturned and converted into a buckled configuration. Larger folds, ones with a greater separation between turning points, would be more stable because of the additional area over which interlayer binding occurs. The curvature at the extremeties of the fold have become slightly more accentuated but overall, the function mapping has been successful in an approximate representation of such a fold defect.

A similar folded structure had been previously created using Cerius^2 modelling software by simply forcing additional material above and below a single layer, making necessary bond adjustments to create a fold, followed by structurally optimising the resultant cell. The result shows more a constant curvature at the fold edges, whereas optimisations by GULP have produced a sharper tip like effect (see figure 2.5). Previous work by Davidson [31] included X-ray diffraction simulations from the ruck and tuck defect produced from structures optimised in Cerius^2. The results reproduced more diffraction spots such as those pertaining to the $(10l0)$ planes than those structures from GULP. Figure 2.6 shows the optimised structure from Cerius^2 which implements a universal force field (UFF) potential to govern the structure. This should be compared to the GULP optimised structure in figure 2.5.

2.5 Prismatic loops

Circular interstitial dislocation loops are modelled as rotationally symmetric discs between the layers of graphite. Their symmetry is by rotation about an axis normal to the basal plane. The use of dislocation displacements to accommodate such a defect has been adapted from the straight edge dislocation equations (3.24) and (3.25). Due to the rotational symmetry of the interstitial loops, it is possible to substitute one of the equations for a radial function that simply acts at a

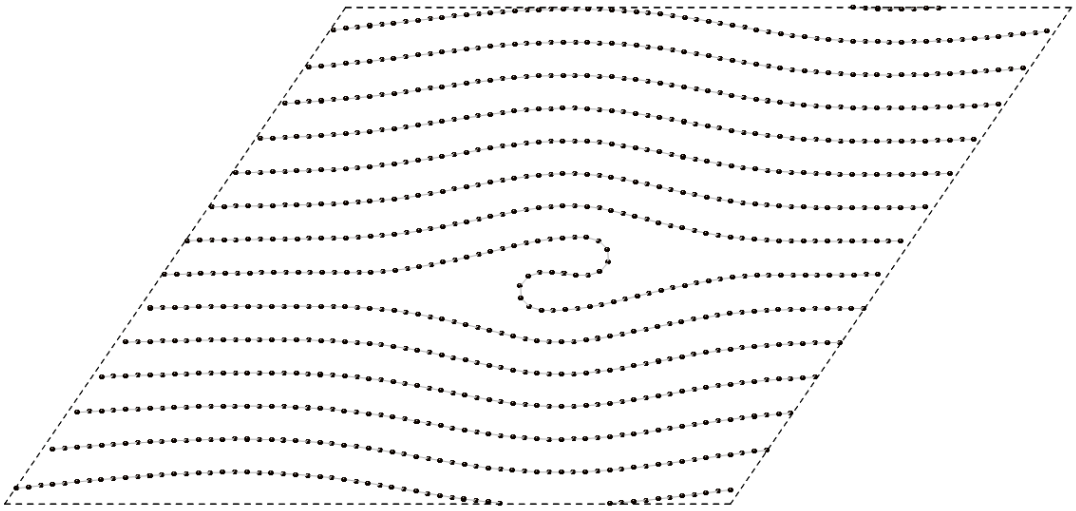

Figure 2.6: A fold created using the molecular modelling software Cerius^2 by physically adding material to a central layer and allowing the system to relax under the UFF potential. The curvature at the edges of the folds are more constant when compared to the structures produced from GULP.

distance, R, from the core. The anisotropic elastic equations that have been used are such that displacements due to the dislocations occur in the x-y plane, with x lying in the basal plane. For a radial defect such as a disc, the displacement in the **c** direction only varies with R, and is constant in θ. As such the the x coordinate has been replaced with $R = \sqrt{x^2 + y^2}$ to account for the rotational symmetry. The function has been applied to generate a structure containing two loops of radius 0.7 nm, each of Burgers vector $\mathbf{c}/2$ in a hexagonal arrangement to reduce strain field interference.

The main change to the prismatic loop cells during the optimisation has been in the curvature of the planes immediately surrounding the edges of the interstitial dislocation loops. The initial structure, generated using the anisotropic equations in chapter 3 produced relatively sharp curvature of the layers surrounding the edges of the discs. However, this region is very near the core of the introduced dislocations where linear elasticity is inadequate in reproducing large lattice distortions. When dealing with dislocations in linear elasticity, a cutoff parameter, usually denoted r_0 is applied such that only material outside of this radius is treated.

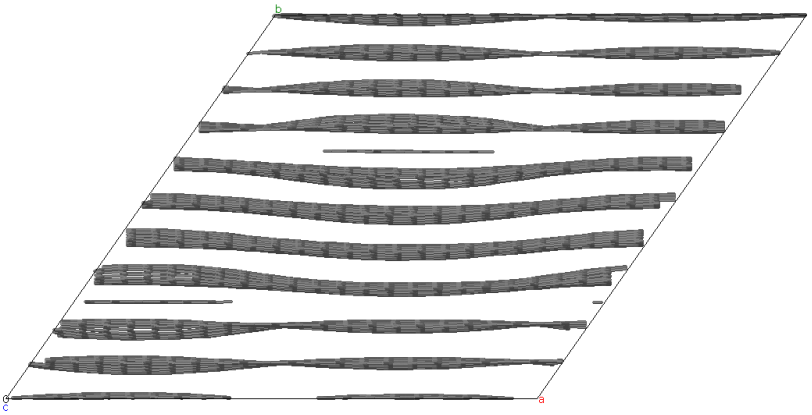

(a) The structurally optimised supercell containing prismatic dislocation loops as viewed along the basal plane shows the induced displacement and arrangement.

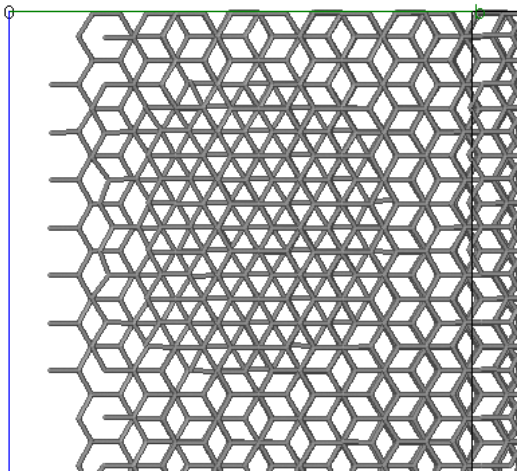

(b) A prismatic interstitial loop as viewed in the **c** direction. The loop is visible as an ABC stacking fault region (seen in the image as bonds appearing to extend to all corners of the hexagonal layer).

Figure 2.7: Optimised structure containing interstitial dislocation loops in graphite. The loops are 0.7nm in radius and are represented by prismatic diclocations **b**=**c**/2.

Chapter 3

Dislocations in graphite

The crystal dislocation was first postulated by Taylor, Orowan and Polyani independently of one another in 1934 [32, 33]. Their proposal was that dislocation slip could explain the phenemomenon of plastic deformation in crystals. Dislocations are also responsible for the theoretical shear strength of a crystal being orders of magnitude larger than the experimentally measured values. Dislocations are 1-dimensional defects and are sources of internal stress in a crystal [34]. Unlike point defects, they extend through a material, creating a line separating slipped regions of crystal from unslipped regions. An individual dislocation can neither begin or terminate inside a crystal and therefore must either be a closed loop or terminate at a free surface or grain boundary. Dislocations are characterised by their Burgers vector $\mathbf{b}$ and line direction ξ. Basal dislocations are prevalent in neutron irradiated graphite and play a defining role in its mechanical properties. It is these basal dislocations which are accountable for the vast discrepancy between experimentally observed shear strength and the theoretically expected value [32, 33]. An insightful analogy for the slip mechanism in a crystal is the motion of a ruck in a rug, which may be translated through the rug much more readily than moving the whole rug at once. Rather than translating all the components of an entire layer over another one in unison, the same result can be achieved by moving dislocations. This dramatically reduces the amount of shear stress required to

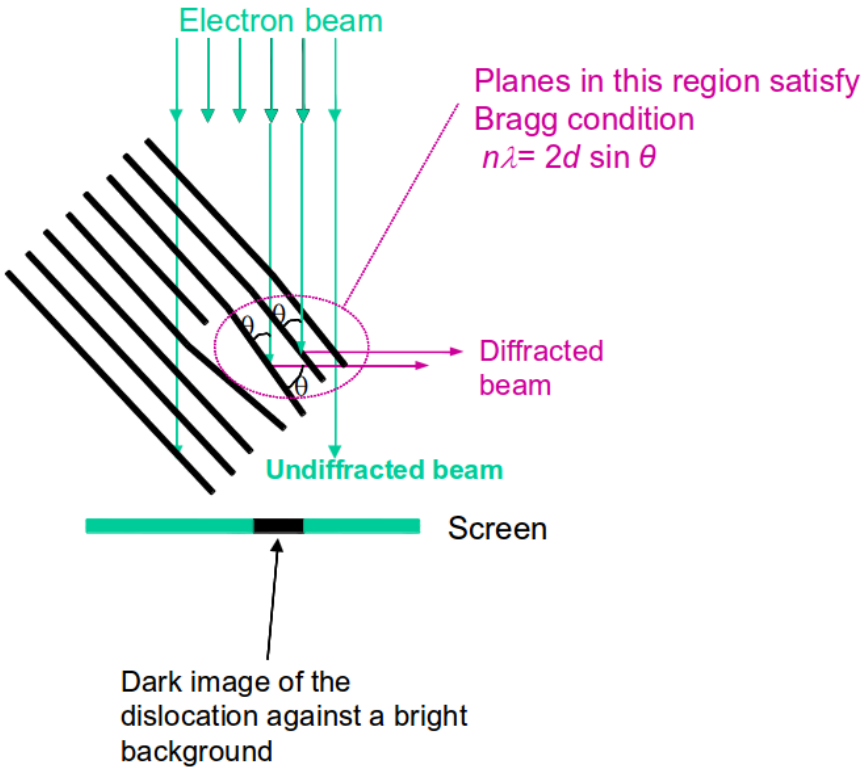

Figure 3.1: The fulfillment of the Bragg condition for diffraction at the edge of a dislocation. The curved layer of atoms changes θ, causing diffraction at specific locations. Image reproduced from [38].

translate one layer over another by slipping discrete amounts of material at a time.

Dislocations in graphite have been an area of much research interest [35, 28, 36, 37]. They are abundant in images of nuclear graphite, showing up as lines or loops of opposite diffraction contrast to the surrounding image due to plane bending, which fulills the Bragg condition at some point along the deformation around the defect [13]. This effect is illustrated in figure 3.1.

Dislocations are shown to have been imaged, appearing to interact with prismatic loops, which impede their glide on the basal plane, inducing curvature and elongation of the line 3.2. These loops, clusters of interstitial atoms, are said by the standard model to be responsible for the dimensional change in the **c** direction at high irradiation temperatures (>500 K). The local dimensions, the height and depth, of adjacent interstital and vacancy loops near the surface of

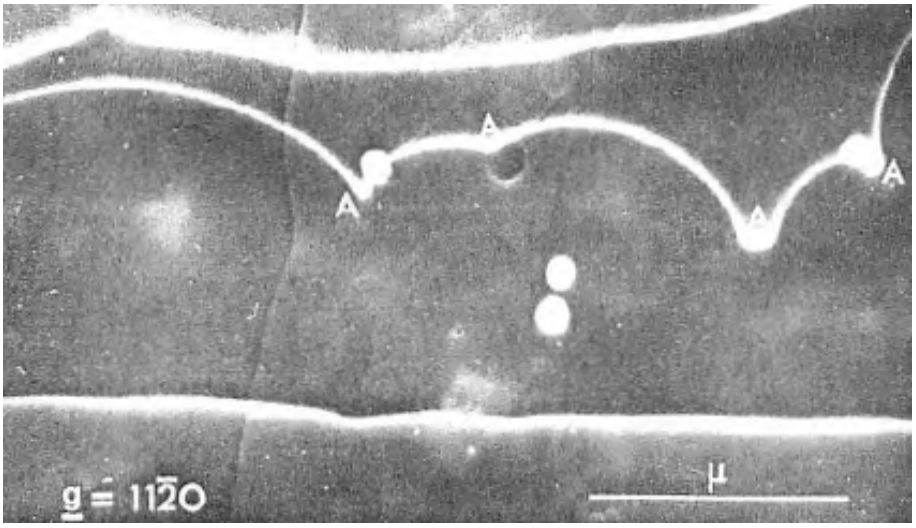

Figure 3.2: Image reproduced from [13] showing loops restricting the glide motion of partial dislocations in the basal plane

a graphite sample have been measured by Ouseph [37]. The paper finds that the variation in height across each of the defects is almost equal and opposite, measuring 0.35 ± 0.2 nm, a result that is in line with a partial prismatic dislocation of Burgers vector 0.335nm. The paper also states that a typical diameter of these prismatic loops in graphite is found to be about 40 nm. A standard way of preparing a sample containing dislocation loops is to irradiate graphite films with fast neutrons followed by an annealing step at $\tilde{2}$000K, creating Frenkel pairs and the aggregation thereof [37].

An investigation into the dimensional change in graphite during electron beam irradiation has been performed by Koike *et al.* [39]. The experiment used 300 keV electrons impinging on a sample of HOPG at temperatures ranging from around 300-900 K, while the lattice parameters were monitored under high resolution TEM. The results reproduced the strikingly large expansion in the prismatic direction during irradiation at room temperature, as shown in figure 3.3. It was found that the expansion saturated at 300% in the **c** direction with only small contraction in the basal plane. In addition, this value is estimated to be slightly low due to the sample expanding beyond the radius of the electron beam.

Vacancies in the carbon lattice that aggregate to create lines form an important

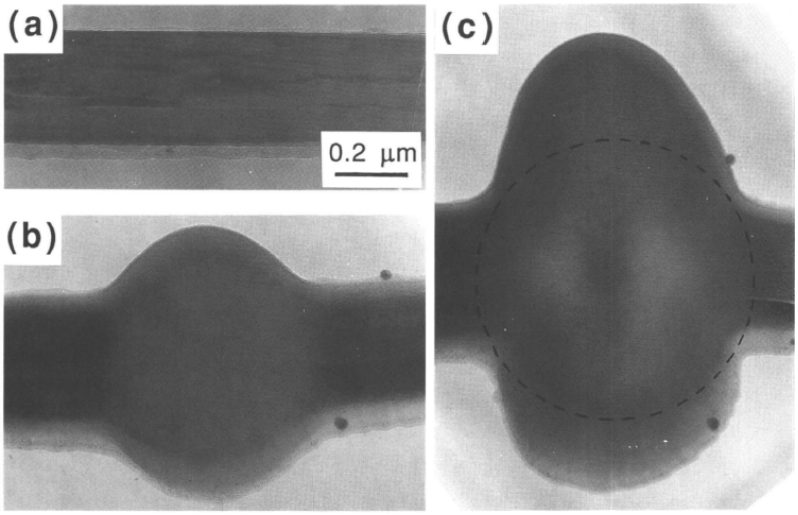

Figure 3.3: 300 keV electron irradiation at room temperature. The sample of HOPG produces enormous expansion along **c** $\sim$ 300%. Image reproduced from [39]

part of the standard model for radiation damage in graphite [13]. The closure of these lines across their width is proposed to account for how basal planes contract as collisions remove atoms from their lattice sites. Insight into a mechanism by which non-basal dislocations nucleate from the reconstruction of di-vacancies (V_2) is provided in a paper by Niwase[36]. The subsequent growth of the lines occurs as a result of additional vacancies formed at the more damage susceptible ends of the dipoles. Multiple vacancies in a line may heal or reconstruct across their width to remove the highly reactive dangling bonds. This phenomenon is part of the standard model for radiation damage in graphite to explain the **a** axis contraction with increasing neutron dose. With such reconstructions, it is possible to find five, seven, and eight-fold rings in the layers, which are defects that are associated with curvature in the layers. For example, the 5-fold pentagonal rings are essential for creating fullerenes such as C_{60} [40]. The curvature arises from shapes that are unable to tesselate, or completely fill space in a plane. Graphite appears to amorphize when irradiated beyond 1 displacement per atom (dpa), however, high resolution electron imaging later showed layer ordering at the nanoscale in the **c** axis [41]. Only until 6 dpa is reached does this stacking sequence become completely negligible [39]. Niwase has presented a model to explain the amorphisation of

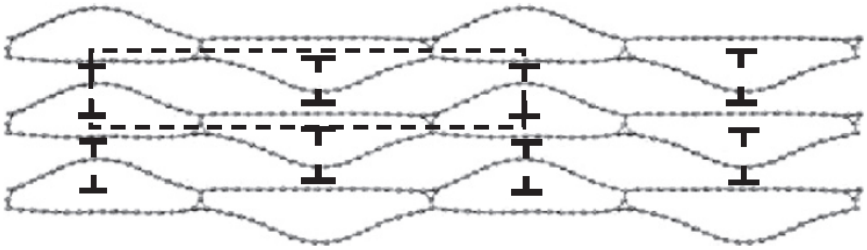

Figure 3.4: Basal dislocations pinned by spiro interstitals and the resultant buckling of layers. Image reproduced from [21]

irradiated graphite using a model which involves the accumulation of dislocation dipoles. This accumulation is said to be responsible for inducing local curvature in the layers, and as such begins to appear amorphous [36].

At low temperatures when interstitial defects are relatively immobile, they provide a confinement for moving dislocations which may result in local buckling of layers. Basal dislocations are proposed to have a significant contribution to the property changes resulting from particle irradiation [21]. Namely, that corrugation of graphite layers occurs when the cores of basal dislocations are sufficiently close to interact and are localised by interlayer defects. A schematic of this structure is shown in figure 3.4. At higher temperatures when effects from pinning points become less significant, the buckles are removed, allowing for the difference in dimensional change between the high and low temperature regimes. At higher temperatures, the interaction between basal dislocations is still important however, their interactions can result in a pile up involving multiple dislocations impinging on the same region of the crystal causing a fold [21]. The pile up of basal dislocations transforms into a series of climb dipoles, the number of which is determined by how many basal dislocations are involved in the fold. Fold growth may also occur by subsequent basal dislocations in the fold layer depositing material at the extremeties of the fold. This process results in annihilation climb of $\mathbf{c}/2$ of the passing dislocations.

Recent work by Sun *et al.* investigates graphene arranged on a SiC substrate [42]. Using STM imaging it was found that the graphene has surface features

like buckles, which have occurred to relieve in-plane compressive strain. This surface buckle was shown to be readily moved and augmented with the tip of the STM, and it was also found possible to form new ridges using the STM tip by manipulating regions of the surface local to the feature. Other instances of the occurrence of surface features like buckles and folds have also been reported in TEM images [43]. Xu *et al.* present high resoltuion STM images of ripples at the surface of graphene reaching amplitudes of up to 2.5 nm, more than seven times larger than one interlayer distance, and provide evidence for changes in the electrical properties of graphite at these regions [44]. Chang *et al.* also report of "giant corrugations" on the surface of cleaved HOPG. The prediction as to how the phenomenon came about was not definitive, but they attributed it to "multilayer electronic interactions" between the layers [45]. The surface ridge could however have been an effect from basal dislocations, where the rippling is a consequence of in-plane stress.

Buckles and folds have not been directly observed in bulk graphite, but there exists high resolution images of irradiated graphite in which there are a multitude of defects, some of which have gone uncategorised and in some instances there may be ambiguity or uncertainty in the interpretation of line defects [13].

3.1 Dislocations in graphite

This chapter will briefly review the various types of dislocation that occur in graphite, and subsequently other hexagonal layered materials. Following this, simulations of basal dislocations using the GULP software are presented, an investigation into the behaviour of isolated, constrained basal dislocations in graphite. Firstly, it is instructive to confirm the conventional notation for crystal directions and Miller planes which will be implemented througout. Brackets [ ] and ( ) are used to define particular directions and planes respectively, while ⟨ ⟩ and { } are used to define sets of directions and planes respectively, those of the

same type that are equivalent by crystal symmetries [34]. Directions in the basal plane of graphite are often described using four indices, $(hjkl)$. The first three letters relate to coefficients of the three basal vectors that are separated by 120 degrees from each other and the fourth is that for the **c** direction.

3.1.1 Screw dislocations

Screw dislocations are characterised by the fact that their line direction is parallel to their Burgers vector. The normal vector to the glide plane of a prismatic screw dislocation points in the [0001] direction. Prismatic screw dislocations in graphite disrupt the layered nature of the material by introducing bonds to be made between them. This connecting of layers to one another inside the material in a helical fashion, much like a spiral staircase, alters the properties of graphite in the basal plane. The layer planes are no longer discretised with relatively weak bonds between them, instead covalent bonds are formed between layers.

Screw dislocations of enormous size have long been known to exist in natural graphite, however, such samples contain very few screw dislocations having a small Burgers vector equal to one or two lattice parameters [46]. Hennig reported in a paper after examining approximately 1 cm^2 of natural graphite crystals that not a single screw dislocation was found with a Burers vector equal to just a few lattice vectors [46]. Large prismatic screw dislocations can become so big that even under a modest optical microscope, it is possible to see spiral structures at the surface of crystals [47]. The atoms involved in screw dislocations, near the core or in the far-field, have only vertical displacement. In isotropic elasticity theory, the displacement field for a screw dislocation, most conveniently written in polar coordinates is shown in equation (3.1). There exists only displacements in the z direction, and the displacement u_z changes uniformly as a function of θ.

$$u_z(r,\theta) = \frac{b_z}{2\pi}\tan^{-1}\theta = \frac{b_z}{2\pi}\tan^{-1}\frac{y}{x} \tag{3.1}$$

The termination of a screw dislocation line at the surface of a crystal produces a reactive site which may be etched away using reactive gases such as O_2 or Cl_2 to reveal a spiral structure [46]. Basal screw dislocations have both Burgers vector and line lying in the basal plane.

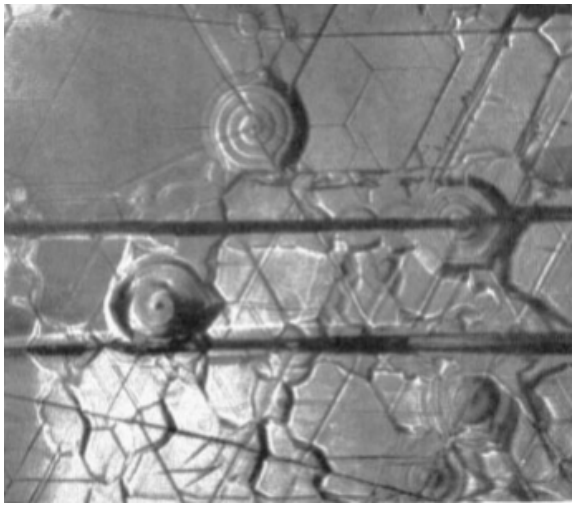

Figure 3.5: Screw dislocation in graphite revealed as an anti-clockwise spiral by etching away the (0001) cleavage face. Magnification is x120. Image reproduced from Patel [47]

3.1.2 Edge dislocations

Edge dislocations can be thought of as extra half planes of atoms that terminate inside a crystal. This extra half plane terminates in what is known as the dislocation line. A depiction of an edge dislocation in a cubic crystal is shown in figure 3.6. In a layered material like graphite, which is highly anisotropic, the direction of the dislocation line is an important factor in the resultant property changes to the material.

The Burgers vector may be determined by tracing a Burgers circuit around the dislocation core. When this circuit is repeated in a perfect region of the crystal, the Burgers vector is defined by the vector that is required to complete the loop. A dislocation is said to be perfect if its Burgers vector is an integer number of lattice vectors. If the Burgers vector is a fraction of a lattice vector, the dislocation is said to be partial. Due to the layered nature of graphite, edge dislocations are

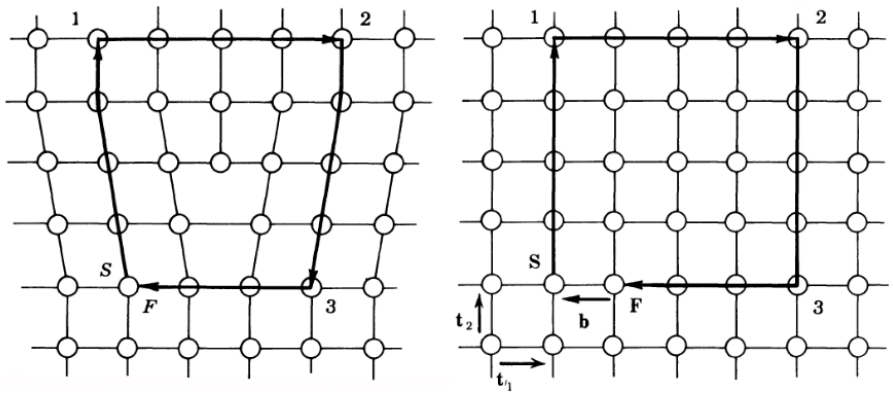

Figure 3.6: An edge dislocation in a simple cubic crystal showing the Burgers circuit in the presence of a dislocation, compared with the same circuit in the unperturbed crystal.[48]

classified into further types. Dislocations which have a Burgers vector aligned with the crystal's **c** direction and line in the basal plane are called prismatic. Those with Burgers vector in the **a** direction and line in the basal plane are called basal. Non-basal dislocations also have their Burgers vector point in the **a** direction, but their line direction points along **c**. Dislocations are distinguished by their glide planes, as more than one type has their line direction lying in the basal plane. Prismatic dislocations are far less mobile than basal dislocations, because glide in the **c** direction requires the breaking of carbon-carbon bonds, each having a cohesive energy of about 7.3eV [49]. Basal dislocations however, require no bond breaking in order to move due to the weak interlayer binding in graphite, instead they only have to overcome a shallow Pierels barrier. This striking property arises as a direct consequence of the contrast between the interplanar and intralayer cohesive binding. The phenomenon may be understood better with the use of a simple model such as the Frenkel-Kontorova model of a dislocation [50]. This model involves balls representing atoms, connected by springs, each situated in a potential well representing the potential landscape of one plane as "felt" by another. For graphite, the case is such that the springs connecting atoms are very strong, whilst the potential barrier governing their translational motion is very low, and as such it is readily envisaged that the atoms may make transitions over these barriers with very little applied shear force.

The number of basal dislocations in graphite is shown to increase with neutron dose [13], however the mechanism by which neutron collisions induce line defects in the graphite crystal is not well understood. A rigorous experimental investigation into the nature of the damage to graphite as a result of high energy neutron exposure has been performed by Thrower [13]. The study includes extensive imaging using TEM and other high resolution microscopy techniques highlighting various defects as a direct result of the irradiation process.

Dislocations are able to move in a crystal by two mechanisms, one is the action of glide and the other is by climb. The glide plane for an edge dislocation is defined by the vector in (3.2), where $\mathbf{n}$ is the normal vector defining the glide plane, $\bar{b}$ is the direction of the Burgers vector and $\bar{\xi}$ is the dislocation line direction. The glide plane for a screw dislocation is not defined by this equation since the Burgers vector and line direction are parallel.

$$\mathbf{n}_{glide} = \bar{b} \times \bar{\xi} \tag{3.2}$$

Dislocations may be categorised as one of two types, glissile or sessile, depending on the nature of their motion. If a dislocation is able to move in the plane which contains both its Burgers vector and line it undergoes conservative motion, or glide. Dislocations which move in this way are referred to as glissile. On the other hand, dislocations that cannot move in this plane, such as prismatic dislocations in graphite, which move most readily by the process of climb, are sessile and they undergo non-conservative motion. Slip planes in crystals are normally those which contain the highest density of atoms, hence the planes separated by the largest distances. In graphite, the relatively large space between the basal planes means that slip is very much more likely to occur along the (0001) plane than any other.

A sample of crystalline material is almost always comprised of multiple smaller domains of individual crystallites. These crystallites are typically randomly oriented relative to one another making up small regions of highly ordered crystal. Grain boundaries in some metals may be seen under optical microscope, as regions of various brightness determined by the change in reflective properties of the different crystal faces exposed at the surface 3.7. When multiple dislocations coexist in a linear fashion, they form a grain boundary which separates two regions of ordered crystal. A depiction of this phenomenon is shown in figure 3.10.

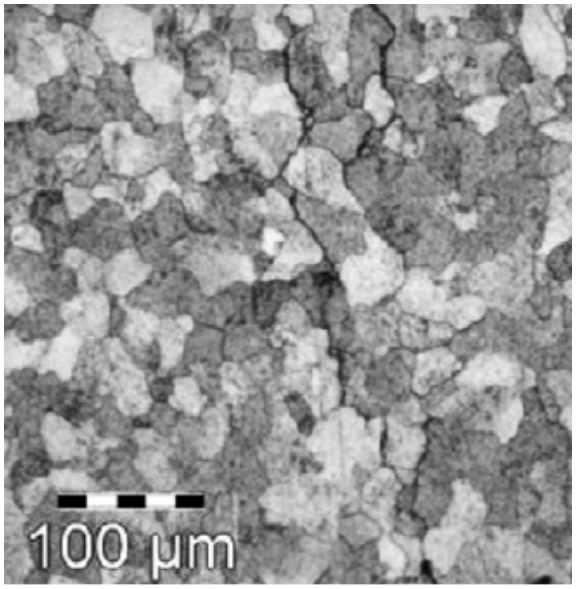

Figure 3.7: A sample of crystalline tungsten under an optical microscope showing the smaller domains of highly ordered crystal that comprise a bulk sample. Image reproduced from [51]

Yazyev and Louie have reported a DFT study of non-basal dislocation dipoles in a supercell in two dimensional graphene [52]. The supercells in the calculations have the dislocations separated by 4 nm along the grain boundary lines. They found the grain boundary energy to be insensitive to changes in the inter boundary separation. The angle of the grain boundary is dependent upon the density of dislocations along the climb direction, the more densely arranged they are, the greater the angle between adjacent crystallites. Their calculations also showed that a single non-basal dislocation involving five and seven membered rings induces buckling in

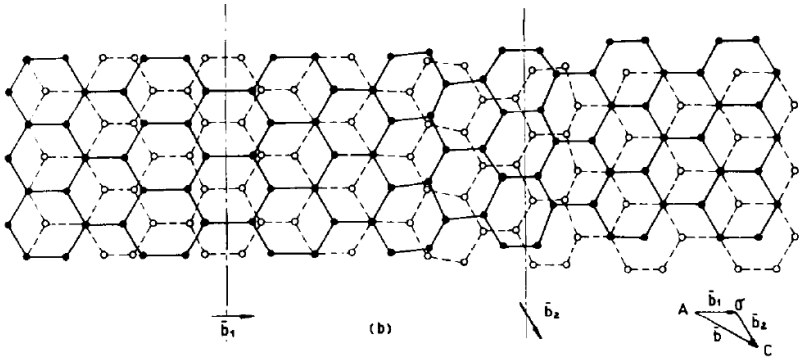

Figure 3.8: A dipole of partial basal dislocations, the one on the right hand side displays a component having screw character. Image reproduced from [53]

the layer, with an amplitude of approximately 0.3 nm [52].

3.1.2.1 Basal dislocations

Basal dislocations in graphite glide on the (0001) plane and are one of the most commonly occurring types of dislocation and are shown to be abundant in samples of neutron irradiated graphite [13, 53]. They are thought to play a key role in subsequent damage processes by their interaction [21]. One of the properties of the basal dislocation in graphite is that it has the ability to move with very little applied stress [28]. Telling and Heggie calculated the Peierls barrier for the partial basal dislocation to achieve glide, and subsequently the Peierls stress required to move the dislocation. They found the Peierls stress required to move the dislocation to be effectively zero [28]. The stacking fault introduced between a dipole of dissociated partial dislocations in graphite is of the form ABCBC. When viewed across the glide plane, the structure appears like that shown in figure 3.9. Note that unlike figure 3.8 there is no screw component to the dislocations, as the dislocations are pure edge in character and oppositely signed 90° partial dislocations.

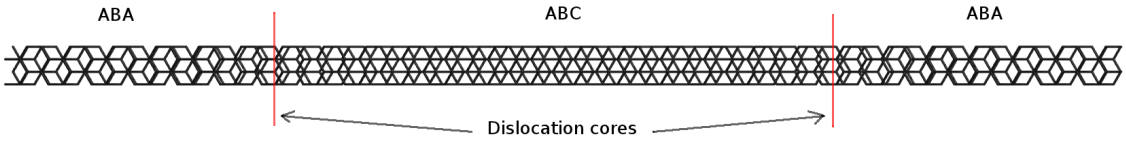

Figure 3.9: The rhombohedral stacking fault bounded by a dipole of 90° partial basal dislocations in graphite.

3.1.2.2 Non-basal dislocations

No calculations have been performed on systems containing non-basal dislocations, hence only a brief explanation and background of such dislocations in graphite is presented here. Non-basal dislocations have their line, ξ, normal to the basal planes of graphite $\langle 0001 \rangle$, and their Burgers vector, $\mathbf{b}$, lying in the basal plane, $\langle 11\bar{2}0 \rangle$. Ewels *et al.* have investigated the core reconstruction of non-basal dislocations in graphite using *ab initio* methods [54]. The calculations show that the core may completely reconstruct to form a pentagon-heptagon pair. However, the energy barrier to motion for the non-basal dislocation is very high, 7.64 eV requiring reconstruction of bonds. If an adatom is present at the core (diagram shown in figure 3.11) then the barrier to motion is substantially reduced, and could be further reduced by applied stresses in the direction of glide [54].

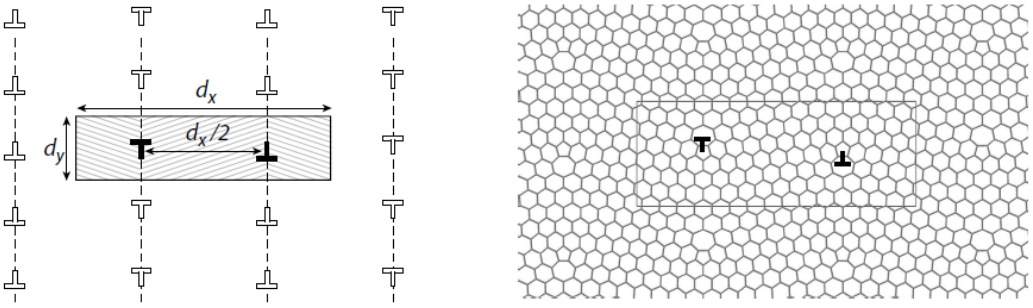

Figure 3.10: A line of dislocations of the same sign create a tilt boundary in the surface of graphene. The image shows a dipole of non-basal dislocations arranged in a supercell at maximum separation, half the width of the cell. Image reproduced from [52]

Roscoe and Thomas developed an experimental method for distinguishing between the surface intersection of non-basal screw dislocations and non-basal edge

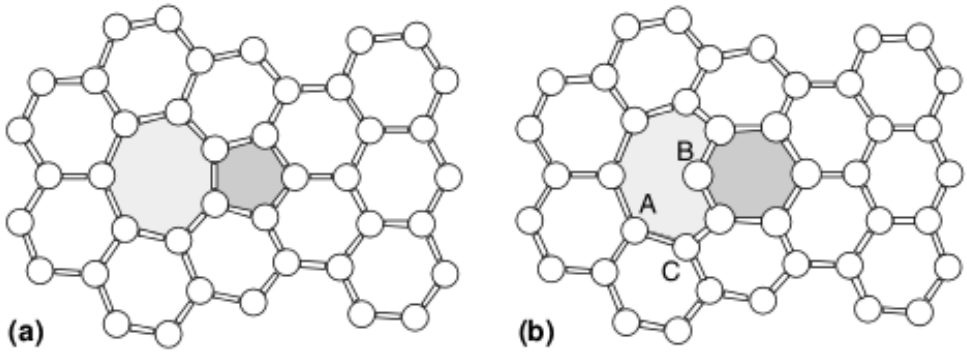

Figure 3.11: The reconstructed core of a non-basal dislocation (a) without and (b) with adatom showing atoms involved in the glide process. Scenario (b) has the lower activation energy of the two. Reproduced from [54].

dislocations, since both provide reactive sites known as etch pits when terminating at a surface [55]. Hashimoto *et al.* have used TEM imaging methods to directly observe a non-basal dislocation defect in a graphene sheet produced by irradiating the sample with electrons. The result is exceptional examples of high resolution images of individual defects, as shown in figure 3.12 [56]. A non-basal dislocation is easier to visualise in a single layer. In which case, the dislocation is an extra line of atoms terminating at a point in the layer. It can be seen that the core is made up of two shapes normally associated with curvature, as found in fullerenes, a pentagon and a heptagon. These dislocations are also shown by Hashimoto exist in nanotubes [56], and can allow a variation in nanotube diameter along the length of the tube.

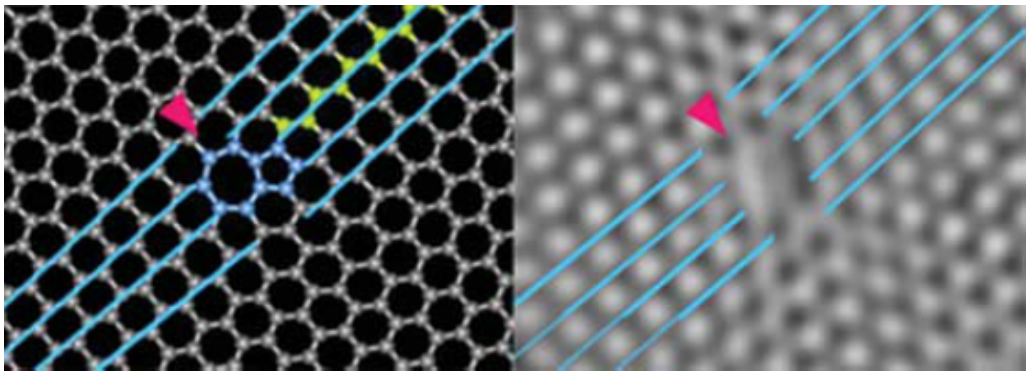

Figure 3.12: The core of a non-basal dislocation in a graphene sheet induced by electron irradiation. The extra line of atoms (green) are seen to terminate at the pentagon and heptagon shapes (blue) in the layer. Image source [56].

3.1.2.3 Partial dislocations

Basal dislocations in graphite may undergo a dissociation reaction in order to lower their energy. Dissociation may only occur where a low energy stacking fault is possible. One example of a dissociation reaction is that of a full basal dislocation in graphite. The Burgers vector $\mathbf{b} = \mathbf{a} = 0.24$ nm along the $\langle 11\bar{2}0 \rangle$ direction in the basal plane, described vectorially in equation (3.3) dissociates into two smaller dislocations each with size $\mathbf{b}/2$. An example of a network of partial dislocations occurring in graphite is shown in figure 3.13.

$$\frac{1}{3}a[11\bar{2}0] = \frac{1}{3}a[10\bar{1}0] + \frac{1}{3}a[01\bar{1}0] \tag{3.3}$$

Evidence of large networks of partial dislocations and their associated stacking fault regions have been observed experimentally in graphite [53]. The intersection of partial dislocations creates nodes, at each node, the total Burgers vector must be conserved. The sum of the Burgers vectors of the dislocations entering and leaving the nodes must sum to zero. This condition is analogous to Kirchoff's law in electric circuits which accounts for conservation of charge. Upon dissociation, there are three energy components that govern the final configuration of the partial dislocations. Firstly, the sum of the self energies of the two partials is less than that of the original, as the self energy of a dislocation increases with the square of the Burgers vector (as can be seen in eq. (3.4)) hence by splitting into two dislocations of equal size, the energy is reduced by a factor of two. The separation of the dislocations into partials necessarily introduces a region of stacking fault bounded by them. This is a result of the partial dislocations not extending over whole lattice vectors. In graphite, the AB stacking is disrupted and a new sequence is introduced, denoted ABABCACAC, where rhombohedral stacking is introduced at the slip plane. The energy of this relative to AB is 0.05 meV$\mathring{A}^{-2}$ Finally, an interaction energy between the two dislocations arises (eq.(3.5)), the force between dislocations of the same sign in the same glide plane is always repulsive. As

such, there is an equilibrium separation of the partial dislocations governed by the energy gain in dissociation and the energy cost of creating a region of stacking fault [48].

$$\frac{E}{L} = E_c + \frac{\mu \mathbf{b^2}}{4\pi(1-\nu)} \log \frac{R}{r_0} \tag{3.4}$$

μ is the shear modulus, ν is the Poisson ratio and E_c is the core energy of the dislocation. The deformation in the region contained within the radius r_0 from the core is not described by linear elasticity theory. The core radius is typically chosen to be approximately the length of the Burgers vector. The core of a dislocation requires treatmeant by means other than linear elasticity, such as atomistic computational simulations [57]. However, the contribution to the total energy from the core is considerably lower than that from the elastic strain contribution [34]. The outer radius R is the cutoff radius, which is required due to the self energy of a dislocation not being convergent as R $\to \infty$, due to the logarithmic dependence. However, in reality crystals are never infinite in size and R will always be finite.

$$\frac{E_{int}}{L} = -\frac{\mu \mathbf{b_1} \mathbf{b_2}}{2\pi(1-\nu)} \log \frac{R}{R_a} \tag{3.5}$$

$$E_{SF} = \gamma A \tag{3.6}$$

Where gamma is the energy per unit area of the faulted region, which is dependent on the nature of stacking created. The energy of faulted regions is normally stated as the difference between itself and AB stacking.

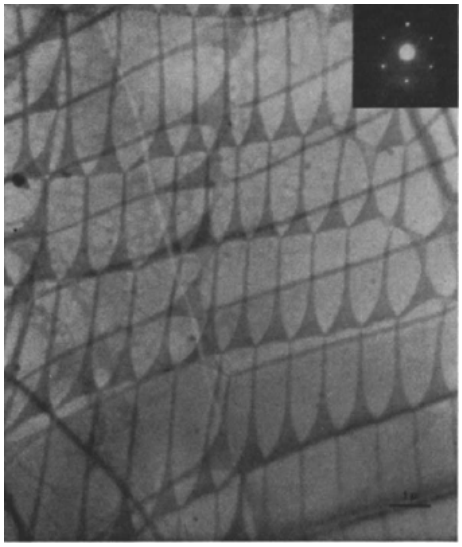

Figure 3.13: Partial dislocation networks in graphite shown up by contrast of faulted regions in the basal plane. Image reproduced from [53]

3.1.2.4 Mixed dislocations

The character of a dislocation describes whether it is of edge or screw type. Dislocations do not necessarily have to be of pure character, that is to say the dislocation may be composed of mixed types and may be split up into constituent vector components, one having screw and one having edge character. The diagram shown in figure 3.14 for example, shows how a curved dislocation may be of pure character at one point, but as the line is traversed, it may end up pure in character of the opposite type at another point [34]. This is because the Burgers vector of a dislocation loop is the same at every point, which results in a change in the value of $\mathbf{b} \cdot \xi$. The elastic field produced by a mixed dislocation is calculated by the sum of its constituent edge and screw components.

3.1.3 Elastic constants of graphite

Hooke's law states that a materials' deformation response is directly proportional to the applied stress. In three dimensions, the equation is written in tensor form as shown in equation (3.7).

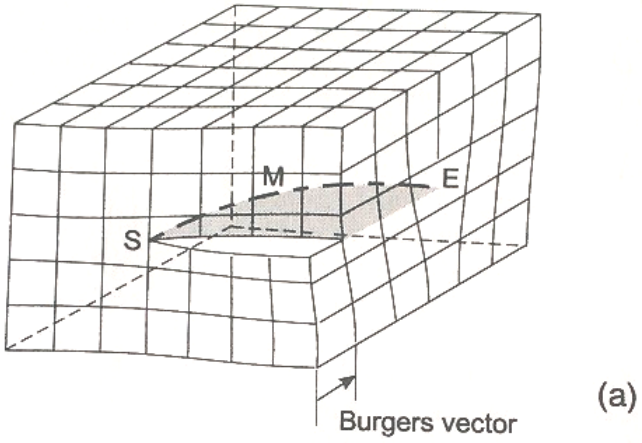

Figure 3.14: A curved dislocation in a cubic crystal which changes character along its length. The dislocation is purely edge in character at E and purely screw in character at S. Reproduced from [34].

$$\sigma_{ij} = C_{ijkl}\epsilon_{kl} \tag{3.7}$$

$$\epsilon_{kl} = \frac{1}{2}\left(\frac{\partial u_k}{\partial x_l} + \frac{\partial u_l}{\partial x_k}\right) \tag{3.8}$$

Where C_{ijkl} is a 9x9 tensor containing the elastic constants relating to the various directions in the material, σ is the stress and ϵ is the strain given by the expression shown in equation (3.8). A cubic crystal requires three independent elastic constants to completely define its elastic properties, which may be reduced to just two if the material is elastically isotropic. Anisotropic materials in general require many more than this due to the variation in mechanical properties along different crystal directions. The general form for the elastic constant tensor contains 81 entries, but this be reduced in size due to symmetries such as those shown in equations (3.9), which automatically reduces the number to 21 independent elastic constants. The notation for the elastic constants is conventionally abbreviated in a contracted notation. In this case the number of indices is reduced to 2 instead of 4, each index condensed to represent a pair. The indices also only run from 1 to 6, rather than 1 to 9, made possible due to native symmetries in the elastic constant tensor. Table 3.1 shows the result of contraction by cyclic permutation

of the indices.

ij, kl	11	22	33	23	31	12	32	13	21
mn	1	2	3	4	5	6	4	5	6

Table 3.1: Contracted elastic constant indices. The repetition of indices 4, 5 and 6 is achieved by use of the symmetry $C_{ij} = C_{ji}$.

In graphite, this number is further reduced to just five non-zero values as a result of crystal symmetries, the remaining constants in contracted notation are C_{11}, C_{12}, C_{13}, C_{33} and C_{44}. Values for which have been obtained both experimentally [15] and theoretically [5].

$$C_{ijkl} = C_{klij} \tag{3.9}$$

$$C_{ijkl} = C_{jikl} = C_{ijlk} = C_{jilk} \tag{3.10}$$

3.1.4 Anisotropic Elasticity

In general, calculating the elastic energy of an arbitrary edge dislocation in anisotropic media requires the solution of a sixth order polynomial. However, such equations cannot be solved in an elementary manner, and numerical approximations are required for polynomials of higher than fourth order, which, in general do not have analytic solutions [58]. Finding the displacements induced in the crystal by the presence of a straight edge dislocation begins with fulfilling the equilibrium equation (3.18). However, if the dislocation lies along one of the three orthogonal Cartesian axes, derivatives with respect to this direction are zero and the problem is greatly simplified, where the indices need only run from 1 to 2 as opposed to all three directions.

The governing equations in isotropic elasticity use parameters μ for a screw dislocation and $\mu/(1-\nu)$ for an edge dislocation. These parameters correspond to

the shear modulus and Poisson ratio respectively. Anisotropic elasticity replaces these parameters with an energy coefficient, usually denoted K, which is defined by the equation (3.11).

$$Kb^2 = b_i \ \mathrm{Im}\left[\sum_{n=1}^{3} B_{i2k}(n)A_k(n)D(n)\right] \tag{3.11}$$

K is a convenient abbreviation made in the equations resulting from solving the equilibrium equation (3.18). The expression shown in (3.12) is formed by combining equations (3.18) and (3.8). It represents three simultaneous differential equations in i but is recognised as being of a standard form, that of the wave equation, with solutions of the type (3.13).

$$C_{i\alpha k\beta}\frac{\partial^2 u_k}{\partial x_\alpha \partial x_\beta} = 0 \tag{3.12}$$

$$u_k = A_k f(\eta) \tag{3.13}$$

Where

$$\eta = x_1 + px_2 \tag{3.14}$$

In these equations, p and A_k are constants. Substituting (3.13) and (3.14) into (3.12), a set of linear equations are formed

$$a_{ik}A_k = 0 \tag{3.15}$$

Which have non-zero solutions only when

$$|\{a_{ik}\}| = 0 \tag{3.16}$$

Which is a sixth order equation in p with roots $p_n, n = 1..6$. For each root p_n there is a set $A_k(n)$ that may be obtained from equation (3.15). It has been shown by Eshelby that the roots of equation (3.16) are never real. Since the displacements u_k must be real, one need only consider the real parts of the solutions to the polynomial p_1, p_2, p_3 and the corresponding sets $A_k(1), A_k(2), A_k(3)$, and as such the equation (3.13) takes the form

$$u_k = \mathrm{Re}\left[\sum_{n=1}^{3} A_k(n) f_n(\eta_n)\right] \tag{3.17}$$

$$\frac{\partial \sigma_{ij}}{\partial x_j} = 0 \tag{3.18}$$

A transformation of coordinates in dislocation theory is common, however the elastic constants are conventionally defined with respect to orthogonal Cartesian axes. In the case of graphite, the constituent graphene layers lie in the x-y plane. It is convenient to change the orientation of the axis with respect to the crystal to make the dislocation line commensurate with a desired Cartesian axis. The equations in Eulerian coordinates to perform a general transformation are shown in (3.19). The equations derived by Hirth and Lothe specify the geometry such that the basal planes lie in the x-z plane and the dislocation line lies along the z axis [48]. This orientation requires a transformation of the elastic constant tensor to correctly represent the properties of the crystal. This method is more conventional in that all the displacements and stresses only occur in the x-y plane.

$$x_1' = (\cos\kappa\cos\phi - \cos\theta\sin\phi\sin\kappa)x_1 \tag{3.19}$$

$$+(\cos\kappa\sin\phi + \cos\theta\sin\kappa\cos\phi)x_2 + \sin\theta\sin\kappa x_3 \tag{3.20}$$

$$x_2' = (-\sin\kappa\cos\phi - \cos\theta\cos\kappa\sin\phi)x_1$$

$$+(-\sin\kappa\sin\phi + \cos\theta\cos\kappa\cos\phi)x_1 + \sin\theta\cos\kappa x_3$$

$$x_3' = \sin\theta\sin\phi x_1 - \sin\theta\cos\phi x_2 + \cos\theta x_3$$

The transformation is normally condensed into a shorter form such as

$$x_i' = T_{ij}x_j \tag{3.21}$$

$$T_{ik}T_{jk} = \delta_{ij} \tag{3.22}$$

The elastic constant tensor transforms as a fourth rank tensor, the transformation of which is given by the following relation [48]

$$c'_{ijkl} = T_{ig}T_{jh}C_{ghmn}T_{km}T_{ln} \tag{3.23}$$

Hirth and Lothe provide the anisotropic displacement field for a straight edge dislocation in a hexagonal crystal whose Burgers vector lies in the x-y plane [48]. These long expressions are shown in equations (3.24) and (3.25). The c' notation refers to the transformed elastic constants according to the orientation of the crystal.

$$u_x = -\frac{b_x}{4\pi}\left(\tan^{-1}\frac{2xy\lambda\sin\phi}{x^2-\lambda^2y^2}+\frac{\bar{c}'^2_{11}-c'^2_{12}}{2\bar{c}'_{11}c'_{66}\sin 2\phi}\ln\frac{q}{t}\right) \tag{3.24}$$

$$-\frac{b_y}{4\pi\lambda\bar{c}'_{11}\sin 2\phi}\Bigg[(\bar{c}'_{11}-c'_{12})\cos\phi\ln qt$$

$$-(\bar{c}'_{11}+c'_{12})\sin\phi\tan^{-1}\frac{x^2\sin 2\phi}{\lambda^2y^2-x^2\cos 2\phi}\Bigg]$$

$$u_y = \frac{\lambda b_x}{4\bar{c}'_{11}\sin 2\phi}\Bigg[(\bar{c}'_{11}-c'_{12})cos\phi\ln qt \tag{3.25}$$

$$-(\bar{c}'_{11}+c'_{12})\sin\phi\tan^{-1}\frac{y^2\lambda^2\sin 2\phi}{x^2-\lambda^2y^2\cos 2\phi}\Bigg]$$

$$-\frac{b_y}{4\pi}\left(\tan^{-1}\frac{2xy\lambda\sin\phi}{x^2-\lambda^2y^2}-\frac{\bar{c}'^2_{11}-c'^2_{12}}{2\bar{c}'_{11}c'_{66}\sin 2\phi}\ln\frac{q}{t}\right)$$

Where convenient use of the following abbreviations has been made

$$q^2 = x^2+2xy\lambda\cos\phi+y^2\lambda^2$$

$$t^2 = x^2-2xy\lambda\cos\phi+y^2\lambda^2$$

$$\phi = \frac{1}{2}\cos^{-1}\frac{c'^2_{12}+2c'_{12}c'_{66}-\bar{c}'^2_{11}}{2c'_{11}c'_{66}}$$

$$\lambda = \left(\frac{c'_{11}}{c'_{22}}\right)^{1/4}$$

The angle ϕ yields real results when the condition in (3.26) is satisfied. However, in a coordinate system where the x and z axis define the basal plane of graphite,

this combination of elastic constants returns a negative value, consequently the roots of the governing polynomial equations are complex. As such, the displacement equations (3.24) and (3.25) may still be used but require the following substitutions

$$2c'_{66} + c'_{12} - \bar{c}'^2_{11} > 0 \tag{3.26}$$

$$\cos 2\phi = -\cos 2\delta, \quad \sin 2\phi = i \sin 2\delta$$

$$\cos \phi = i \sinh 2\delta, \quad \sin \phi = \cosh \delta$$

$$q^2 = x^2 + i2xy\lambda \sinh \delta + y^2\lambda^2$$

$$t^2 = x^2 - i2xy\lambda \sinh \delta + y^2\lambda^2$$

Where δ is determined by equation (3.27).

$$\cosh 2\delta = \frac{\bar{c}'^2_{11} - c'^2_{12} - 2c'_{12}c'_{66}}{2\bar{c}'_{11}c'_{66}} \tag{3.27}$$

Graphite is elastically isotropic in the basal plane, therefore equations (3.24) and (3.25) still hold true for any dislocation whose line exists wholly in the basal plane.

3.1.5 Extended defects

Dislocation theory does not intrinsically provide solutions for defects such as folds and buckles in crystals, but this phenomenon is a unique property of layered materials [21]. However, for such extended defects, the effect to surrounding material may be treated by using an equivalent dislocation representation. Much like prismatic loops and vacancies may be considered as dislocation loops, folds may be considered to be either a pile up of basal dislocations or two prismatic edge dislocations. The displacement field of a defect may be represented as a sum of displacement fields arising from an arrangement of individual dislocations. In the case of a fold such as that shown in 3.15, the displacement field is equivalent to a climb dipole of perfect prismatic dislocations ($\mathbf{b} = \pm\mathbf{c}, \xi$ =basal).

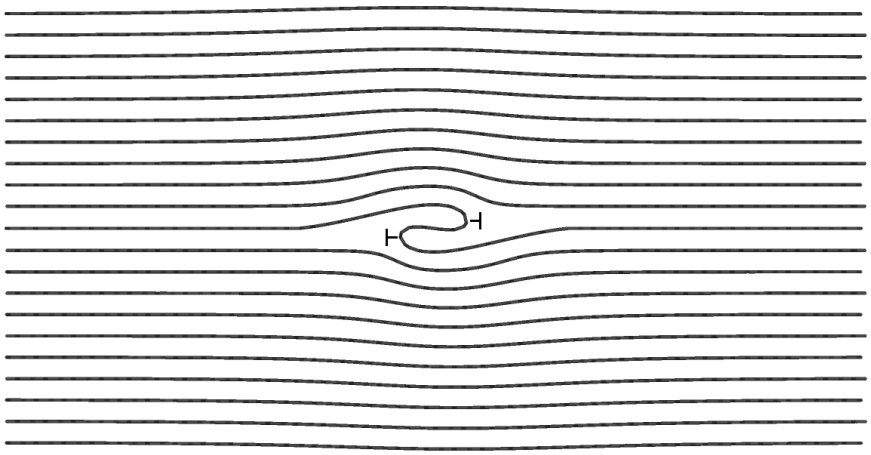

Figure 3.15: A ruck and tuck defect accommodated in the displacement field of a dipole of prismatic edge dislocations, each of Burgers vector $\mathbf{c}/2$, separated by $\mathbf{c}/2$ from one another in the glide direction to account for the asymmetry of the fold. (dislocation positions shown schematically).

When creating structures of defects such as dislocation dipoles for the purpose of computer simulation, it is necessary to consider the unit cell in which they will be contained. There are two configurations which the dislocations may take in the cell, one of which is where dislocations of the same sign repeat directly above one another, creating a tilt grain boundary like structure. The other is to

have the dislocation signs alternate in this direction creating a quadrupole, which may be acheived using the same structure but changing the lattice parameters to that of a monoclinic cell. It was found by Lehto and Oberg that the tilt grain boundary configuration is the lower in energy when compared with that of the quadrupole in the monoclinic supercell [59]. All of the simulations were performed with orthorhombic cells with dislocations of the same sign stacking in the **c** direction, or the tilt grain boundary configuration. The lattice parameter correction as provided by Lehto *et al.* has been applied to account for the presence of the dislocations and correct any discontinuities introduced at the cell boundaries [59].

Bigger *et al.* have studied the 90° partial dislocation in silicon in an *ab initio* investigation. Their research motivation was that of the importance to understand the most common dislocation which occurs in plastically deformed silicon, a widely used material in semi-conductor applications [60]. Their interest was in modelling the atoms that comprise the core of the dislocation, where the greatest lattice distortion is present and continuum elasticity breaks down. However, atomistic calculations are best represented by using a supercell, a unit cell of atoms containing the defect of interest, which is repeated periodically along each supercell lattice vector. The authors state "Unless the height of the repeat cell, d, is commensurate with the periodicity of the grain boundaries, a misfit is introduced at the horizontal cell borders". They had noted that this geometrical correction had been overlooked by previous researchers, which had resulted in controversial artefacts in the form of electronic states in the band gap of silicon [60]. As a resolution to this problem, the paper suggested the requirement of at least six (or an integer multiple thereof) 90° dislocation dipoles in silicon using an orthorhombic cell to avoid introducing misfit at the cell boundaries. They also added that to use just a single dipole of dislocations, an oblique cell, creating the quadrupolar arrangement of the dislocations is necessary. The correction (eq. (3.28)) is added to the lattice vector parallel to that defining the area of slip, $d\mathbf{A}$, in the direction of the Burgers vector,

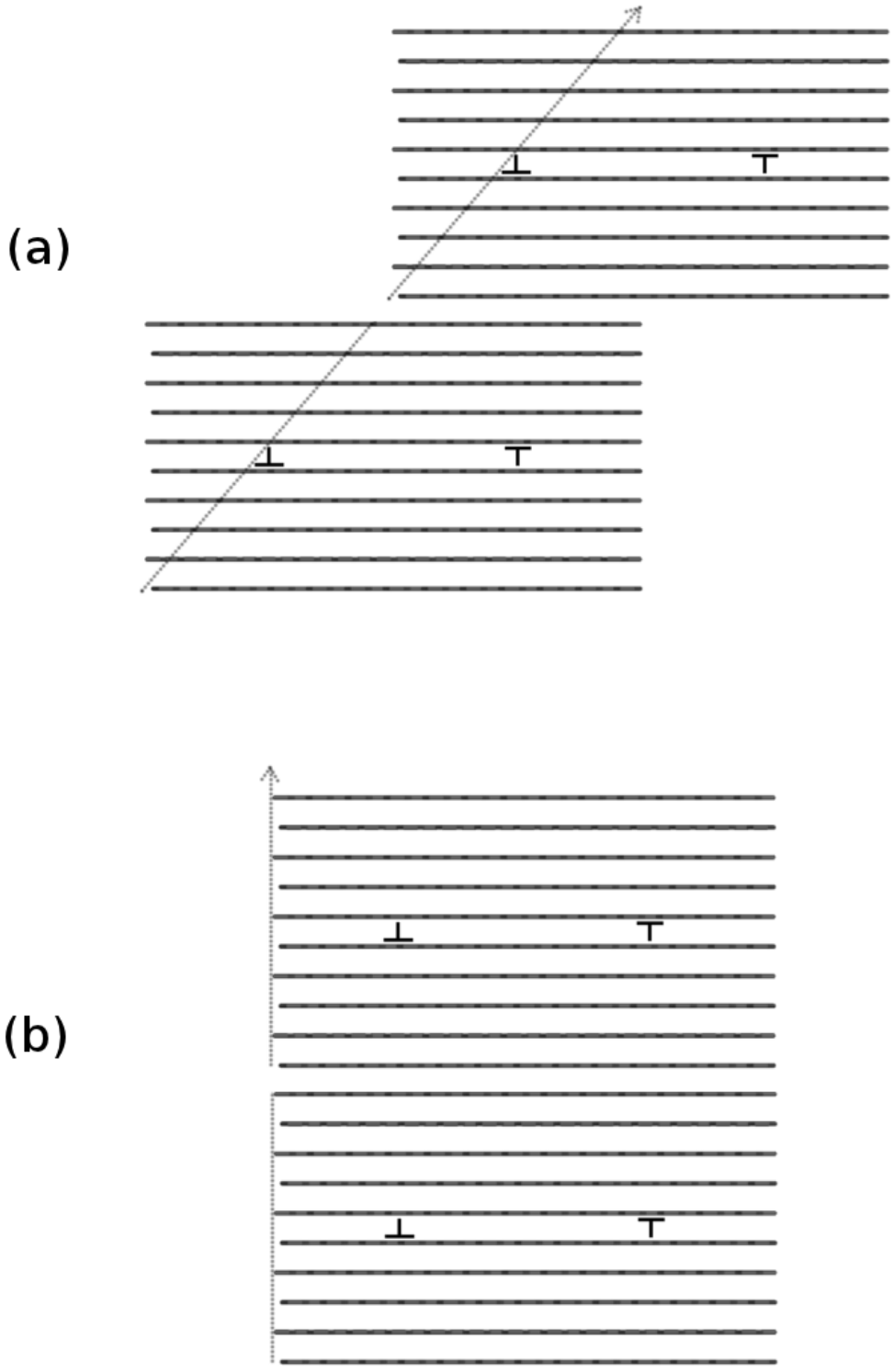

Figure 3.16: The location of the partial dislocations in the supercell scheme, showing the two sets of lattice parameters to create (a) a quadrupole configuration or (b) a grain boundary like configuration

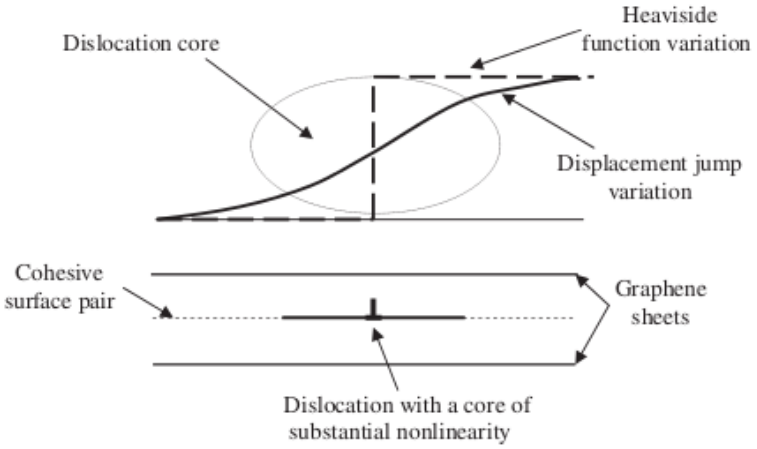

Figure 3.17: A schematic of the model implemented by Yang *et al.* showing the large dislocation core and the cohesive surface at the centre of buffer layers. Image reproduced from [35]

b. Thus, for a dipole of basal dislocations, the correction is added to the **c** lattice vector, in the direction along the basal plane. Hence an orthorhombic cell becomes monoclinic, as shown in figure 3.16. The result found by Lehto and Oberg is in contrast to that calculated by Bigger *et al.* [60].

$$\Delta \mathbf{c}_i = -\mathbf{b} \int_A \frac{\mathbf{c}_i \cdot d\mathbf{A}}{|\mathbf{c}_1 \cdot (\mathbf{c}_2 \times \mathbf{c}_3)|} \tag{3.28}$$

Yang *et al.* present a nanoscale continuum approach for modelling the core of a basal dislocation in graphite [35]. Their method involves treating graphite as a stack of buffered Kirchoff plates. Some of these plates represent the individual graphene sheets, whilst the others act as buffer layers representing the interactions between the layers (see figure 3.17). Within the buffer layers, cohesive surfaces are defined in such a way that the interlayer interaction is governed by a 4-8 Lennard Jones potential. However, such a potential underestimates the shear strength, C_{44}, and as such the authors implement a separate potential, as defined by Telling and Heggie [28], to describe any tangential basal deformations.

Chapter 4

X-ray diffraction

X-ray diffraction techniques have played an instrumental role in the determination of crystal structures in the past century [61]. X-rays are able to produce diffraction images from crystals due to their very short wavelength, comparable to inter-atomic distances. The non-destructive nature of X-rays makes it a highly attractive experimental imaging technique when compared to electron or neutron scattering where, in order to achieve high resolution the particles possess very high energies, consequently introducing a threshold at which the sample under investigation begins to damage. X-ray images may be taken multiple times from the same sample with the guarantee that the internal structure has not been affected by the measurements. X-ray diffraction was first discovered by William Bragg and son, who demonstrated that crystal planes diffract X-rays to the same effect that had previously been shown for visible light through diffraction gratings [62]. There are two methods by which crystals are normally analysed using X-rays, one is that of single crystal diffraction and the other, powder diffraction. Identification of a crystal structure using single crystal diffraction relies on a pure, homogeneous sample representative of a single crystal of the material of interest. The sample is exposed to monochromated X-rays, resulting in defined diffraction spots which may be attributed to crystal lattice planes. Powder diffraction utilises a sample comprised of many individual crystals that are randomly oriented such that the

contributions from all of the possible reflection planes have their contributions to the diffraction pattern projected simultaneously onto a 2D plane creating a rotationally symmetric diffraction pattern.

Diffraction images obtained from samples of graphite can be used as a measure of crystal disorder [63]. The images in figure 4.1 show a side of view of the layer planes of graphite with the use of selected area electron diffraction (SAED) and the corresponding x-ray diffractograms. The view in the electron micrograph image is along the basal plane and illustrates the nature of the plane deformations as a result of irradiation by neutrons with an energy of at least 1 MeV. The images show varied orientations of the layer plane normal direction as well as broken planes. However, there are regions of the crystal that have little contrast and any defects here are unclassifiable by eye. It is highly unlikely that the broken planes terminate in the material with dangling bonds, with *ab inito* calculations estimating that unterminated edges have an energy cost associated with them, those being 3.77 eV per atom for zig-zag edges and 2.65 eV per atom for armchair edges [64]. Asthana attributes the dimensional change of the crystal to a number of contributions as a direct result of atom displacements. Those contributions come from such defects as the fragmentation of the structure into nanocrystallites, which may contain dislocation loops, a reduction in the stacking efficiency of the layer planes resulting from interstital atoms, and induced bending and breaking of planes [65].

Diffraction techniques may also be used as a method of measuring the quality of graphite during the process of graphitisation [63]. As the graphitisation temperature is increased, it can be seen that the diffraction spots in the images become progressively more defined, and at about 3000 K, the graphite has a very well defined structure with (0002) spots and $(10\bar{1}0)$ spots becoming more circular and less diffuse [30].

Leyssale *et al.* have presented a method for the reconstruction of three dimensional

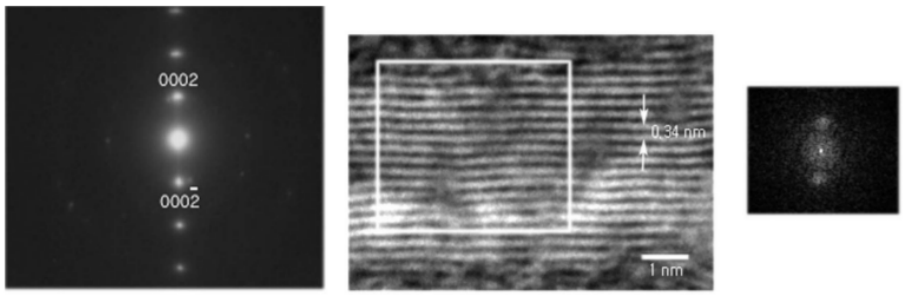

(a) Unirradiated sample of HOPG graphite

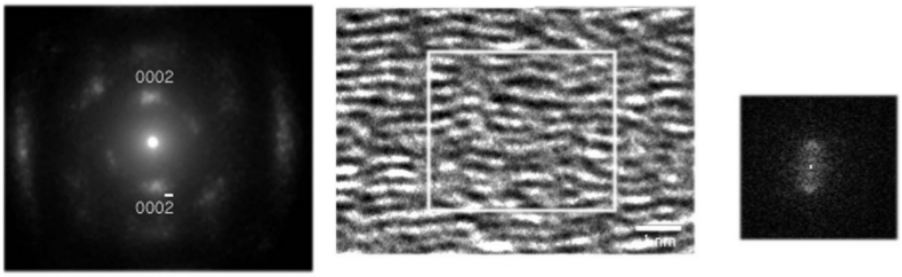

(b) HOPG sample irradiated to $3.2\text{x}10^{20}\text{n/cm}^2$

Figure 4.1: Images showing the effect of neutron irradiation on the structure of graphite as determined by XRD (left) and SEM (centre). Reproduced from [65]

nanotextured carbons from two dimensional HRTEM images [66]. Their technique has been named Image Guided Atomic Reconstruction (IGAR) in which a model is created from the contrast in the HRTEM images. The initial step to generate the model involves the creation of three dimensional target statistics from two dimensional reference statistics using 2D/3D statistical inference [66]. The construction of an atomistic model begins by defining a cubic region of space and filling it with carbon atoms according to the interfringe distance (d_{002}) as provided by the brightness field of the HRTEM image. The carbon atoms are initially introduced in a random fashion in accordance with the suited density of these fringes. To obtain a viable structure from this distribution of atoms, simulated annealing in the form of molecular dynamics or monte carlo simulations are performed. The computer simulations of the structure are governed by an interatomic potential energy function combined with an artificial interaction potential between the arrangement of atoms and the generated 3D HRTEM image. This function is dependent upon the greyscale level of each region of the image, for example, the function would return zero energy contribution for a black element

of space and unity for a white element (implying that a lower energy would be achieved if the atoms are settled in the darker areas of the image). A structure created using the algorithm is shown in figure 4.2. The technique may prove useful for in depth analysis of HRTEM images, which otherwise have no such equivalent analogue to real space structures.

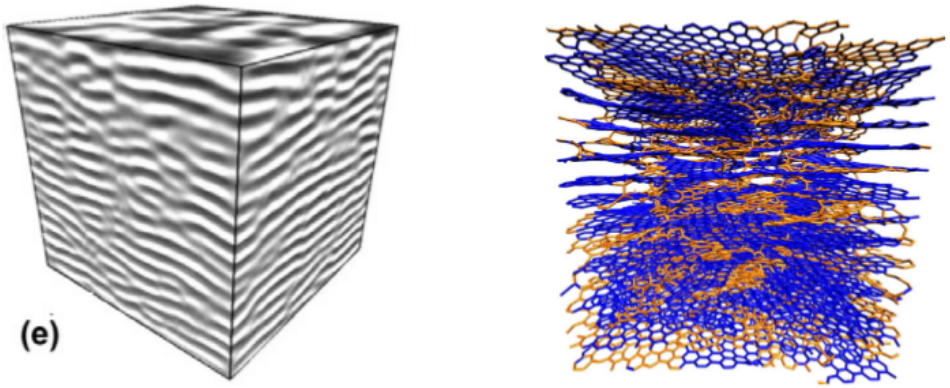

(a) HRTEM image for analysis and conversion to a real space structure

(b) The resulting real space structure after the application of Image Guided Atomic Reconstruction and a short MD relaxation at 300 K using the AIREBO potential.

Figure 4.2: The conversion of a 2D HRTEM image to a real space structure as a result of the IGAR process as proposed by Leyssale *et al.*. Reproduced from [66]

Disorder generated by irradiation of graphite or other means such as ball milling, has been visited in the literature in the form of powder diffraction experiments and simulations [67, 68, 69]. Bollmann has investigated neutron irradiated graphite at various temperatures and collected data from both energy release and diffraction studies [70]. The paper reports on experiments of irradiating samples of nuclear grade graphite to various doses at low temperatures (30 - 50°C). Upon examining the diffraction peak data, a transition dose was noted around 6x10^{20} n cm^{-2}, at which point the diffraction peak for the d_{002} starts to become asymmetrically broader and shifts to lower angles along with having diminished intensity, which represents an increase in d_{002} spacing (figure 4.3). In this temperature range, the standard model predicts the formation of point defects in the form of interstitial atoms and vacancies, but the new theory hypothesises that buckles are predominantly responsible for interlayer expansion. Bollman reported that **c**

expansion occurs in a linear fashion up to a saturation point of about 16% at 4 x 10^{21} n cm^{-2} [70].

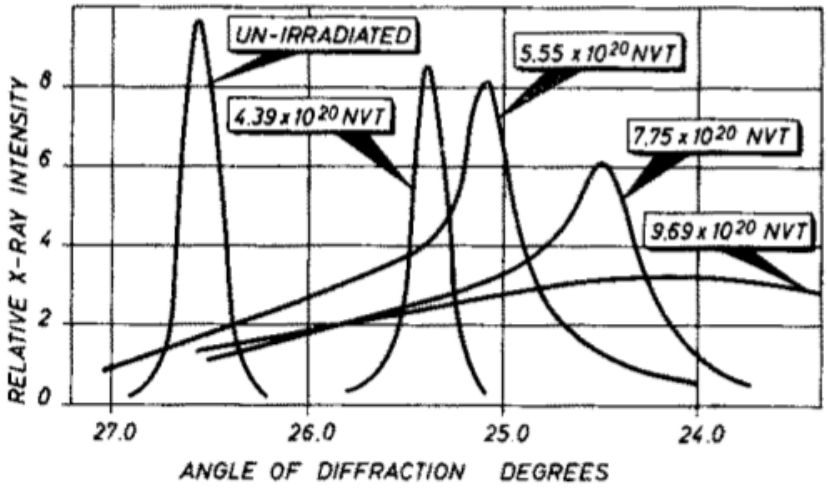

Figure 4.3: The change in the d_{002} diffraction peak in graphite with increasing neutron fluence. Image reproduced from Bollmann [70]

Diffraction simulations have been performed on structures containing dislocations and folds. These results are compared to experimental data collected from diffraction studies on neutron irradiated graphite. There are two main objectives of this chapter. One is to see if folds reproduce the patterns from experimental findings, and secondly to see if folds and dislocations produce mutually exclusive patterns, to reduce ambiguities when interpreting x-ray data from graphite samples containing line defects.

4.1 Elastic Scattering of Waves in a Crystal

The process by which a crystal structure is determined using diffraction is firstly to assume that rays impinging on a sample undergo specular reflection. That is, the incident angle of the beam is equal to that of the reflected. The atoms in a crystal lattice form reflective planes defined by Miller indices (hkl) the reciprocal of each index is the fractional distance along the lattice vector at which the Miller plane intersects it. When the path length difference between two rays

reflected from adjacent planes is an integer multiple of the wavelength of the wave or particle used, constructive interference of the waves occurs and diffraction spots are observed at angles predicted by Bragg's law (4.1). A crystal sample is exposed to a monochromatic beam of radiation, for which the wavelength is precisely known. The specimen is rotated through various angles and diffraction spots recorded as the Bragg condition is fulfilled at specific angles. These angles are used to determine the spacing between adjacent Miller planes. Structures with atoms located in the (002) plane, such as body centered cubic (BCC) and face centered cubic (FCC) are missing some of the expected reflections due to destructive interferece with the (001) reflections. In these cases, a range of planes that produce diffraction spots need to be found in order to determine the unique identity of the crystal structure.

$$n\lambda = 2d_{hkl}\sin\theta \tag{4.1}$$

Where n is the order of diffraction, d is the interplanar spacing between the set of (hkl) planes and theta is the angle between the beam and the sample. The Bragg equation only provides the angles at which to expect diffraction spots, but includes no details regarding the intensity of the diffracted beam. Some other properties of the lattice are required for this to be determined. The contribution of a single atom to a scattered wave detected a large distance from the sample is made up of three factors [71].

$$A_r = A_0 e^{i(\mathbf{k}\cdot\mathbf{r}-\omega t)} \times f \times \frac{e^{ik|\mathbf{R}-\mathbf{r}|}}{|\mathbf{R}-\mathbf{r}|} \tag{4.2}$$

Where the first term describes the incident wave, f is the atomic scattering factor and the last term represents the amplitude decrease and phase change from a point source at the position of the atom. For large distances $\mathbf{R}$, the vector $\mathbf{r}$ becomes

negligible.

The scattering factor f depends on the atom-light interaction, and in general depends on the scattering angle 2θ. The last term in the equation relates to the amplitude decrease and phase change associated with each atom. The amplitude decrease is approximately the same for all atoms and the denominator in this term may be replaced with R, the distance to the detector. The same replacement may not be made for the phase as this term has a significant effect on the intensity of the diffracted beam. For elastic scattering, the wavenumber and frequency of the incident beam remains unchanged after diffraction. The wavevector $\mathbf{k}'$ of the diffracted beam is, to a good approximation parallel to both $\mathbf{R}$ and $\mathbf{R} - \mathbf{r}$, and as such, the amplitude is proportinal to the sum shown in equation (4.3).

$$A = \sum_n f_n e^{-i\mathbf{K}\cdot\mathbf{r_n}} \tag{4.3}$$

$\mathbf{K} = \mathbf{k}' - \mathbf{k}$ is called the scattering vector. A crystal may have a basis of more than one atom associated with each lattice point, in which case the coordinates of the n^{th} atom may be written as

$$r_n = r_l + r_p \tag{4.4}$$

Expression (4.4) denotes the position $\mathbf{r_n}$, of atom n as a sum of two components. $\mathbf{r_l}$ is the position of the lattice point from some origin with which atom n is associated and $\mathbf{r_p}$ is the position of the atom relative to this lattice point. This sum allows the splitting of equation (4.3) into two components, the first is a sum which predicts the angles at which diffraction occurs, determining the crystal lattice. The second is called the structure factor, and determines the relative

intensities of the diffracted beams.

$$A = \sum_{l} e^{-i\mathbf{K}\cdot\mathbf{r_l}} \sum_{p} f_p e^{-\mathbf{K}\cdot\mathbf{r_p}} \tag{4.5}$$

As well as determining the structure of perfect crystals, the technique can provide valuable information regarding crystallite size, size distribution and dislocation structure. XRD peaks in powder diffraction methods change in the presence of defects. Peak broadening indicates that crystallites have become small or that defects have become highly abundant, for example a dislocation density of more than $5\text{x}10^{12}\text{m}^{-2}$ would be required for noticeable changes to the diffraction pattern [72]. The method is sensitive to strain inducing defects, common sources of which are dislocations, stacking faults and grain boundaries to name a few. Defects are apparent in diffraction images as deviations from, and alterations to the perfect crystal's diffraction pattern. In single crystal images the size, shape, position and intensity of diffraction spots may all change in the presence of defects. It has been shown that following neutron irradiation, the diffraction pattern of graphite can change in distinctive ways [73], namely the broadening of the (0002) spots and diffuse streaks passing through ($hkl0$) diffraction spots. These same occurrences, particularly that of the broad (0002) spots are also exhibited during the graphitisation process, suggesting some structural similarity between neutron irradiated and partially graphitised samples of graphite [30]. It is these most noticeable changes that have been sought in the simulated images from the models presented here.

X-ray diffraction images formed part of the most convincing evidence for the existence of carbon nanotubes (CNTs) [74]. The nature of buckles and folds can have similar geometric properties to nanotubes such as the introduction of curvature and therefore x-ray diffraction may be able to provide strong grounding for the existence of these features within bulk irradiated graphite. However, X-ray

diffraction data alone cannot conclusively determine the nature of disorder in a crystal [75].

4.2 The Ewald construction

The reciprocal lattice of a Bravais lattice may be obtained by the Fourier transform of the real space crystal, such that the periodicity of the lattice d_{hkl} becomes $1/d_{hkl}$. The shape of each reciprocal node is the Fourier transform of the crystal shape, for example, a long thin crystal implies elongation of the reciprocal nodes, which in turn implies that a mathematically infinite crystal will produce no diffraction spots. The transform of a beam of x-rays of wavelength λ impinging on a crystal forms the Ewald sphere with a radius equal to λ^{-1}. Scattering of the incident beam occurs when the Ewald sphere intersects a reciprocal lattice point. More reciprocal lattice nodes may intersect the Ewald sphere if the radius of the sphere is increased, which may be achieved by using a very thin sample, causing elongation of the nodes, or by decreasing the wavelength of the incident beam. Switching the source of the incident radiation is possible, such as from x-rays (λ for Mo-Kα radiation is 0.709 Å) to electrons, the relation between the beam voltage and the wavelength of the accelerated electrons is given by equation (4.6).

$$\lambda = \frac{h}{\sqrt{2m_0 eV_0\left(1 + \frac{eV_0}{2m_0c^2}\right)}} \tag{4.6}$$

Where m_0 is the mass of the electron, e is the elementary charge and V_0 is the beam voltage. For a modest voltage of 10^4 kV, the resultant wavelength of the electrons in the beam is 0.001 Å, which is already a large increase in possible resolution over X-rays. The use of high energy electrons (large Ewald sphere) in conjunction with a thin crystal sample (elongated reciprocal lattice nodes) produces the greatest chance of achieving diffracted rays. The Ewald sphere generates Laue

zones, discrete rings containing diffraction spots. These rings are separated by blank regions where the conditions for diffraction are not satisfied [63].

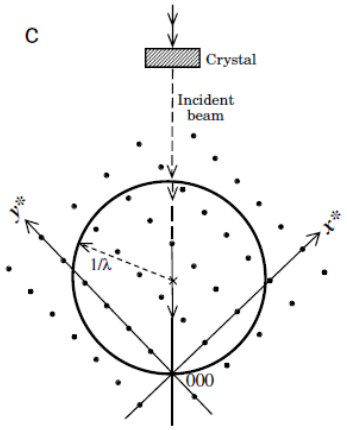

(a) Two dimensional representation of the Ewald sphere interacting with the lattice. In this instance, no nodes are intersected, hence no diffraction would occur.

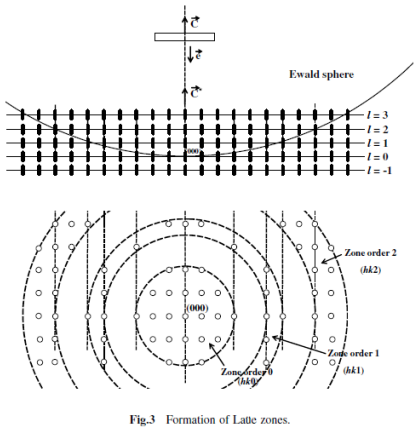

(b) Laue zones produced by interaction between the Ewald sphere and the reciporcal lattice nodes.

Figure 4.4: Image reproduced from [63]

The direct transfer from the diffraction pattern to the real space atomic structure is not possible. It is however, possible to extract information about the sample by using a Fourier transform of the spot intensities, I_s. The transform provides information about the distribution of atomic distances $P(x)$ in the crystal. As disorder in the crystal increases, $P(x)$ and I_s become more continuous in the limit of a gas-like scattering at which point the two distributions are continuous in reciprocal space [63].

Chapter 5

X-ray diffraction on graphite

The structure of graphite changes when it is irradiated with neutrons [15]. The layered nature of graphite creates a contrast in properties along two direction of particular importance. X_a denotes the length of a crystal sample along the basal plane direction whilst X_c denotes the length dimension in the direction out of plane, normal to X_a. See figure 5.1.

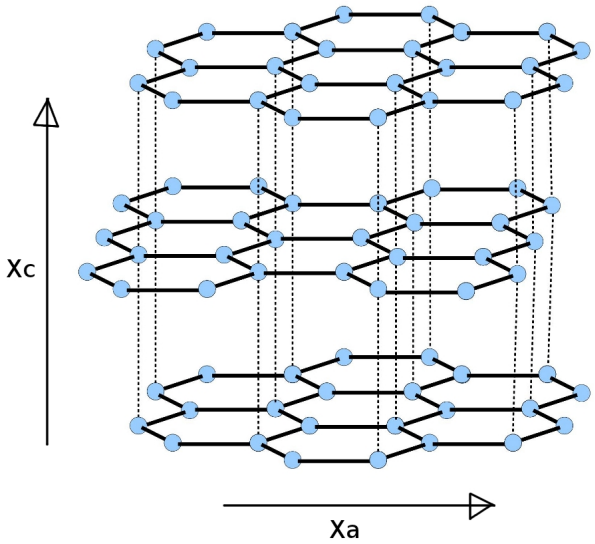

Figure 5.1: Diagram highlighting the two length dimensions along different directions in graphite crystals, X_a and X_c

In the case of single crystals, the X_c dimension expands, whilst the X_a direction contracts. The ratio of ΔX_c to ΔX_a is highly dependent on the temperature at

which irradiation takes place [15]. The expansion is evident in powder diffraction experiments by a shift in the angle at which the (002) peak is measured, shown in figure 5.2. This peak also broadens asymmetrically, with a bias towards smaller angles indicating an increase in average interlayer distance. The (002) diffraction spot also broadens in single crystal images, suggesting a range of values for the interlayer distance possibly caused by an effect such as mosaic spread or Mrozowski cracks [30].

Diffraction simulations were undertaken using the CrystalMaker software package [76]. Procedures include stationary view images along high symmetry directions in graphite as well as precession diffractograms for the ruck and tuck defect. Graphite cells containing dislocation dipoles, folds and prismatic loops were created for the purpose of structural optimisation and X-ray diffraction simulations in order to compare with results in the literature.

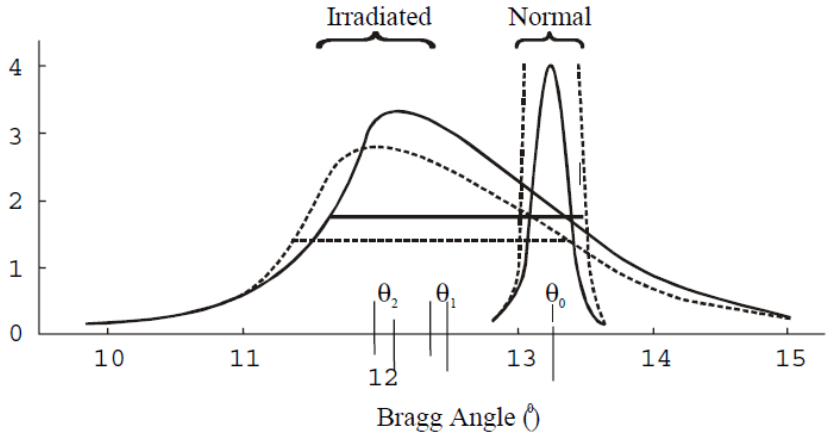

Figure 5.2: Powder diffraction plot of angle against intensity. Plot shows {0002} peak shift in graphite after irradiation.

One of the motivations behind performing X-ray diffraction simulations was due to the availability of experimental images obtained from samples of neutron irradiated graphite. One particular investigation of interest is that by Eeles [73, 75], who performed diffraction experiments on Ticonderoga graphite[1] samples irradiated with neutrons to a dose of $2\text{x}10^{20}$ n cm^{-2}. The results showed distinct changes

[1] A source of natural graphite obtained from the Ticonderoga region in the state of New York

to the diffraction patterns of graphite after neutron irradiation at 200^{o}C. One of these attributes was the presence of diffuse lines connecting diffraction spots along the $(10l)$ lines, consistent with random shifts along the $\langle 11\bar{2}0\rangle$ (zig zag) direction, but the author concluded that there was no known defect which could cause such an effect [73]. Another change to the pattern was consistent with expansion in the **c** direction, vertical extension of the $(000l)$ spots, which also spread out horizontally. The images produced from Eeles investigation are shown in figure 5.3, from which comparisons will be drawn for the single crystal simulations. The various structures that have been generated and structurally optimised have been used to investigate the effect of dislocations and folds on the diffraction patterns compared with that of virgin graphite.

A paper by Keating and Goland investigated the effect of the presence of prismatic loops on the diffraction pattern of graphite by computer simulation [77]. The investigation was in response to the images produced experimentally by Eeles to see if the dramatic changes to the virgin graphite diffraction patterns might be attributed to prismatic loops (small clusters of carbon atoms) sitting between the layers. Ohr derived the equations for the displacement field around a prismatic loop in graphite [78], which have been implemented by Keating to generate displaced atomic positions for which simulated diffraction patterns have been calculated and analysed (shown in figure 5.4). The paper concludes that the simulated XRD patterns reproduce some, but not all of the features found by Eeles, namely the streaks connecting spots $(11\bar{2}0)$ and $(11\bar{2}2)$ are not present in the simulation. A quote from a paper by Keating brings together work from two papers, stating "Ohr has also considered the stress fields produced by basal plane dislocation loops in graphite. One might suspect that the stress $\sigma_{zz}(\rho, 0)$, shown in his Fig. 5, near the edge of a loop is sufficient to rupture the weak π bonds between the basal planes. Thus a crack or large-dislocation core, as suggested by Eeles, might be produced whose extent is considerable when compared to the area of the atoms in the loop itself" [77]. The noted statement of Eeles hints at the underlying theory

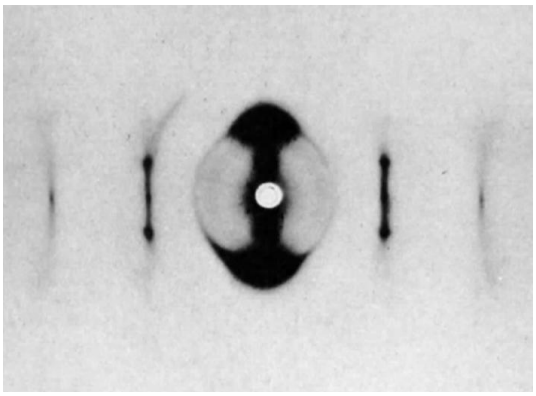

(a) 60 degree oscillation photograph about crystal's **c** direction

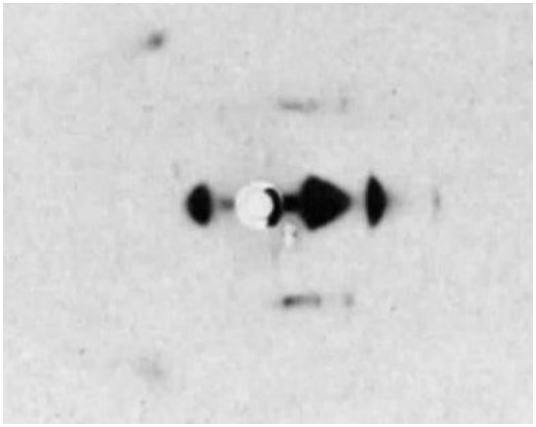

(b) 30 degree oscillation photograph about $(10\bar{1}0)$

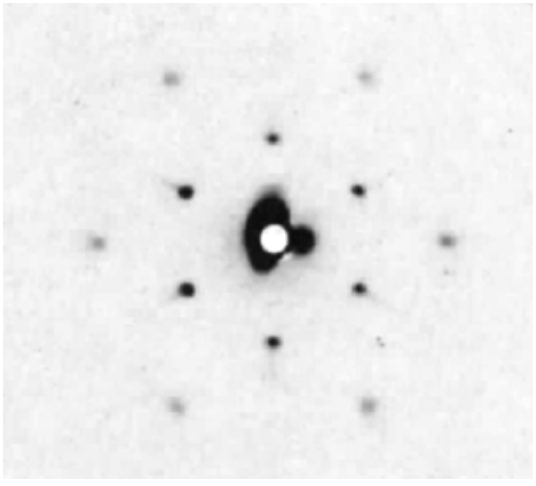

(c) Stationary photograph parallel to **c**

Figure 5.3: XRD images obtained from samples of Ticonderoga graphite irradiated to $2x10^{20}$ at 200^{o}C. Images reproduced from Eeles [73].

of the behaviour of layered materials, but the idea of wrinkling, buckling and folding were never really considered as possible mechanisms of damage in graphite

until recently [21]. The quote from Keating provides real incentive to investigate the XRD patterns produced from large cells containing confined basal dislocation dipoles. It should be noted that the quote from Keating is in error by suggesting that π interactions govern the interlayer binding, as the π bonds in graphite exist parallel to the basal plane between the p_z orbitals and contribute to strengthening the in-plane σ bonds between nearest neighbour atoms. The interlayer binding comes from overlap of the π systems in adjacent layers, as well as a contribution from London dispersion forces [3].

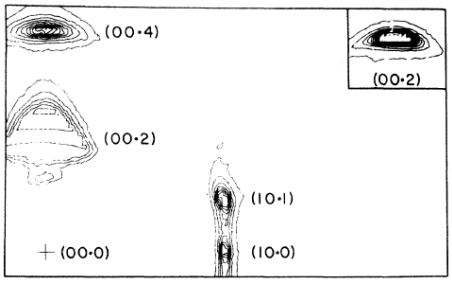

(a) Eeles' precession photograph converted to show contours denoting regions of equal diffraction intensity.

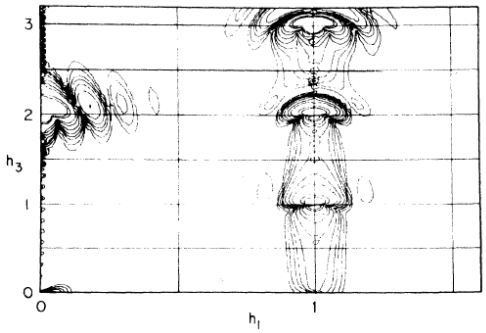

(b) Keatings' simulated diffraction intensities for the model influenced by the presence of a prismatic loop

Figure 5.4: Comparing the images produced by (a) Eeles diffraction experiment and (b) Simulated diffraction by Keating. Images reproduced from [77].

5.1 Simulated x-ray diffraction results

5.1.1 Virgin graphite patterns

The diffraction simulation software was tested using a perfect graphite cell as a benchmark. Accurate results here would bring some confidence in any further results obtained using this method. Figure 5.5 shows the results from single crystal images of the perfect graphite cell. The images are XRD simulations, with a wavelength of 0.07 nm and a sample thickness of 10 nm. Alongside each of the diffraction images are pictures of the real space crystal and select Miller planes associated with the generated spots.

The reciprocal lattice of graphite has been faithfully reproduced, with the characteristic hexagonal lattice shown in the **c** direction, and several orders of the $(000l)$ diffraction spots coming from the interlayer distance. Some higher order spots that aren't typically seen in experiments have been reproduced due to the perfect long range cystalline structure in the model cell. These images will help to identify changes in the diffraction patterns produced from the simulations obtained from the variety of defects being modelled.

5.1.2 Simulated diffraction from dislocations

A number of integer multiples of 90° partial basal dislocations were introduced into large unit cells and subsequently optimised using GULP. The resulting structures were used to generate TEM simulated images with the CrystalMaker software package. The first of the dislocation structures for simulation contained just one dipole of 90° partials. Subsequent structures that were studied contained dipoles of two, three, four and seven dislocations. The results from the X-ray diffraction simulations are shown in figure 5.7.

The image 5.6a shows vast asymmetrical broadening of the (0002) diffraction

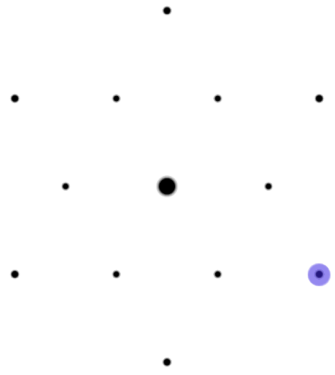

(a) Beam along layer plane normal direction $\langle 0001 \rangle$

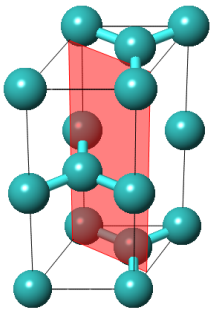

(b) $\{2\bar{1}0\}$ Miller plane

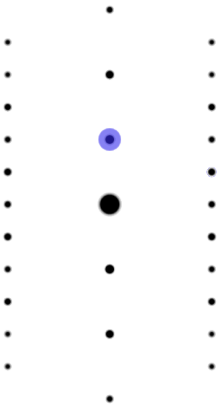

(c) Stationary image with view along zig-zag $\langle 11\bar{2}0 \rangle$ direction

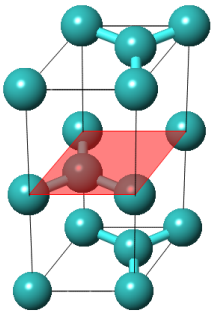

(d) $\{002\}$ plane

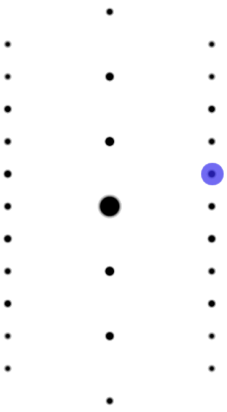

(e) Stationary image with view along zig-zag $\langle 11\bar{2}0 \rangle$ direction

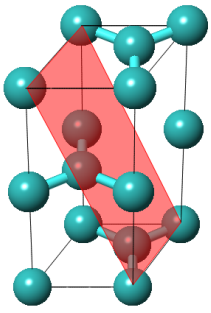

(f) $\{0\bar{1}1\}$ plane

Figure 5.5: Diffraction spots from perfect graphite and Miller planes associated with the highlighted spots.

spots, resembling the images of low temperature irradiated samples of graphite presented by Eeles [73]. The streaks connecting the direct beam spot and (0002)

(a) View along dislocation line direction $(11\bar{2}0)$

(b) Stationary photograph with view parallel to **c** direction

(c) Stationary photograph into armchair direction, view along $(10\bar{1}0)$

Figure 5.6: XRD images from a structurally optimised cell containing a dipole of 4 x 90° partial dislocations

spots have also been reproduced. Figure 5.6b differs greatly from the virgin graphite equivalent. The lines of spots between the normal $(hkl0)$ spots are due to disregistry of the layers resulting from the buckling. It is not clear why the intensity along central line is orders of magnitude greater than the others.

The literature has an abundance of images of defects in graphite, however, very little high resolution imaging has been performed on neutron irradiated graphites. The most extensive investigation is that of Thrower [13]. Other models which were created for the purpose of diffraction simulations include interstitial dislocation loops, and folds. Both of these defects introduce curvature in the normally flat graphite planes. It will therefore be insightful to see if similar traits are produced

between the diffraction patterns of each.

5.1.3 Prismatic interstitial loops

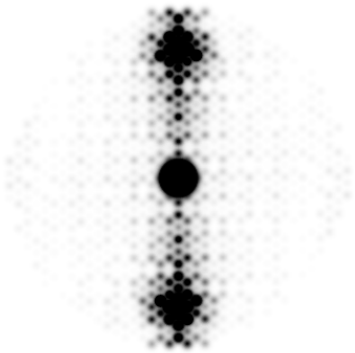

(a) Stationary image looking along zig-zag driection $(11\bar{2}0)$

(b) Stationary image looking along armchair $(10\bar{1}0)$ direction

(c) Stationary image looking into **c** direction

Figure 5.7: XRD images from a supercell containing interstitial loops of 0.7 nm radius. Lack of spots $(10l)$ spots relative to perfect XRD images implies loss of registry. There is very little evidence of streaks, but many well defined spots around the (0002) region. The overall shape of this diffraction area is in agreement with the prediction by Keating for loops in the basal plane [77]

The diffraction images of the prismatic loops are in agreement with predictions by Keating for the presence of intersitial dislocation loops in the basal plane of graphite [77]. That is, broadening of the $\langle 0002 \rangle$ spots and diffuse scattering along the $\langle 00l \rangle$ direction. However, the spots pertaining to the $(10l)$ lines are missing,

which is predicted to be a result of disregistry between the planes and not due to the bending of them, as this is a relatively local effect in comparison to the size of the loop and the cell. This may be a shortcoming of the interlayer potential used in the optimisation routine, which is a Lennard-Jones potential with parameters ϵ and σ adjusted to the lattice vectors for graphite. In turn, the potential leads to an underestimate of the shear modulus by some margin [79]. However, C_{44} in graphite is drastically reduced by the presence of any stacking fault such as the slip produced by a dislocation [80], or by a relative rotation between the planes [4]. The view directly in the [0002] direction has also lost diffraction spots, picking out only scattering due to the long range periodicity of the defects. Although the structure appears to have a reasonable stacking order, evidently, enough disregistry has been generated with the introduction of prismatic loops to lose these high symmetry diffraction spots in the model.

5.1.4 Diffraction simulations from folds in graphite

The ruck and tuck is a hyopthetical defect that is thought to occur in the high temperature irradiation process in graphite (above 500 K). The loss of pinning points such as interstitials, vacancies and broken planes at higher temperatures means less hinderance on dislocation motion. The interaction of moving dislocations, resulting in a pile up, may cause buckling and subsequent folding of the planes resulting in the ruck and tuck defect. The growth of the fold may proceed by a process of annihilation climb, in which passing dislocations deposit additonal material in the end of one of the folds, and continue their motion having climbed by $\mathbf{c}/2$ [21]. Folds in graphene flakes have been observed many times in the literature [81, 82, 83]. Allen *et al.* report of chemically induced folds of graphene and instances where multiple folds occur parallel to one another implying a preferential folding direction. Intercalation materials between a substrate and graphene disrupt the interlayer bonding and spontaneously causes the graphene

to fold back on itself [81]. The author also reports that these folds are able to be very tightly curved. Raman experiments on the samples are absent of a defect peak (or D peak) in the spectra, suggesting the folds are free of defects and consist of purely sp^2 bonding, preserving the hexagonal structure of the layer, implying that such highly curved edges are stable enough to exist in the presence of intercalants.

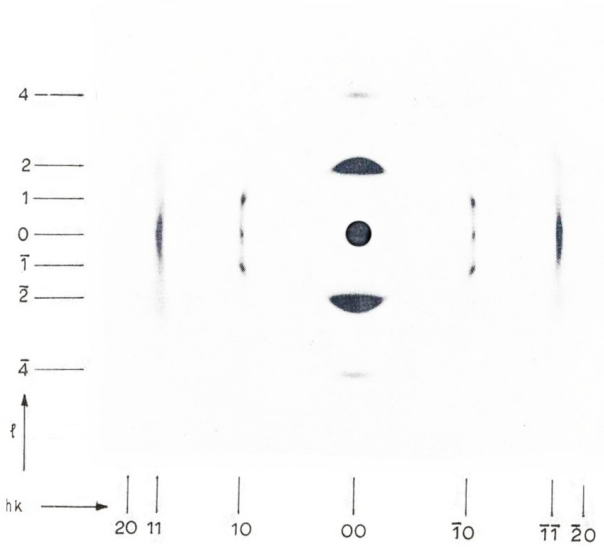

Figure 5.8: Experimental precession diffractogram produced by Eeles [75] using monochromated Mo-Kα radiation and a precession angle of 20°. The image is a composite of two precession images about different axes $[10\bar{1}0]$ and $[11\bar{2}0]$.

Kim *et al.* have also studied folds in graphene, providing evidence of the the occurrence of multiple folds in the same layer [83]. Atomic resolution TEM images display Moiré patterns between two parallel lines defining the edges of a fold. The XRD image also shows the two sets of hexagonal spots with a relative rotation angle between them associated with each layer. This effect is equivalent to that of turbostratic graphite.

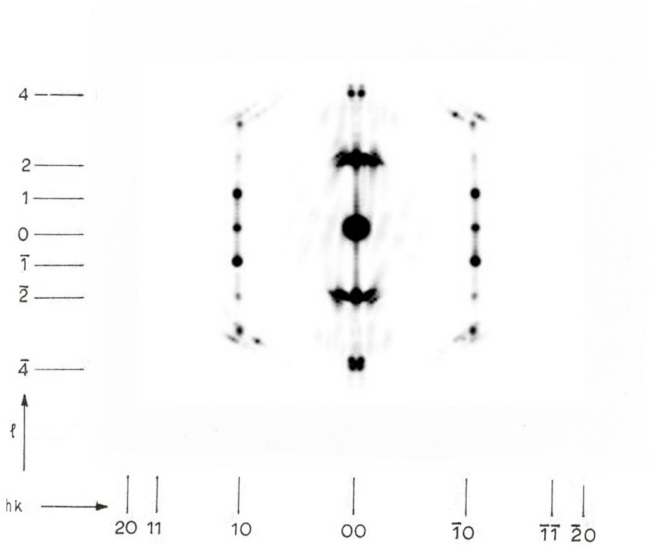

Figure 5.9: Simulated X-ray diffraction produced from a Cerius2 optimised structure using a precession of $\theta = 20°$ with a wavelength of 0.071 nm. The image is created by superimposing precessions from the two directions in the crystal as defined by Eeles.

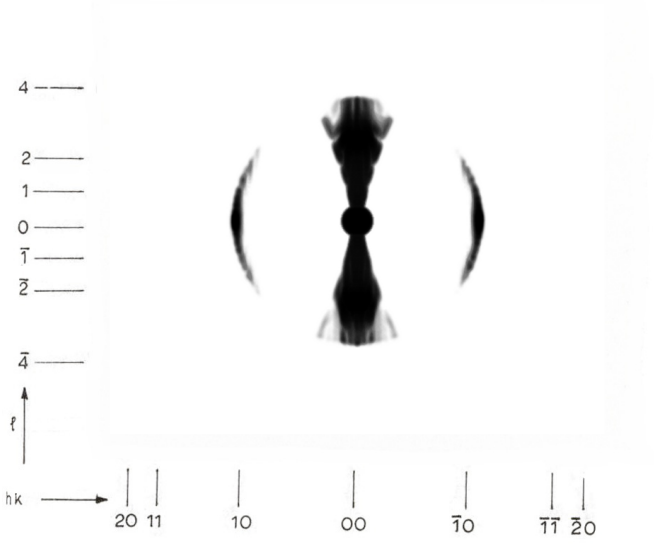

Figure 5.10: The same procedure X-ray simulation using a GULP optimised structure. Considerably more diffraction along the $(00l)$ central line relative to the Cerius2 structure and much more diffraction connecting $(10l)$ spots, to the point that they are continuous.

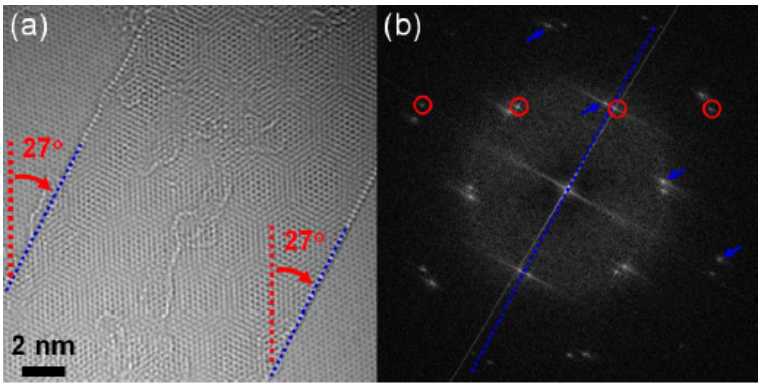

Figure 5.11: Image showing (a) parallel fold lines bounding a region displaying moiré pattern due to the relative rotation between stacked layers. (b) Fast Fourier Transform (FFT) showing the rotation with two sets of spots occurring at an angle from one another. Image reproduced from [83].

5.1.4.1 HRTEM simulation for a fold

Simulations of HRTEM images have been produced from the ruck and tuck model in collaboration with C. Seabourne from Leeds. The resulting images, shown in figure 5.12 were performed to give an idea of what might be expected in experimental images on neutron irradiated graphite that contain folds. The striations in the images are artifacts resulting from a slight perodicity mismatch in the unit cell. The cell contains 35,000 atoms and has been viewed along the line direction of the fold (that is along $\langle 11\bar{2}0 \rangle$ relative to graphite). This is an ongoing research collaboration and it is hoped that more HRTEM simulations can be generated. The goal is to investigate the images produced by looking at the fold from different angles, such as the view from the **c** direction and at a glancing angle from the curved edges, as these will all potentially provide clues towards identifying such defects in experiments.

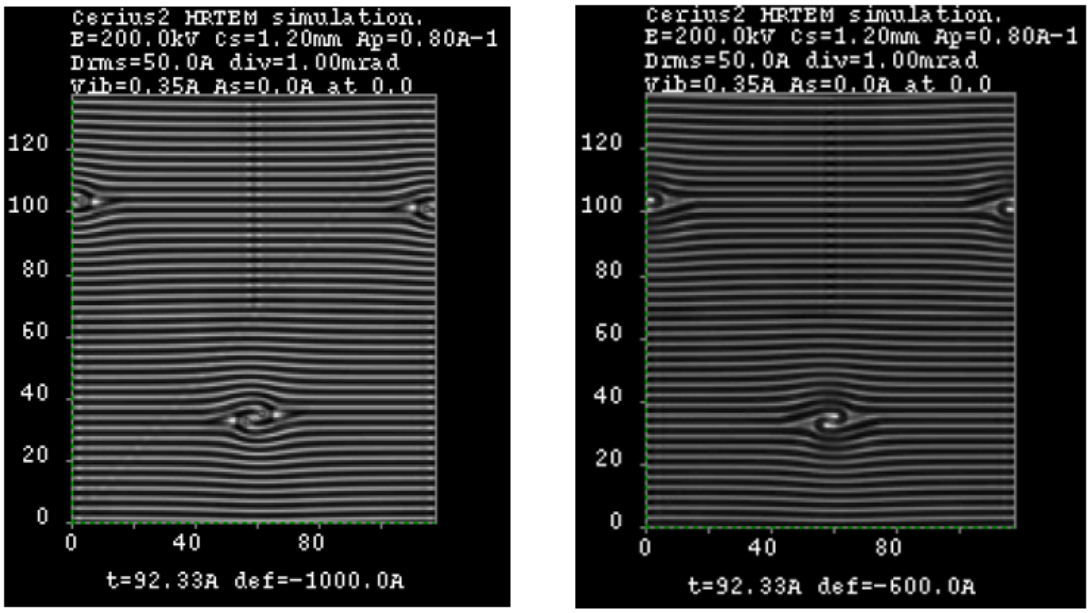

Figure 5.12: HRTEM simulations provided by Che Seabourne on the ruck and tuck defect (private communication). The two images are produced using different Scherzer defocus values, where there has been an inversion of the contrast.

The same view direction was imaged using different Scherzer defocus values [2]. The two images in figure 5.12 show an inversion in contrast between planes of graphite and the spacing between them.

5.1.5 Diffraction simulations from ridges

If a basal dislocation exists at, or near the surface of graphite with its glide plane vector normal to the layers, the resulting in-plane strain may cause delamination of the top most layers [42]. This mechanism of strain relief resulting in the formation of a surface ridge feature has been observed by Sun *et al.* with the use of high resolution Scanning Tunneling Microscope (STM) imaging [42]. Figure 5.13 shows the cone shaped ridge which has resulted from straining the graphene layer.

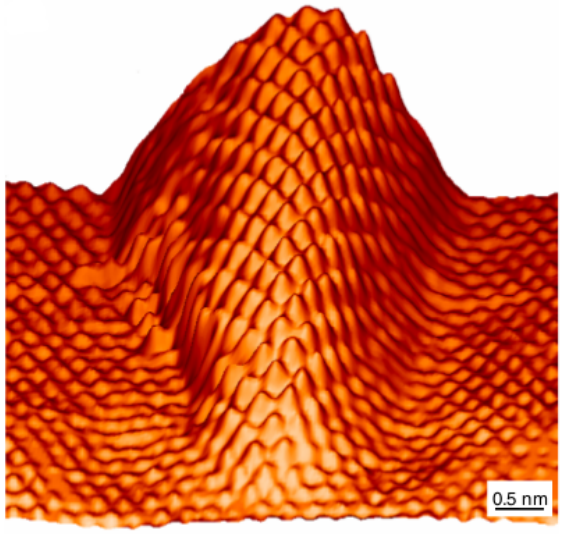

Figure 5.13: Surface ridge in epitaxial graphene on 6H-SiC substrate. Image reproduced from [42].

Luxmi *et al.* also witness ridges at the surface of graphene on a substrate of silicon carbide, although their reasoning behind their formation is not conclusive. They propose that a mismatch in thermal expansion between the SiC substrate and the sample during annealing causes induced stress in the graphene layer, which is accommodated by the formation of ridges.

[2] "The Scherzer defocus value is determined by the spherical aberration of the lens and the electron wavelength. It is different for different microscopes" [84]

In order to create a model for a ridge at the surface of a cell, the mapping routine discussed in chapter 6 has been used to transform a flat graphene strip into a cosine squared function to represent an undulation in the layer. The supercell is orthorhombic and in order to preserve the ridge during optimisation, a region of vacuum was introduced in the **c** direction to avoid interation between repeat cells. This is achieved by increasing the size of the lattice vector along the **c** direction. The diffraction simulations for the cell are shown in figure 5.14

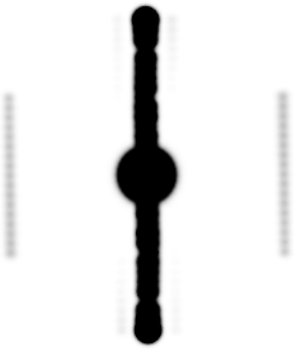

(a) Stationary image along armchair $10\bar{1}0$ direction

(b) Stationary image looking along zig-zag $11\bar{2}0$ direction

(c) Stationary image looking into **c** direction

Figure 5.14: XRD images from a supercell with a surface ridge feature. The amplitude of the ridge is 0.27 nm.

5.1.6 Diffraction simulations from screw dislocations

For completeness, a structure containing screw dislocations has been studied using the X-ray diffraction simulation software. The results from the simulations are shown in figure 5.15. The dislocations have been created in AA stacked graphite, which allows the Burgers vector to be multiples of $\mathbf{c}/2$ in magnitude rather than $\mathbf{c}$, as is the case in AB stacked graphite. The structure contains a quadrupole of screw dislocations in order to create a periodic structure. Each dislocation has a Burgers vector of $\pm\mathbf{c}/2$. The diffraction images were generated using a wavelength of 0.071 nm.

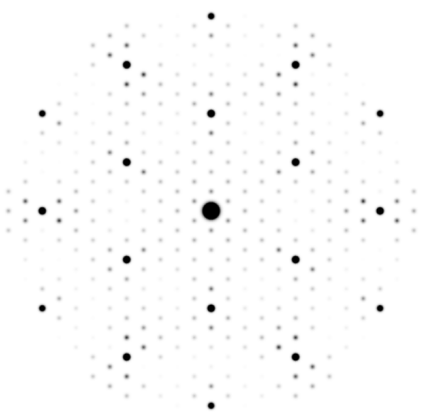

(a) Stationary image, view into the $\mathbf{c}$ direction

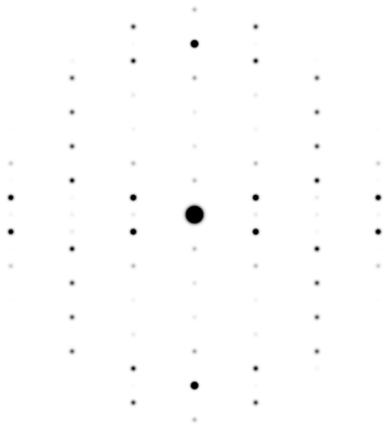

(b) Stationary image, view along $10\bar{1}0$ direction

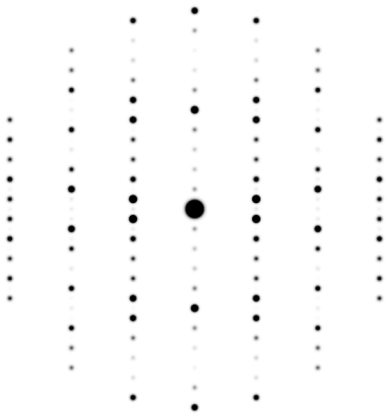

(c) Stationary image, view along $11\bar{2}0$ direction

Figure 5.15: XRD simulations on a cell containing a quadrupole of screw dislocations $\mathbf{b}=\mathbf{c}/2$ in AA stacked graphite.

It is clear from looking at these simulations that no diffuse scattering has occurred connecting the spots, only variations in relative intensities. The **c** direction image has many spots arising from the periodicity of the dislocation cores in repeated cells. Although these simulations do not provide conclusive evidence that screw dislocations do not play a role in the neutron irradiation damage model in graphite, the patterns show least resemblance to the images produced by Eeles, shown previously.

5.1.7 Diffraction simulations from turbostratic graphite

A FORTRAN program has been written, designed to generate unit cells of turbostratic graphite with a rotation defined by nanotube indices. These indices are normally used to define the chiral vector and translational vector for nanotubes, however they may be readily used for the lattice parameters of turbostratic graphite simply by the argument that the sheet will not be rolled up into a tube, but instead will be linearly periodic. The rotation angle is defined as that between the zig zag direction, denoted by indices, (1,0) and the chiral vector with indices (n,m). Turbostratic graphite cells have a minimum size due to the increased periodicity length. The new periodicity of the graphene sheet for a chiral direction is equal to the length of the chiral vector, known as the super lattice vector, the length of which may be found using a simple trigonometric relation, as shown in (5.1).

$$L_{ch} = a\sqrt{a\cos(\pi/6)^2 + a(1+\sin(\pi/6))^2}, \tag{5.1}$$

where a is the length of the basal lattice parameter for graphite. The purpose of this was to perform XRD simulations on such defects so that direct comparison with experimental results would be possible. The first of two simulations involves a periodic cell containing two layers of graphite with a relative rotation angle between them defined by indices (5,3). This amounts to an angle of 43.57° and the structure

showing its moiré pattern is provided in figure 5.16a. The second structure is the same two layers but amongst another two layers stacked in the normal AB fashion. The accurate reproduction of the diffraction spots as compared with results from Kim brings further confidence in the diffraction simulations performed here.

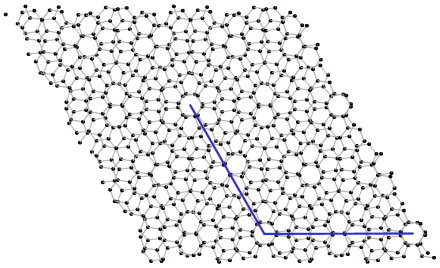

(a) Turbostratic graphite cell defined by indices (5,3), periodic lattice vector is 1.712 nm and marked with lines along each direction. The periodic Moiré pattern is visible.

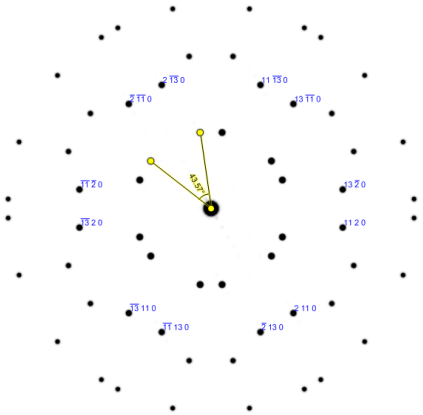

(b) The XRD simulation of the cell conatining two rotated layers. The relative rotation angle is reproduced in the hexagonal spots from each layer. Angle between equivalent spots from each layer is shown.

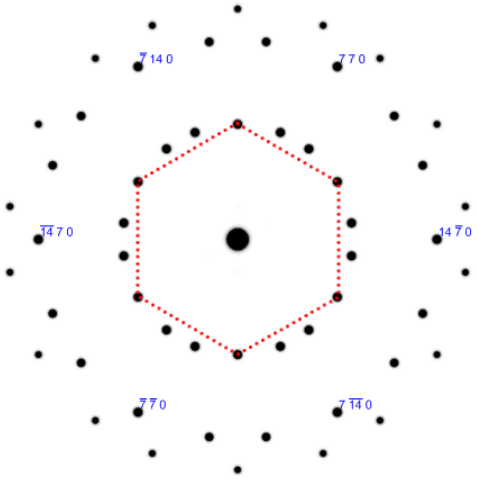

Figure 5.16: Turbostratic graphite cell defined by indices (5,3), resulting in a relative rotation of 43.6°, in addition to two AB stacked layers, a total of 4 layers per supercell. The spots labelled with Miller indices are in relation to the supercell, which is seven primitive graphite units in size. The first order diffraction contribution from the AB stacked layers is marked with dotted lines.

5.2 Powder Diffraction Simulations

Powder diffraction simulations have been performed on graphite cells containing defects which have been optimised using GULP (details of the optimisations are given in Chapter 6). The powder diffraction simulations were performed using a wavelength of 0.071 nm (Mo radiation) on graphite cells containing various defects. The simulated diffraction patterns of the defects are shown in a red line, and these are compared directly with the powder diffraction peaks from virgin graphite, the profile of which is shown in black. The peaks are labelled with indices corresponding to the supercell lattice vectors. The simulated peak profiles are shown in figures 5.17 to 5.21.

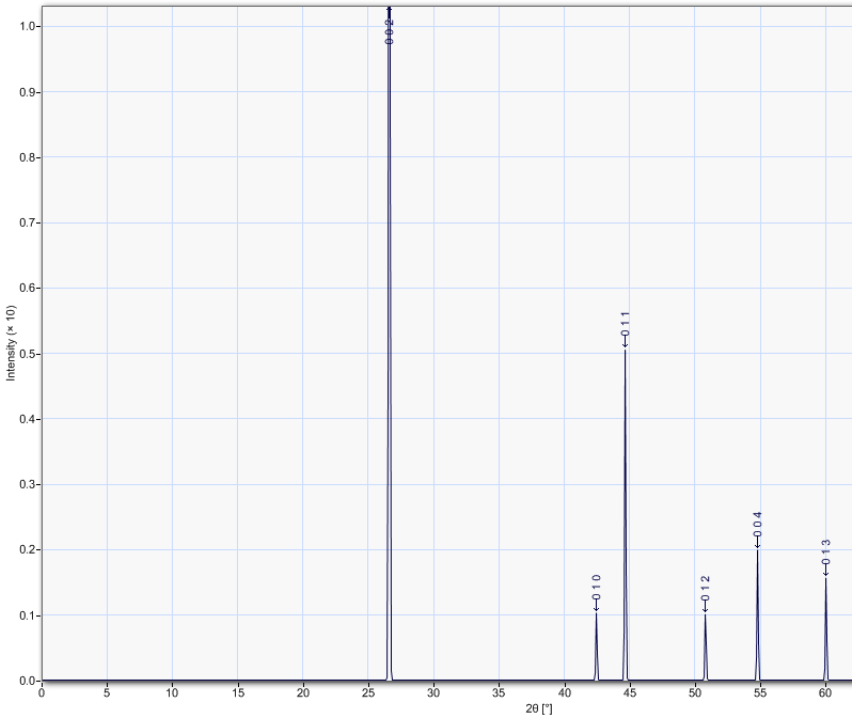

Figure 5.17: Powder diffraction peaks for virgin graphite

In all of the simlations, small angle diffraction peaks have been generated, arising due to large deformations of the system. On the contrary, none of the diffraction peaks for the large cells have reproduced higher order peaks that occur at larger angles and arise from registry of the hexagonal layers.

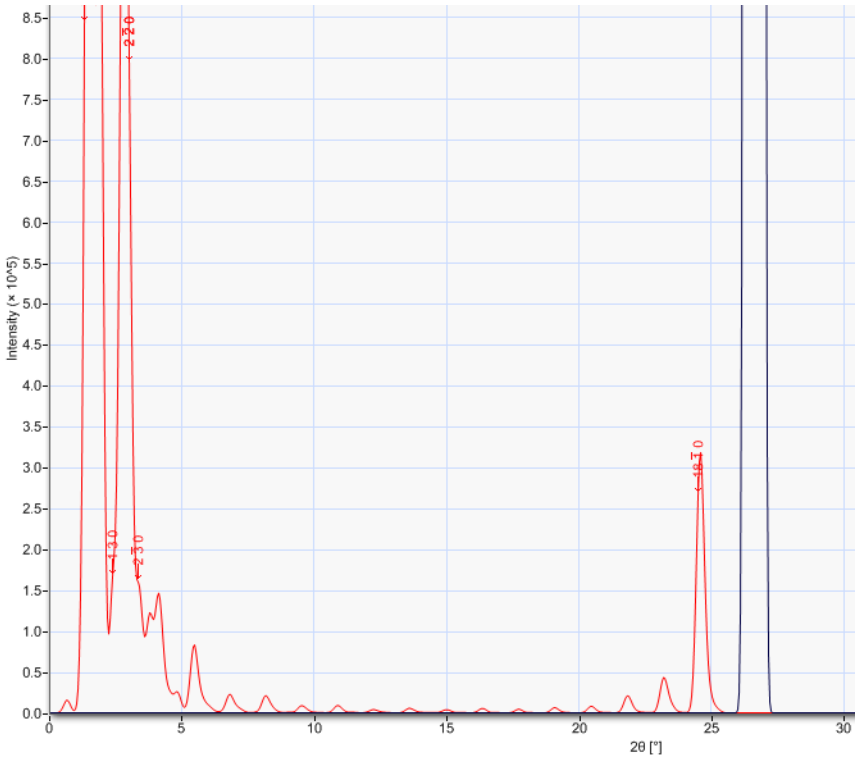

Figure 5.18: Powder diffraction peak profile for a cell containing a dipole of two 90° partial basal dislocations

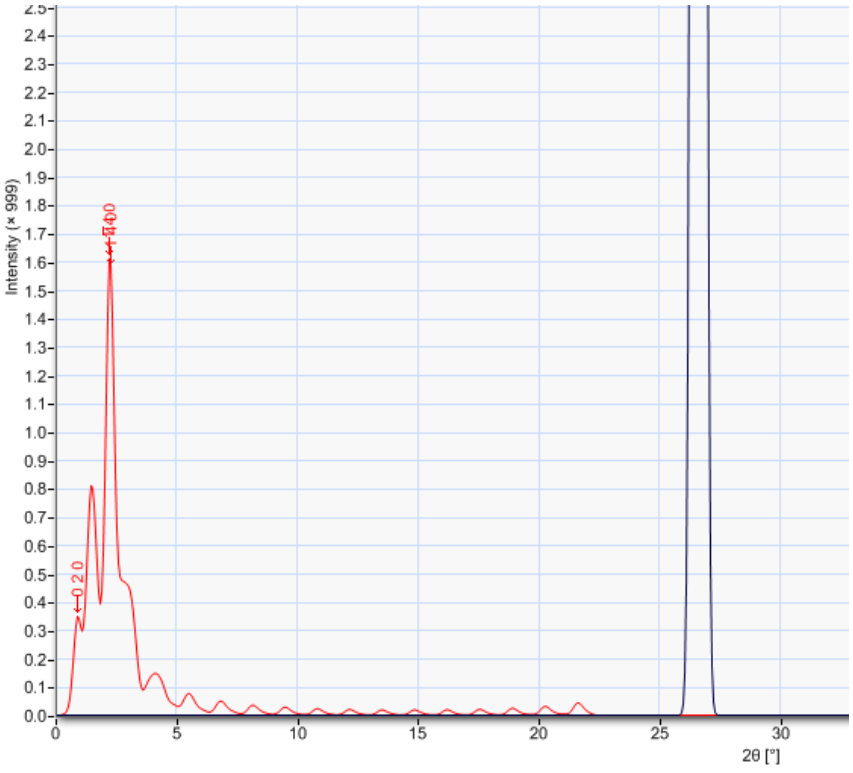

Figure 5.19: Powder diffraction peak profile for a cell containing a dipole of four 90° partial basal dislocations

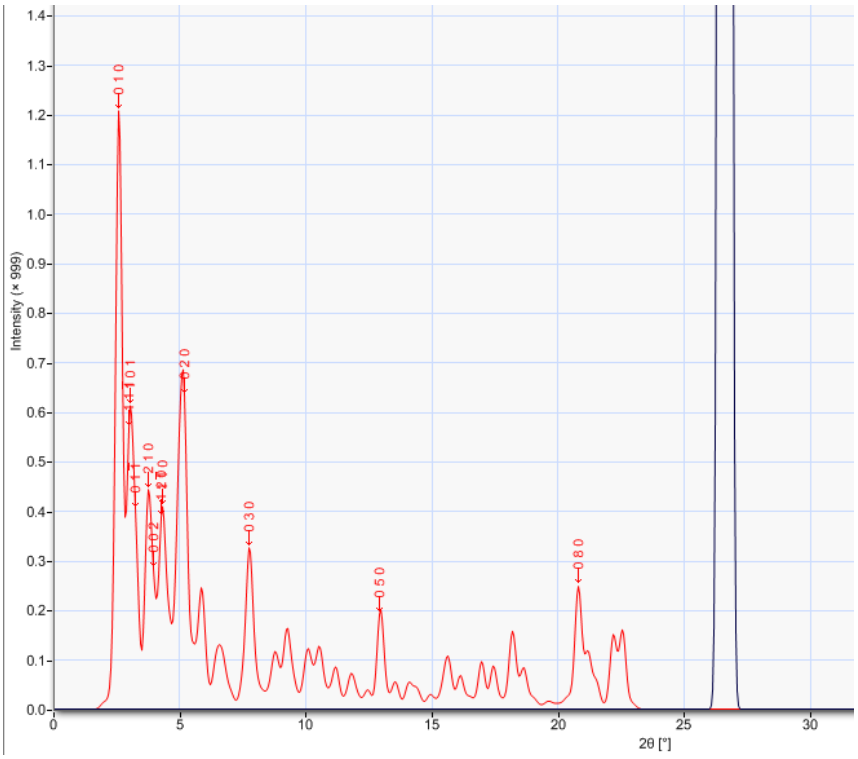

Figure 5.20: Powder diffraction peak profile for a cell containing prismatic loops of radius 0.7 nm

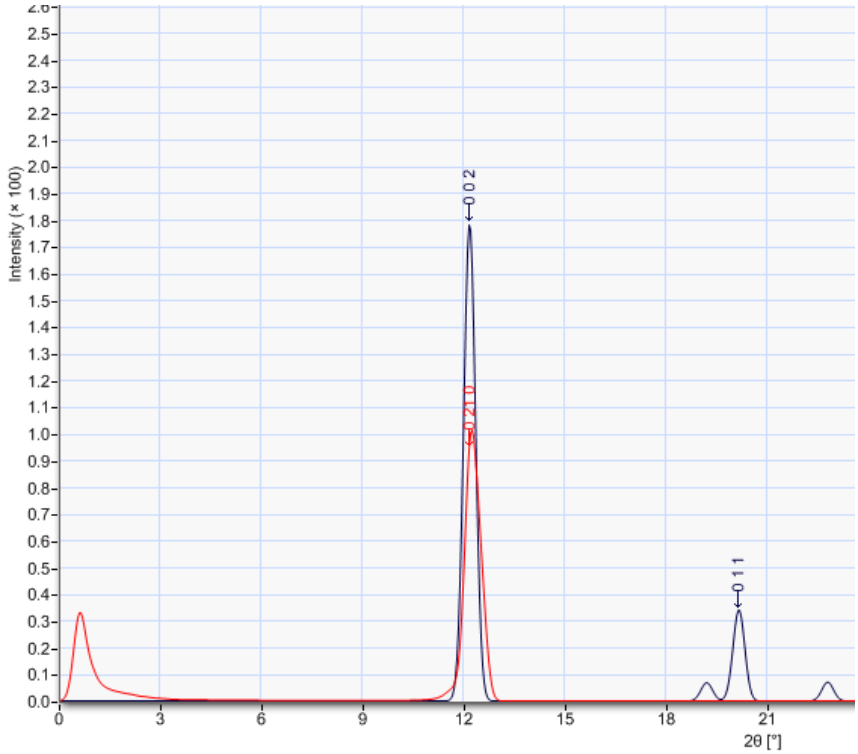

Figure 5.21: Powder diffraction peak profile for a cell containing a ruck and tuck defect, fold width equal to approximately 1 nm

Chapter 6

Graphene as a continuum membrane

In recent years, graphene has become an immensely popular focus of research after its discovery and isolation in 2004 [85]. The new material promises potential uses in many areas of science including electronics or structural enhancement of existing materials such as polymers. It is theorised that if it were possible to create a square metre of perfectly formed graphene and use it as a hammock it could support the weight of a 4 kg cat, yet it would weigh less than one of the cat's whiskers and be near invisible [86]. Despite the atomistic scale, the mechanical properties of graphene have, on several occasions been treated using continuum elasticity [87, 88, 89]. Sawada has calculated the energy of formation of CNTs as a function of their diameter using a Tersoff potential [49]. The work compares the energy cost of having dangling bonds along the edge of a graphene ribbon with that of bending the sheet into a tubule to eliminate them for a number of chiral angles. They find that the derived equation from continuum mechanics is sufficient for tubes of 1nm diameter and greater, and that the chirality has very little influence on the bending energy. The continuum approach to calculating the bending energy deviates for small radii tubules, however Sawada suggests an additional correcting term which improves the fit at higher curvatures [49]. The

correcting term involves a higher order R^{-4} component and a different coefficient to that of the R^{-2} term. Tomanek *et al.* have also investigated the stability of fullerenes and nanotubes using the energy due to bending of sheets into nanotubes. Their results are in agreement with Sawada, but it should be noted that if the energy of the tube is quoted per atom, the relationship is inversely proportional to the radius squared, due to the rate at which the number of atoms increases with radius, whereas if dealing with the energy per unit tube length, the energy increases as a function of inverse radius [49, 87].

Nanotubes are not unique carbon structures in having the geometric property of curvature, fullerenes and folds in graphene also exhibit this property. Folded graphene sheets have been produced by lightly irradiating the edge of multi layered graphene flakes [82]. A similar method for calculating the energy of a deformed membrane using the curvature and thickness as the dependent variables is presented. When bending a beam or sheet, opposing forces are introduced either side of the centre of the thickness. The surface on the inside of the bend is under compressive stress, whilst the outside is under tensile stress, as illustrated in figure 6.1. These two forces contribute to returning the bar to its equilibrium state.

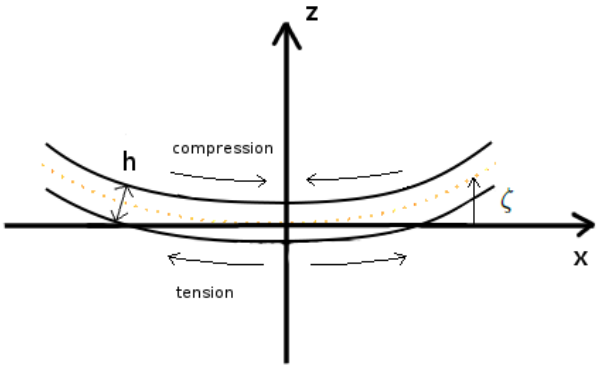

Figure 6.1: Image showing an element of membrane of thickness h about one axis. For small displacements, the local second derivative along x is equal to the curvature. The dotted line represents the middle of the sheet.

Yang and Tewary have investigated the bending properties of graphene in the

continuum limit [90]. The method uses a Kirchoff plate model to explain the stability of two dimensional graphene and the convergence of an atomistic model with a continmuum model, providing grounds for the use of continuum theory applied to graphene. However, they predict the flexural rigidity D, an intrinsic property of a graphene membrane, to be 0.797 eV. This is in disagreement by almost a factor of two with other values measured in the literature [91]. The value for the bending modulus used herein is the same as that calculated independently by both Huang and Tománek, which is 1.4 eV. This is shown to be in good agreement when used in the continuum elasticity calculations for the bending energy when compared to high level DFT simulations on the formation energy of carbon nanotubes (see figure 6.2). Of course, this value for the bending modulus could be adjusted in the elasticity calculations presented here to better fit the DFT calculations, but is kept as 1.4 eV to remain in line with literature findings.

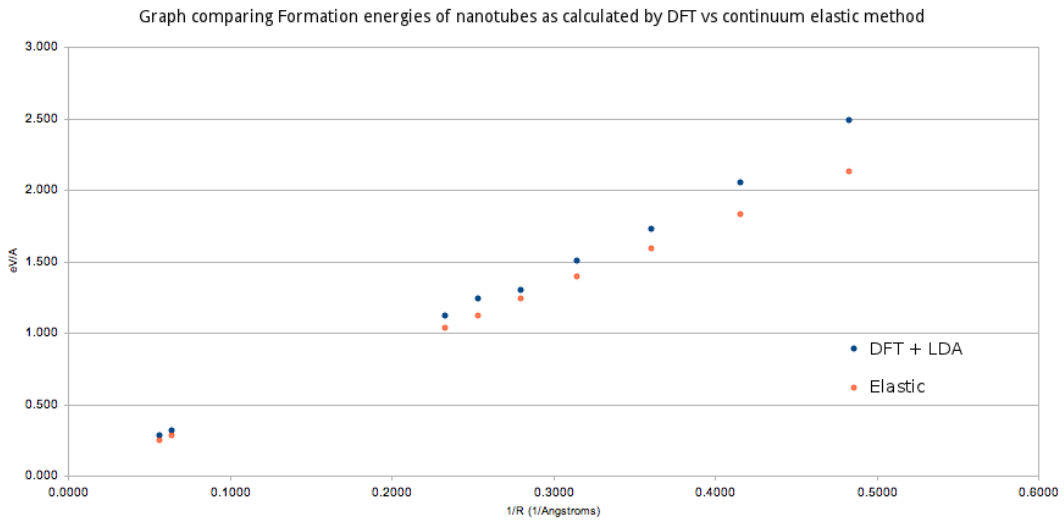

Figure 6.2: Nanotube energy per unit tube length calculated using elasticity theory with flexural rigidity value of 1.4 eV, compared with DFT results for the formation energy of nanotubes [92].

Experimental evidence of folds occurring at the edges of both natural and synthetic graphitic materials have been directly imaged by Rotkin and Gogotsi [93]. Reconstructed edges that form folds involving one and two layers are clearly

shown in TEM images (shown in figure 6.3). MD simulations of such structures also predict that the arched edges have a curvature similar to that of nanotubes [93]. Gogotsi *et al.* have also performed Raman spectroscopy on these samples and find nanotube-like vibrational modes arising from the curved edges, providing further evidence for pristine folded graphite [94].

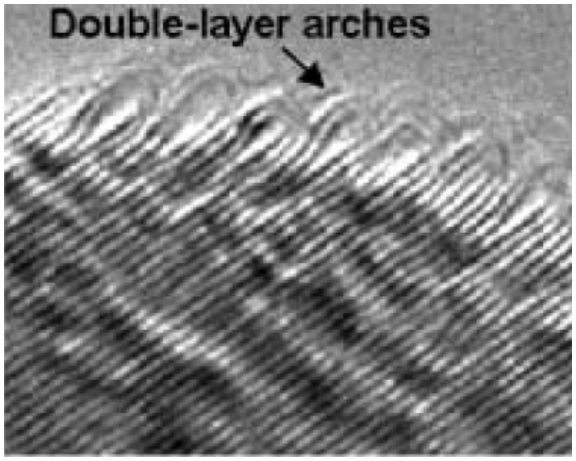

Figure 6.3: Gogotsi has imaged arched edges or folds involving double layers formed at the egdes of graphite polyhedral crystals. Image reproduced from [94].

Landau and Lifshitz provide the general equation for calculating the free energy due to bending for small deformations of a thin elastic membrane [95]. The equation depends on the vertical displacement of the sheet, ζ, at each point in a plane. An approximation is made here, justified by the use of thin membranes that ignores the resultant Gaussian curvature that is induced when a plane of non-neglible thickness is bent [96]. The resultant surface is known as anticlastic, and takes the form of a saddle shape which has curvature of opposite directions in planes normal to one another at a single point.

$$E_{bend} = \frac{Yh^3}{24(1-\sigma^2)} \iint \left[\left(\frac{\partial^2 \zeta}{\partial x^2} + \frac{\partial^2 \zeta}{\partial y^2} \right)^2 + 2(1-\sigma) \left\{ \left(\frac{\partial^2 \zeta}{\partial x \partial y} \right)^2 - \frac{\partial^2 \zeta}{\partial x^2} \frac{\partial^2 \zeta}{\partial y^2} \right\} \right] \mathrm{d}x\mathrm{d}y \tag{6.1}$$

Here, Y is Young's modulus, h is the thickness of the membrane and σ is the

Poisson ratio. It is convenient to abbreviate this combination of variables into one referred to as the bending modulus, D of the membrane. In the small displacement approximation, the second derivative of the displacement with respect to a direction is equal to the local curvature, C. If bending is considered about only one axis, terms containing derivatives with respect to that axis disappear, since no curvature is induced along that direction. This leads to the simplification shown in equation (6.2)

$$E_{bend} = \frac{Yh^3}{24(1-\sigma^2)} \iint \frac{\partial^2 \zeta}{\partial x^2} \; dxdy \tag{6.2}$$

This equation holds for small displacements, however for structures such as tightly rolled nanotubes, ruck and tuck defects and buckles, the displacement can be large, with a local radius of curvature reaching 0.3 nm. In such cases, rather than use the second derivative as the parameter along the arclength, it is subsituted for the local radius of curvature for all cases. The integral over the second dimension has no dependence on the curvature, hence it is equivalent to integrating over the depth of the structure. Alternatively, it can be transferred to the other side of the equation and the integral then represents the energy per unit depth of curved defect. This depth for example would be the length of nanotube or fold involved. The equation may be reduced to that shown in equation (6.3), with C representing the local curvature as a function of the arclength. The local radius of curvature for a real valued function is given by equation (6.4) and that for a parametrically defined curve of the form $S = (x(t), y(t))$ is shown in (6.5).

$$E_{bend} = D \int_l C(l) \; dl \tag{6.3}$$

$$C_{func} = \frac{f''(x)}{(1 + f'(x)^2)^{3/2}} \tag{6.4}$$

$$C_{param} = \frac{x'y'' - y'x''}{x'^2 + y'^2} \tag{6.5}$$

6.1 Generalised 2D bending energy

A Matlab code has been written to calculate the energy due to pure bending given a general parametric description of a curve (The Matlab algorithm is provided in Appendix A.1). The curve is required to be defined as a pair of parametric functions $x(t)$ and $y(t)$, where t is the dependent variable. The curve must be continuous and twice differentiable everywhere. Rapdily varying curves which either have high curvature or discontinuities will generate poor mappings. In general, equidistant intervals in the parameter t do not translate to equally separated points along the arclength of a curve defined parametrically. This may lead to biased sampling of a property along the curve such as the curvature, and may result in a poor estimate of the energy due to bending.

In order to generate equidistant sampling points of the curvature along the arclength, it is necessary to integrate over the curve and store the arclength as a function of t. This is performed using the 'quadgk' routine in Matlab. The function 'quadgk' computes an approximate value for the integral of a function between specified points. These lengths are used to find the values for t which relate to equal intervals along the arc. The arclength of a parametric equation is given by equation (6.6). The curvature at each of the points is squared and summed, as is necessary to find the total energy due to bending. For the case of a tube, it is unnecessary to use any numerical integration as the curvature is constant everywhere. The Matlab code takes this into account and includes a special case for the circle and simply returns the value of the energy per unit tube length according to equation (6.3) but with the curvature, C as a constant.

$$L = \int_a^b \sqrt{\left(\frac{dx}{dt}\right)^2 + \left(\frac{dy}{dt}\right)^2}\ \mathrm{d}t \tag{6.6}$$

Several parametric curves were generated, each representing a bending configuration of a sheet over suitable length scales and viable minimum curvatures. The four different curves, for which the equations are provided in table 6.1, represent cylindrical tubes, folds, buckles and a wave packet like distortion which shall be referred to as a chirp. The properties for each of the curves using the continuum elasticity method are shown in table 6.2, while corresponding images of each configuration are provided in figure 6.4.

Parametric equations		
	$x(t)$	$y(t)$
a) and b)	$R\cos(t)$	$R\sin(t)$
c)	$Wt\cos(t)$	$A\tan(t)\cos(3t)$
d)	t	$A\cos(\pi t/W)$
e)	t	$Ae^{-\lambda t^2}\cos(\omega t)$

Table 6.1: Table showing equations representing various configurations of deformed membrane.

Where R is the radius of the circle, W is a scaling parameter for the width along the x axis, A is the scaling for the maximum amplitude, λ governs the rate of amplitude decay and ω is the frequency of oscillation in the wave packet description.

	Structure	Energy (eV/Å)	Smallest radius (Å)	Arc length (Å)
a)	nanotube (6 Å diam)	1.0	6.0	37.0
b)	nanotube (3 Å diam)	1.46	3.0	19.0
c)	ruck and tuck	5.2	1.0	57.0
d)	buckle (1.5 Å amp)	0.15	10.0	27.3
e)	chirp (2 Å max amp)	4.3	1.0	41.0

Table 6.2: Table of bending energies and curve properties

The highest energy structure is shown to be the ruck and tuck defect, comprised of two tightly folded regions. The chirp is the next highest in energy, where there exist highly curved regions, but these are quickly reduced with increasing distance from maximum amplitude. The 2.5 nm wavelength buckle is a relatively low energy structure in terms of bending with only lightly curved regions relative to the other configurations.

The elastic energy required to deform a graphene sheet into a nanotube increases with inverse radius, ignoring corrections for high curvature. Figure 6.2 shows a plot of nanotube formation energy vs inverse radius from DFT calculations compared with the bending energy of equivalent radii tubes using the continuum elastic method. Although the calculations here are for pure bending energy, it should be noted that as curves approach themselves along their arc length, an interlayer interaction would be present which would have the effect of reducing the total energy [97]. This contribution has not been accounted for here, but it is expected to reduce the energy for the ruck and tuck defect in particular. This is a possible improvement that could be made to the model, either by using a continuum approach with a binding energy per unit area and neglecting relative atomic positions, or by taking into account the registry across the three layered region of the fold.

The motivation for calculating these bending energies for various forms of graphene is for their possible use as the core energy of a dislocation configuration. Structures such as those proposed here using the equations in table 6.1 have well defined structures for which the atomic displacements are large, but the hexagonal layered structure is maintained, so bonds are preserved and bond distortions are not unrealistic.

6.2 Atomic coordinate mapping

In order to create extended defects in graphite such as buckles and folds for the purpose of atomistic modelling of such structures, it has been useful to be able to map the coordinates of graphene onto various surfaces. The extended defects implemented here only vary along two dimensions, in order to be able to create periodic boundary conditions. Routines have been written in Fortran for the purpose of mapping a set of coordinates in a plane onto the surface of a two dimensional function or parametric equation (with the third dimension an extension of the 2D form to create a line defect). This was for the purpose of generating approximate structures of interest for use in modelling software such as GULP, to model and optimise different configurations. The routines require the function and its path integral to be specified. The path integral for a function is shown in equation (6.7) and that for a parametrically defined curve in equation (6.6). The mapping of a flat sheet of graphene onto a surface that varies in two Cartesian coordinates is simplified from that of a function which varies in all three axes. Firstly, the path length integral for the prescribed function or parametrically defined equation is numerically evaluated over small iterations (small enough such that the nearest neighbour atoms may be mapped without causing undesirable discrepancy in interatomic distance). Each of the iterations is stored, alongside the associated integration limit on the variable. The mapping routine then compares the x value of each atom coordinate to that of the arclength along the curve. For each of the atoms' x coordinates, the closest result for the arclength is associated with that atom. From this data, each atom may be assigned a new x and y coordinate corresponding to the function value at that arclength. Each atom's z coordinate remains unchanged due to no variation in the surface height along that axis.

$$L = \int_a^b \sqrt{1 + \left(\frac{dy(x)}{dx}\right)^2}\, \mathrm{d}x \tag{6.7}$$

Care should be taken when using the routine to make sure dimensions of the curve are viable. The curve should not approach itself too closely, within viable range of the equilibrium interlayer distance [2], and the smallest radius of curvature should be greater than 0.2 nm.

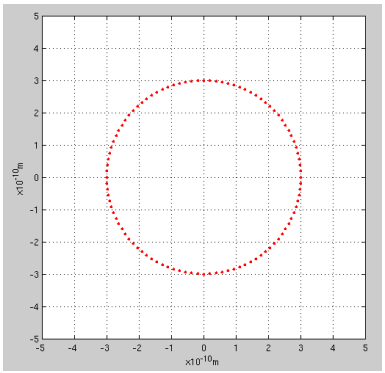

(a) 1 & 2 - Nanotube of radius 0.3 nm

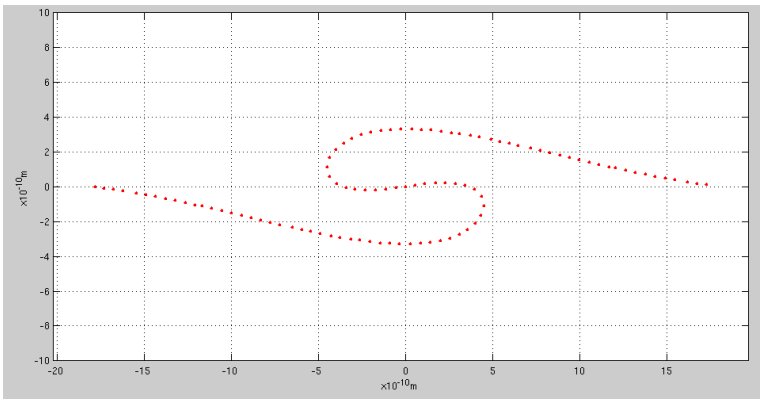

(b) 3 - Ruck and Tuck defect represented by a parametric equation

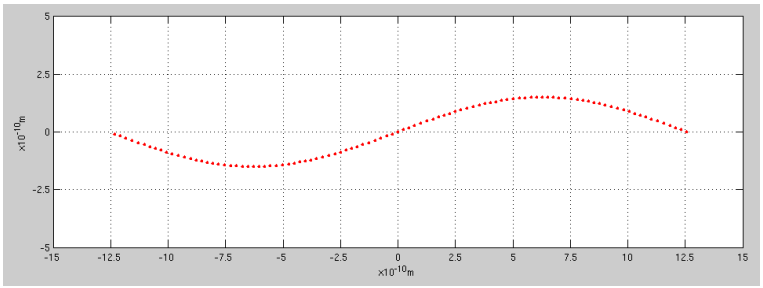

(c) 4 - Buckle of wavelength 2.5 nm and 0.15 nm amplitude

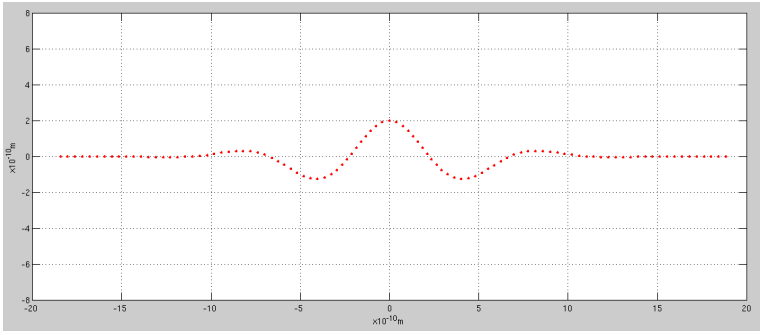

(d) 5 - Chirp represented by decaying oscillating function. Maximum amplitude of 0.2 nm and a decay constant of 0.025

Figure 6.4: Images of curves representing configurations of graphene layers. The numbers in the images correspond to entries in table 6.2. Each curve has been defined by the equations shown in table 6.1.

6.3 Folds in hexagonal boron nitride

Hexagonal boron nitride, abbreviated hBN, is a layered material which has a structural configuration very much like AA stacked graphite. Each atom in the hexagonal planes have three nearest neighbours of the opposite species. The boron and nitrogen atoms also alternate in the layer plane stacking direction, such that along the **c** direction, the sequence of atoms is BNBN. The lattice parameters of hexagonal boron nitride are **a**=0.243 nm and **c**=0.666 nm [98]. The hexagonal form of boron nitride is of particular interest because it is a layered material, very similar in structure to graphite and may exhibit some characterstic behaviours which are similar in nature to graphite.

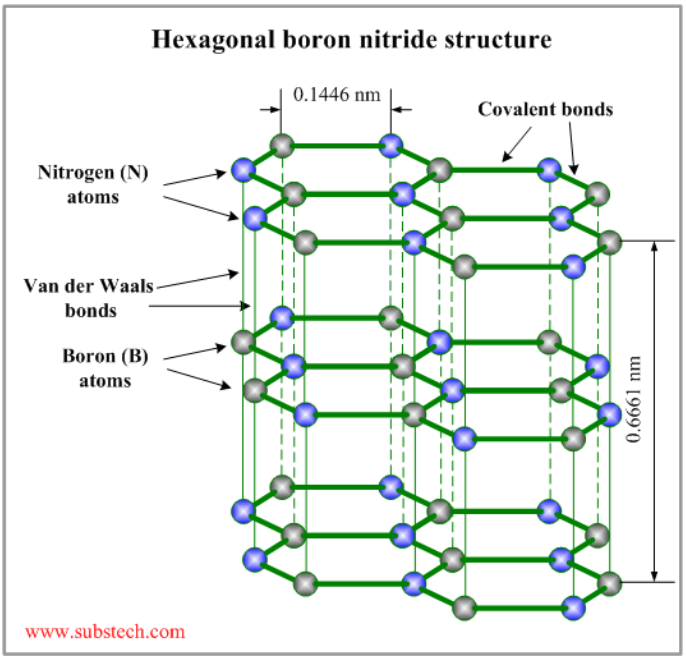

Figure 6.5: The structure of hexagonal boron nitride. Image reproduced from [99].

Zobelli *et al.* have been studying this material, and have employed microscopy techniques to view the surface of hexagonal boron nitride samples. They have produced images which contain what they believe to be folds existing at the surface [100]. Evidence in the images leading to the interpretation of folds has presented itself as two pairs of parallel lines separated in depth by about 1 nm. These folds involve more than one layer of the material, and as such resemble

the effects in images akin to that for nested nanotubes, or multi-walled nanotubes (MWNT). In a collaborative effort with Zobelli, a folded structure involving two layers of boron nitride situated atop four planar layers has been created. The model is for the purpose of simulated imaging, to compare directly with the collected experimental image to confirm or denounce the interpretation of the parallel lines in the experimental result as a two layered fold. The fold mapping routine has been used to generate the necessary double fold structure, with the aid of Avogadro molecular modelling software to produce folds on the surface of boron nitride for imaging purposes. The process involved creating two folds of different scales and concatenating half of each with one another, this allowed the nesting of the layers within one another to create the two layered fold. The structure was manipulated within Avogadro and subsequently opimised using GULP to produce a suitable periodic supercell.

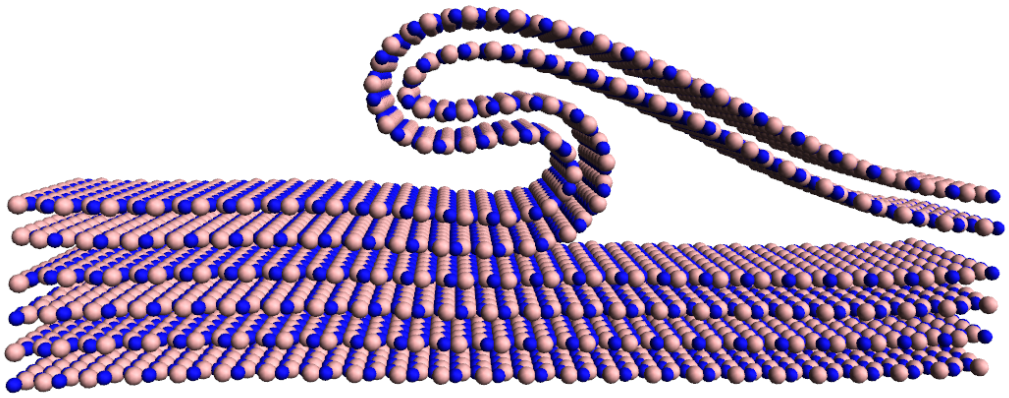

Figure 6.6: A fold involving two layers of hexagonal boron nitride. The structure has been optimised using a molecular mechanics potential within the GULP package. The width of the fold (distance between fold extremes) is ∼2.5 nm, and its height ∼2.3 nm.

This is ongoing collaborative work and we expect to have some results from simulated microscopy images generated using the structure shown in figure 6.6 in the near future.

Chapter 7

Conclusions

The properties of graphite and some of its unusual properties as a layered material have been discussed. The idea that dislocations and other extended defects may contribute substantially to the observed dimensional change has been studied with the use of dislocation theory and X-ray diffraction simulations.

X-ray diffraction simulations have shown that the ruck and tuck defect poses the best model when compared with experimental data. The simulations on the fold reproduced most accurately the observed changes to the pattern with substantial broadening of the d_{002} spots and diffuse streaks connecting spots lying along the $(10l)$ lines.

The use of GULP software to optimise structures containing dislocations has provided substantial evidence for the formation of cracks by delamination as a result of out-of-plane stress relief. The confinement of a pile up of partial basal dislocations has been shown to be sufficient to cause delamination within the cell when confined to regions smaller than their full core width. Interstitials bound across the slip plane have been shown as insufficient to prevent glide of the whole dislocation, but instead prevents the slip of material in layers adajcent to the slip plane, which allows the rest of the dislocation to free itself by the process of climb.

The optimisation of a structure containing a folded layer proved to be stable, although there are subtle differences in the curvature at the extremeties of the fold when compared with structures optimised using the Cerius2 software. Folds optimised using GULP allowed more acute curvature. The interlayer potential implemented in GULP may not be sufficient to model defects that have stacking intricacies, where a registry dependent potential should be used instead of, or in addition to, a simple Lennard Jones interlayer potential.

Dislocation theory has been successfully implemented as a tool for creating displacement fields which accommodate other extended defects such as folds and prismatic loops. Careful choice of the placements of the dislocations can yield representative displacements in order to accommodate the defects for the creation of models. In conjunction with the routines to map graphene on to functions and parametric forms, this has proven to be a very convenient method for creating very large structures with extended defects without the need to use molecular modelling software to manually place or adjust the positions of atoms and the bonds between them.

The elastic energy due to bending has shown good agreement with high level calculations on nanotubes, and is justified for use with other layer configurations with moderate curvature and could be a simple method of calculating the dislocation core energy for such defects. The mapping algortithm is a verstaile tool in allowing the generation of structures defined by functions or parameteric equations that enable the creation of a broad range of layer deformations.

Further work should include *ab initio* calculations on extended defect structures to more precisely model the structures and energies thereof. Vibrational and electronic properties of the extended defects, particularly for that of the ruck and tuck and basal dislocations could also be of interest. The current limitation is that extended defects in graphite have far reaching displacement fields and most of the defects require cells containing a few thousand atoms to reduce periodic

interactions. With continued advances in computational methods and computing resources, these calculations should be possible in the very near future.

Appendix A

Source codes

A.1 Matlab code for bending energy

```
function [eV_per_Angstrom, max_curv, arclength]=bending()
    % call the function using "[eV_per_Angstrom, arclength]=bending()"
    % Function takes no arguments.

   fprintf('\n (Note: governing functions are contained in file "bending.m") \n');

    choice=...
    input('\n Select structure by number: \n\n 1-fold \n 2-buckle...
                                \n 3-chirp \n 4-circle \n\n:');

    % number of sampling points along arclength of curve
    points=100;

    %-------------------------Predefine functions-------------------------
   % a and b are coefficients in the parametric equation. The switch statement
   % allows one from a selection to be chosen at runtime. More cases may be added
    switch choice
```

```
case{1}
    % fold
    a=8.0;
    b=1.1;

    lo_lim=-2.6;
    hi_lim=2.6;

    syms t

    x=a*t*cos(t);
    y=b*tan(t)*cos(3*t);

  % function handle L (denoted by '@' symbol) passed to quad routine.
    L=@(t)((a*cos(t)-a*t.*sin(t)).^2+(b*(1+tan(t).^2).*...
              cos(3*t)-3*b*tan(t).*sin(3*t)).^2).^(1/2);

case{2}
    % buckle
    a=1.5;
    b=0.25;

    lo_lim=-pi/b;
    hi_lim=pi/b;

    syms t
    x=t;
    y=a*sin(b*t);

    L=@(t)((1+a*b*cos(a*t).^2).^(1/2));
```

```
case{3}
    % chirp or wave packet
    syms t

    a=2.0;
    b=0.025;
    c=0.7;

    x=t;
    y=a*exp(-b*t^2)*cos(c*t);

    lo_lim=-6*pi;
    hi_lim=6*pi;

L=@(t)(1+(a*exp(b*t.^2).*(2*b*t.*cos(c*t)-c*sin(c*t))).^2).^(1/2);

 case{4}
   % special case for circle, energy easily calculated from Radius.
    R=input('Specify tube radius (Angstroms):');
    syms t

    T=-pi:2*pi/points:pi;

    x=R*cos(t);
    y=R*sin(t);

    Xt=zeros(1,points);
    Yt=zeros(1,points);

    for i=1:points
         Xt(i)=subs(x,T(i));
```

```
            Yt(i)=subs(y,T(i));
        end

        plot(Xt,Yt,'.r','markersize',6);

        axis equal
        xlim([-10 10])
        ylim([-10 10])

        max_curv=1/R;
        arclength=2*pi*R;
        eV_per_Angstrom = pi*1.4/R;
        return;

    otherwise
        fprintf(2,'\n invalid selection!\n\n\n');
        return;
end

% 1st and 2nd derivatives required
dx=diff(x,t);
ddx=diff(dx,t);

dy=diff(y,t);
ddy=diff(dy,t);

curvature=abs(dx*ddy-dy*ddx)/((dx^2+dy^2)^1.5);

%-------------integration routine---------------

tr=(lo_lim:0.005:hi_lim);
```

```
M=zeros(1,numel(tr));

    for i = 2:numel(tr)
    % Gauss-Kronrod adaptive quadrature - integral is evaluated
    % repeatedly from lo_lim to i, each is stored in M(1,i)
      M(1,i) = quadgk(L,lo_lim,tr(i));
    end

%-----------locate equal intervals---------------

uplen=max(M);
ind=zeros(1,points);
T=zeros(1,points);

% 'sep' increases by an equal amount each iteration.
% 'sep' is then compared to each entry in 'M' to find the closest
% arclength match. The corresponding value for t can then be found for
% consecutive equal interval points.
     for i=1:points
          sep=(uplen/points)*i;
          temp=abs(M-sep);
          [l,ind(i)]=min(temp);
          T(1,i)=tr(ind(i));
     end

Xt=zeros(1,points);
Yt=zeros(1,points);
% substitute the previously found values for t into the original
% equations to plot points at equidistant arclengths ('sanity check')
    for i=1:points
```

```
            Xt(i)=subs(x,T(i));
            Yt(i)=subs(y,T(i));
        end

    plot(Xt,Yt,'.r','markersize',6);

    axis equal
    xlim([-25 25])
    ylim([-10 10])

    %----------------------Curvature_sum----------------------

    % calculate the energy due to bending. Bending modulus
    % of graphene from literature (Tomanek, Huang), 1.4eV

    total=0;
    curv=zeros(1,points);
    for i=1:points
        curv(1,i)=subs(curvature,T(1,i));
        total=total+curv(1,i)^2;
    end

    max_curv=1/max(curv);
    arclength=max(M);
    eV_per_Angstrom = 1.4*total*max(M)/points;


end
```

A.2 FORTRAN code for turbostratic graphite

```
program rotate

 use universal
 implicit none

 integer :: i, j, l, a1, a2, lat, diff, cnt, tmp=0
 real, dimension(atnum) :: jar
 real, dimension(3,atnum) :: r
 real, dimension(3) :: minrot, maxrot, minr, maxr, adjust
 real :: theta, xlim, ylim, temp, xrpt, yrpt, xunits
 real :: x, y, veclen, ch, rptfac

 open(1,file='80,80,0-AB.xyz',status='old')

 write(*,*) 'Provide indices of desired direction (a,b):'
 read(*,*) a1, a2

 write(filename,'(a,i2.2,a,i2.2,a)')'rotated',a1,',',a2,'.xyz'

 open(2,file=filename)

 theta=atan((sqrt(3.)/2.)*a2/(a1+0.5*a2))

 ch = 2.446*sqrt((a2*cos(pi/6.))**2 + (a1+a2*sin(pi/6.))**2)
 diff=a1-a2

 if(a2.gt.a1) then
 write(*,*) 'rotation angle greater than 30 degrees!'
 return
```

```
 endif

 if(a2.eq.0) then
 theta=0.
 endif

 xrpt=ch
 cnt=0

 do j=1,atnum
  read(1,*,end=110) c, r(2,j), r(1,j), r(3,j)
  r(1,j)=r(1,j)-80.48911478133
  r(2,j)=r(2,j)-56.25818538906
  cnt=cnt+1
 enddo

110 continue

 allocate(rot(3,cnt))

 write(*,*) '-------------------------------------------------------'
 write(*,*) 'relative rotation angle =', 2.*theta*180./pi, 'degrees'
 write(*,*) 'lattice paramter for hex-p=', xrpt*1.8897, 'atomic units'
 write(*,*) '-------------------------------------------------------'

 latparam=xrpt*1.8897
 write(*,*) 'lattice parameters (a,c) =', xrpt, 6.482
 ! -----------------------------------------------------

 do j=1,cnt
  rot(3,j)=r(3,j)
```

```
 if(r(3,j).eq.0.) then
  rot(1,j)=r(1,j)*cos(theta)-r(2,j)*sin(theta)
  rot(2,j)=r(1,j)*sin(theta)+r(2,j)*cos(theta)
 else
  rot(1,j)=r(1,j)*cos(theta)+r(2,j)*sin(theta)
  rot(2,j)=r(1,j)*(-1.)*sin(theta)+r(2,j)*cos(theta)
 endif
 rptfac=(rot(2,j))*tan(pi/6.)
 if(rot(1,j).gt.(-1.)*rptfac.and.rot(2,j).ge.0.) then
  if(rot(1,j).lt.xrpt-rptfac.and.rot(2,j).le.xrpt*cos(pi/6.)) then
   tmp=tmp+1
   unitcell(1,tmp)=rot(1,j)
   unitcell(2,tmp)=rot(2,j)
   unitcell(3,tmp)=rot(3,j)
  write(2,'(a," ",f8.4," ",f8.4," ",f8.4)') c, rot(1,j), rot(2,j), rot(3,j)
  endif
 endif
enddo

close(2)

call datfile(tmp)

end program rotate
```

Appendix B

Figures

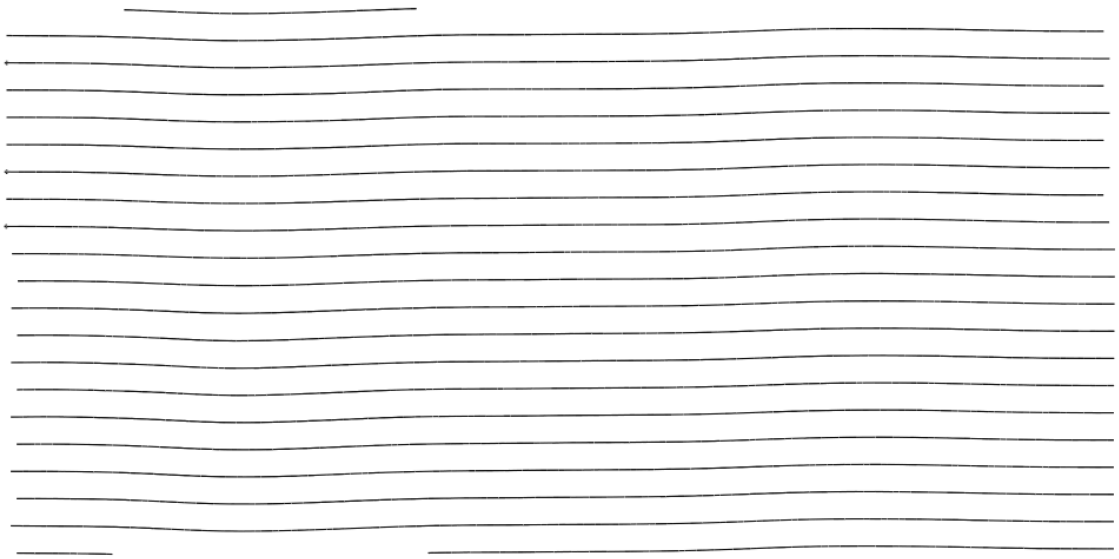

Figure B.1: A dipole of 90° partial basal dislocations, constrained to half the cell width each and the cell structurally optimised.

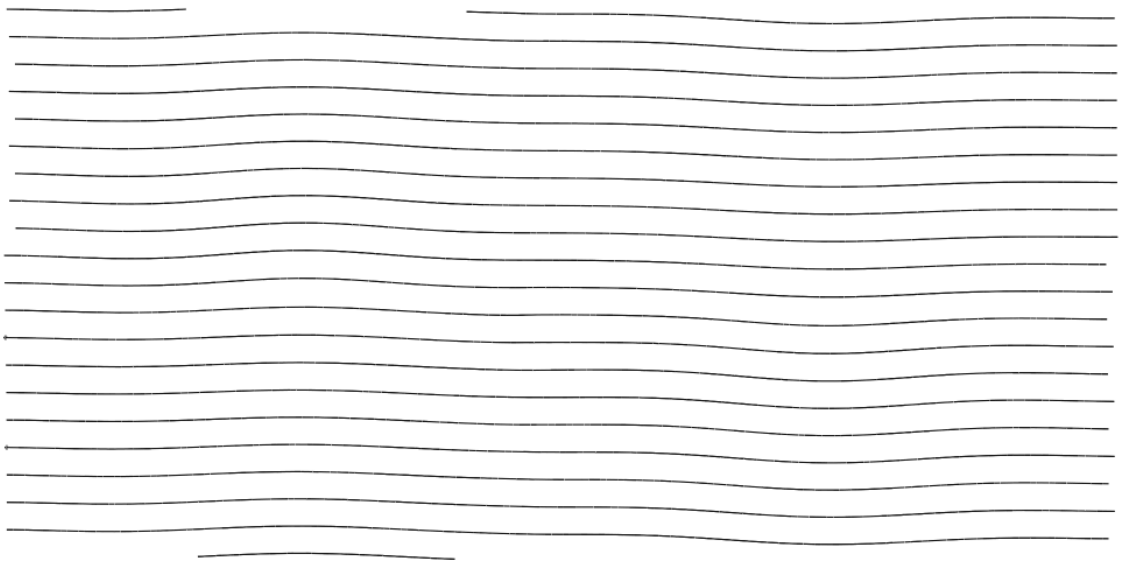

Figure B.2: A dipole of two 90° partial basal dislocations, constrained to half the cell width each and the structurally optimised.

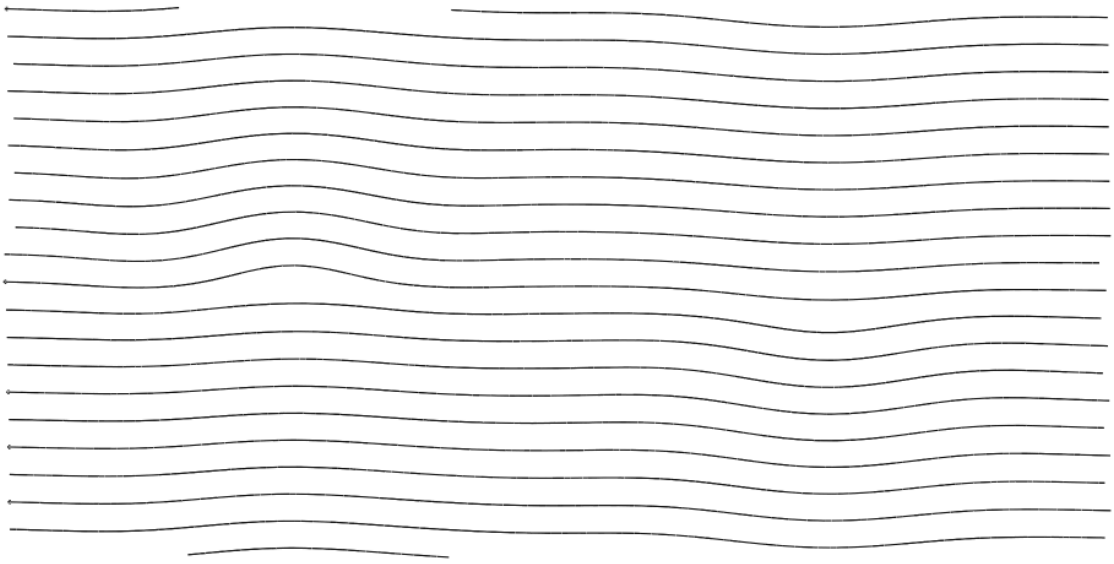

Figure B.3: A dipole of three 90° partial basal dislocations, constrained to half the cell width each and the cell structurally optimised.

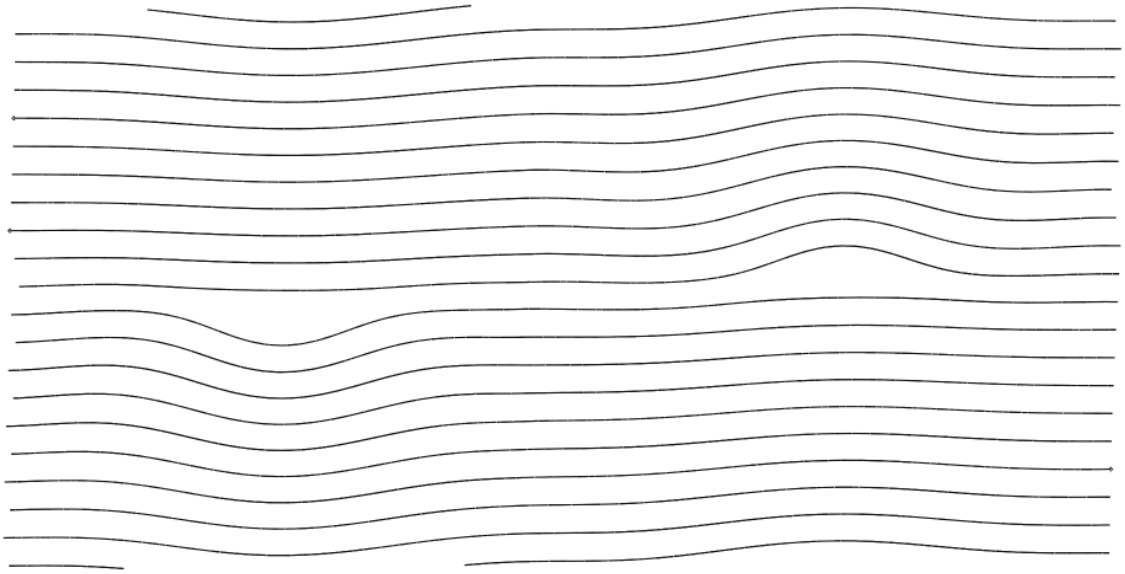

Figure B.4: A dipole of four 90° partial basal dislocations, constrained to half the cell width each and the cell structurally optimised.

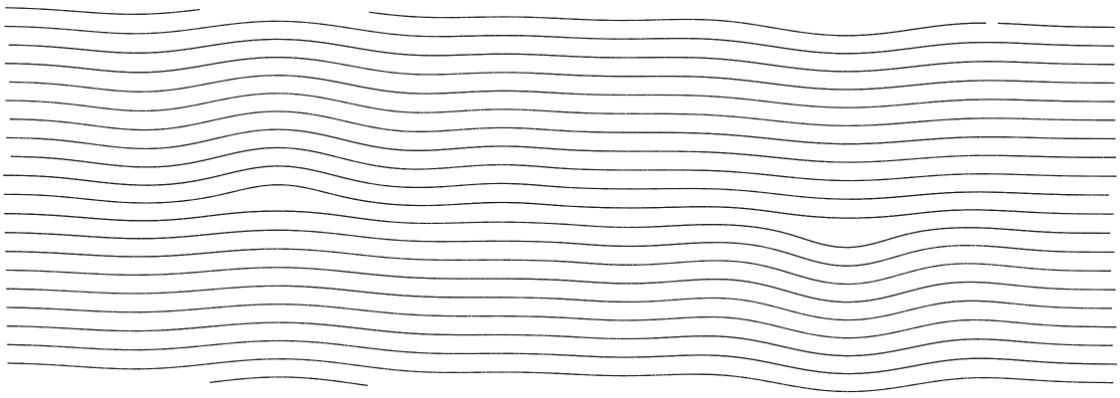

Figure B.5: A dipole of four 90° partial basal dislocations, constrained to half the cell width in a cell 50% larger in width than B.4 and structurally optimised.

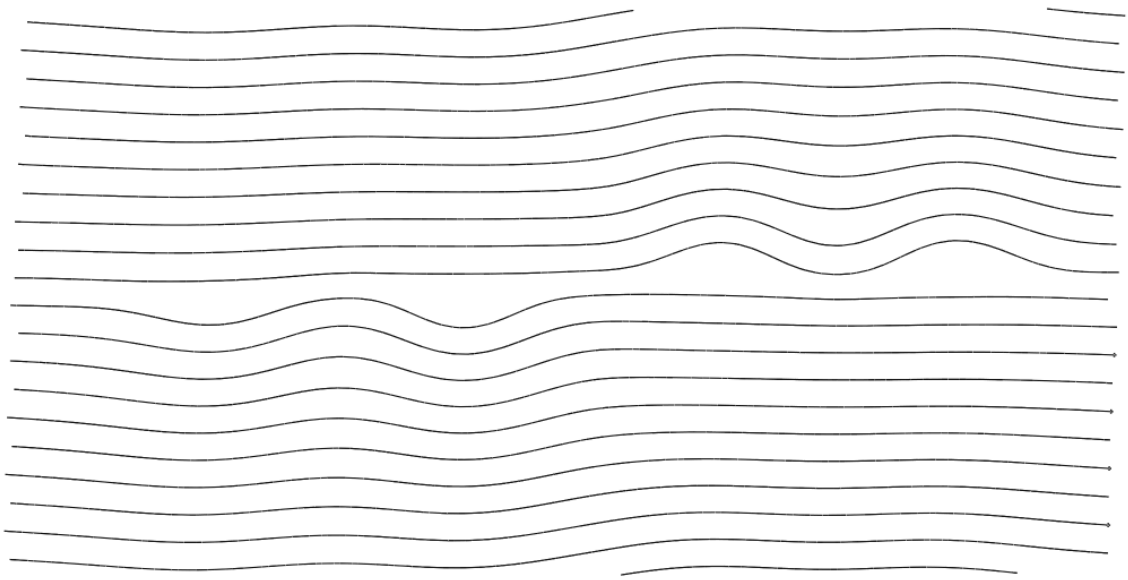

Figure B.6: A dipole of seven 90° partial basal dislocations, constrained to half the cell width each and optimised. The limit of seven was reached as further dislocations caused undesirable core distortions, even with the discretising of the Burgers vector.

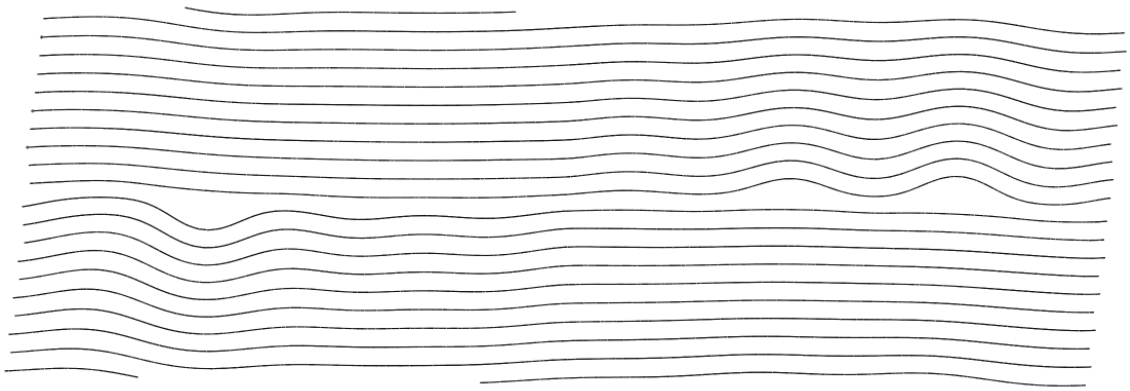

Figure B.7: A dipole of seven 90° partial basal dislocations, constrained to half the cell width each in a cell 50% wider than B.6 and structurally optimised.

List of Figures

List of Tables

Bibliography

[1] A. W. Hull. A new method of x-ray crystal analysis. *Phys. Rev.*, 10(6):661–696, December 1917.

[2] J. D. Bernal. The structure of graphite. *Proc. R. Soc. London, Ser. A*, 106(740):749–773, December 1924.

[3] J.-C. Charlier, X. Gonze, and J.-P. Michenaud. Graphite interplanar bonding: electronic delocalization and van der Waals interaction. *Europhys. Lett.*, 28(6):403–408, November 1994.

[4] J.-M. Campanera, G. Savini, I. Suarez-Martinez, and M. I. Heggie. Density functional calculations on the intricacies of moiré patterns on graphite. *Phys. Rev. B*, 75(23):235449, June 2007.

[5] C. S. G. Cousins and M. I. Heggie. Elasticity of carbon allotropes. III. Hexagonal graphite: Review of data, previous calculations, and a fit to a modified anharmonic Keating model. *Phys. Rev. B*, 67(2):024109, January 2003.

[6] G. Savini and M. I. Heggie. Mesoscale elastic constants in graphite. In *Carbon 2007 Proceedings*, Seattle, Washington, July 2007.

[7] R A Dugdale. The colouring of diamonds by neutron and electron bombardment. *British Journal of Applied Physics*, 4(11):334, 1953.

[8] L. C. Qin. CVD synthesis of carbon nanotubes. *J. Mater. Sci. Lett.*, 2:4 – 6, 1997.

[9] E. G. Gamaly and T. W. Ebbesen. Mechanism of carbon nanotube formation in the arc discharge. *Phys. Rev. B*, 52(3), 1995.

[10] R. Saito, G. Dresselhaus, and M.S. Dresselhaus. *Physical properties of carbon nanotubes*. Imperial College Press, Covent garden, London, 1998.

[11] Z Wang, P Ciselli, and T Peijs. The extraordinary reinforcing efficiency of single-walled carbon nanotubes in oriented poly(vinyl alcohol) tapes. *Nanotechnology*, 18(45):455709, 2007.

[12] B.T. Kelly, B.J. Marsden, K. Hall, D.G. Martin, A. Harper, and A. Blanchard. Irradiation damage in graphite due to fast neutrons in fission and fusion systems. *IAEA-TECDOC*, 2000.

[13] P. A. Thrower. The study of defects in graphite by transmission electron microscopy. In P. L. Walker, editor, *Chemistry and Physics of Carbon*, volume 5, chapter 3, pages 217–319. Marcel Dekker, New York, 1969.

[14] D. R. Ball. High purity nuclear graphite, August 2007. Application for United States letters patent.

[15] B. T. Kelly. *Physics of graphite*. Applied Science Publishers, Barking and New Jersey, 1981.

[16] T. Iwata, F. E. Fujita, and H. Suzuki. On the energy of the interstitial atom in graphite. *J. Phys. Soc. Jpn.*, 16(2):197–205, February 1961.

[17] Timothy D. Burchell and Lance L. Snead. The effect of neutron irradiation damage on the properties of grade nbg-10 graphite. *Journal of Nuclear Materials*, 371(13):18 – 27, 2007.

[18] C. A. Coulson, S. Senent, M. A. Herraez, M. Leal, and E. Santos. Deformation of graphite lattices by interstitial carbon atoms. *Carbon*, 3(4):445–457, February 1966.

[19] L. Li, S. Reich, and J. Robertson. Defect energies of graphite: Density-functional calculations. *Phys. Rev. B*, 72:184109, Nov 2005.

[20] Andris Gulans, Arkady V. Krasheninnikov, Martti J. Puska, and Risto M. Nieminen. Bound and free self-interstitial defects in graphite and bilayer graphene: A computational study. *Phys. Rev. B*, 84:024114, Jul 2011.

[21] M. I. Heggie, I. Suarez-Martinez, C. Davidson, and G. Haffenden. Buckle, ruck and tuck: A proposed new model for the response of graphite to neutron irradiation. *J. Nucl. Mater.*, 413(3):150–155, June 2011.

[22] P. Kim. Hierarchical folding of elastic membranes under biaxial compressive stress. *Nature Materials*, 10(10):1 – 3, 2011.

[23] D. Vella, A. Boudaoud, and M. Adda-Bedia. Statics and Inertial Dynamics of a Ruck in a Rug. *arXiv:0905.2952v2*, 3(87), 2009.

[24] P. J. Hudleston. Similar folds, recumbent folds, and gravity tectonics in ice and rocks. *The Journal of Geology*, 85(1):113 – 122, 1977.

[25] Talbot. http://myweb.facstaff.wwu.edu/talbot/cdgeol/structure/fold/folds1/recumbent.l

[26] M. J. Rayson and P. R. Briddon. Highly efficient method for Kohn-Sham density functional calculations of 500–10 000 atom systems. *Phys. Rev. B*, 80(20):205104, November 2009.

[27] Julian D. Gale and Andrew L. Rohl. The general utility lattice program (gulp). *Molecular Simulation*, 29(5):291–341, 2003.

[28] R. H. Telling and M. I. Heggie. Stacking fault and dislocation glide on the basal plane of graphite. *Phil. Mag. Lett.*, 83(906873699):411 – 421, 2003.

[29] Yoshitaka Matsukawa and Grace S. Liu. In situ tem study on elastic interaction between a prismatic loop and a gliding dislocation. *Journal of Nuclear Materials*, 425(13):54 – 59, 2012.

[30] S. Mrozowski. Mechanical strength, thermal expansion and structureof cokes and carbons. *At. Energ.*, 15, 1951.

[31] C. R. Davidson. X-ray diffraction simulations of defects in graphite, 2009. unpublished.

[32] G. I. Taylor. The mechanism of plastic deformation of crystals. part i. theoretical. *Proceedings of the Royal Society of London. Series A*, 145(855):362–387, 1934.

[33] E. Orowan. For crystal plasticity. *Zeitschrift Fur Physik*, 89(9-10):605–613, SEP 1934.

[34] D. Hull & D.J. Bacon. *Introduction to Dislocations*. Butterworth-Heinemann, Oxford, fourth edition, 2001.

[35] B. Yang, M.W. Barsoum, and R.M. Rethinam. Nanoscale continuum calculation of basal dislocation core structures in graphite. *Philosophical Magazine*, 91(10):1441–1463, 2011.

[36] K. Niwase. Formation of dislocation dipoles in irradiated graphite. *Mater. Sci. Eng. A*, 400–401:101–104, July 2005.

[37] P. J. Ouseph. Observation of prismatic dislocation loops in graphite by scanning tunneling microscope. *Phys. Status Solidi A*, 169(1):25–32, September 1998.

[38] M. I. Heggie. Private communication.

[39] J. Koike and D. F. Pedraza. Dimensional changes in highly oriented pyrolytic graphite due to electron-irradiation. *J. Mater. Res.*, 9(7):1899–1907, July 1994.

[40] H. W. Kroto, J. R. Heath, S. C. O'Brien, R. F. Curl, and R. E. Smalley. C60: Buckminsterfullerene. *Nature*, 318:162–163, 1985.

[41] T. Tanabe, S. Muto, and K. Niwase. On the mechanism of dimensional change of neutron irradiated graphite. *Appl. Phys. Lett.*, 61(14):1638–1640, October 1992.

[42] G F Sun, J F Jia, Q K Xue, and L Li. Atomic-scale imaging and manipulation of ridges on epitaxial graphene on 6h-sic(0001). *Nanotechnology*, 20(35):355701, 2009.

[43] Hsiangpin. Chang and Allen J. Bard. Observation and characterization by scanning tunneling microscopy of structures generated by cleaving highly oriented pyrolytic graphite. *Langmuir*, 7(6):1143–1153, 1991.

[44] Ke Xu, Peigen Cao, and James R. Heath. Scanning tunneling microscopy characterization of the electrical properties of wrinkles in exfoliated graphene monolayers. *Nano Letters*, 9(12):4446–4451, 2009.

[45] Chong Yang. Liu, Hsiangpin. Chang, and Allen J. Bard. Large scale hexagonal domainlike structures superimposed on the atomic corrugation of a graphite surface observed by scanning tunneling microscopy. *Langmuir*, 7(6):1138–1142, 1991.

[46] G. R. Hennig. Screw dislocations in graphite. *Science*, 147(3659):pp. 733–734, 1965.

[47] A. R. Patel and O. P. Bahl. Evidence of screw dislocations in graphite. *British Journal of Applied Physics*, 16(2):169, 1965.

[48] J. P. Hirth and J. Lothe. *Theory of dislocations*. Materials Science and Engineering. McGraw-Hill, New York, 1968.

[49] P. P. Ltd, S. i. Sawada, and N. Hamada. Energetics of carbon nano-tubes. *Solid State Commun.*, 83(11):917 – 919, 1992.

[50] Ya.I. Frenkel and T.A. Kontorova. *zetf*, (8):1340, 1938.

[51] G. Pintsuk, W. K. hnlein, J. Linke, and M. R. dig. Investigation of tungsten and beryllium behaviour under short transient events. *Fusion Eng. Des.*, 82:1720 – 1729, 2007.

[52] O. V. Yazyev and S. G. Louie. Topological defects in graphene: dislocations and grain boundaries. *Phys. Rev. B*, 81(19):195420, May 2010.

[53] P. Delavignette and S Amelinckx. Dislocation Patterns in Graphite. *Journal of Nuclear Materials*, 5(1):17 – 66, 1962.

[54] C. P. Ewels, M. I. Heggie, and P. R. Briddon. Adatoms and nanoengineering of carbon. *Chem. Phys. Lett.*, 351(3-4):178–182, January 2002.

[55] C. Roscoe and J. M. Thomas. The identification and some physico-chemical consequences of non-basal edge and screw dislocations in graphite. *Proc. R. Soc. London, Ser. A*, 297(1450):397–407, March 1967.

[56] A. Hashimoto, K. Suenaga, A. Gloter, K. Urita, and S. Iijima. Direct evidence for atomic defects in graphene layers. *Nature*, 430(7002):870–873, August 2004.

[57] G. Schoeck. The core energy of dislocations. *Acta metall. mater.*, 43(10):3679 – 3684, 1995.

[58] A. K. Head. The monodromic galois groups of the sextic equation of anisotropic elasticity. *Journal of Elasticity*, 9(3):321 – 324, 1979.

[59] N. Lehto and S. Öberg. Interaction of vacancies with partial dislocations in silicon. *Phys. Rev. B*, 56(20):12706–12709, November 1997.

[60] J. R. K. Bigger, McInnes D. A., A. P. Sutton, M. C. Payne, I. Stich, R. D. King-Smith, D. M. Bird, and L. J. Clarke. Atomic and electronic structures of the 90° partial dislocation in silicon. *Phys. Rev. Lett.*, 69(15):2224–2227, 1992.

[61] W. W. Strong. X-ray diffraction patterns. *Science*, 40(1037):pp. 709–710, 1914.

[62] W. H. Bragg and W. L. Bragg. The reflection of x-rays by crystals. *Proceedings of the Royal Society of London. Series A*, 88(605):428–438, 1913.

[63] A. Oberlin, S. Bonnamy, and K. Oshida. Landmarks for graphitization. *Macromolecules*, 3(224):2006, 2006.

[64] G. Nanoribbons, K. V. Bets, and B. I. Yakobson. Spontaneous Twist and Intrinsic Instabilities of Pristine Graphene Nanoribbons. *Mater. Sci.*, 2, 2009.

[65] A. Asthana, Y. Matsui, M. Yasuda, K. Kimoto, T. Iwata, and K. Ohshima. Investigations on the structural disordering of neutron-irradiated highly oriented pyrolytic graphite by x-ray diffraction and electron microscopy. *J. Appl. Cryst.*, 38(2):361–367, April 2005.

[66] J.-M. Leyssale, J.-P. Da Costa, C. Germain, P. Weisbecker, and G. L. Vignoles. Structural features of pyrocarbon atomistic models constructed from transmission electron microscopy images. *Carbon*, May 2012. Accepted for publication.

[67] D. D. Dijulio and A. I. Hawari. Examination of reactor grade graphite using neutron powder diffraction. *Journal of Nuclear Materials*, 392(2):225–229, JUL 15 2009.

[68] Hui Li, ChuanZheng Yang, and Fang Liu. Novel method for determining stacking disorder degree in hexagonal graphite by x-ray diffraction. *Science in China Series B: Chemistry*, 52:174–180, 2009. 10.1007/s11426-009-0009-z.

[69] H. Shi, J. N. Reimers, and J. R. Dahn. Structure-refinement program for disordered carbons. *Journal of Applied Crystallography*, 26(6):827–836, Dec 1993.

[70] W. Bollmann. Electron-microscopic observations on radiation damage in graphite. *Phil. Mag.*, 5(54):621–624, June 1960.

[71] J.R. Hook and H.E. Hall. *Solid State Physics*. Wiley, second edition, 1991.

[72] T. Ungár. Microstructural parameters from X-ray diffraction peak broadening. *Scripta Mater.*, 51:777 – 781, 2004.

[73] W. T. Eeles. Diffuse diffraction phenomena from neutron-irradiated graphite single crystals. *ACA*, 24(6):688–689, Nov 1968.

[74] Sumio Iijima. Helical microtubules of graphitic carbon. *Nature*, 354:56–58, 1991.

[75] W. T. Eeles. Interpretation of the diffuse diffraction phenomena of neutron-irradiated graphite crystals. *Phil. Mag.*, 32(6):1273–1276, December 1975.

[76] www.crystalmaker.com.

[77] D. T. Keating and A. N. Goland. X-ray scattering from graphite crystals containing interstitial basal-plane loops. *Phys. Rev. B*, 10(6):2232–2245, September 1974.

[78] S. M. Ohr. Anisotropic elasticity of a prismatic dislocation loop in a hexagonal crystal. *J. Appl. Phys.*, 43(4):1361–1365, April 1972.

[79] A. N. Kolmogorov and V. H. Crespi. Registry-dependent interlayer potential for graphitic systems. *Phys. Rev. B*, 71(23):235415, June 2005.

[80] R. H. Telling and M. I. Heggie. Stacking fault and dislocation glide on the basal plane of graphite. *Phil. Mag. Lett.*, 83(7):411–421, July 2003.

[81] Matthew J. Allen, Minsheng Wang, Sergio A. V. Jannuzzi, Yang Yang, Kang L. Wang, and Richard B. Kaner. Chemically induced folding of single and bilayer graphene. *Chem. Commun.*, pages 6285–6287, 2009.

[82] J. Zhang, J. Xiao, X. Meng, C. Monroe, Y. Huang, and J.-M. Zuo. Free folding of suspended graphene sheets by random mechanical stimulation. *Phys. Rev. Lett.*, 104(81), 2010.

[83] Kwanpyo Kim, Zonghoon Lee, Brad D. Malone, Kevin T. Chan, Benjamín Alemán, William Regan, Will Gannett, M. F. Crommie, Marvin L. Cohen, and A. Zettl. Multiply folded graphene. *Phys. Rev. B*, 83:245433, Jun 2011.

[84] Xiaodong Zou, Sven Hovmoller, and Peter Oleynikov. *Electron Crystallography: Electron Microscopy and Electron Diffraction.* Oxford University Press, 2011.

[85] K. S. Novoselov, A. K. Geim, S. V. Morozov, D. Jiang, M. I. Katsnelson, I. V. Grigorieva, S. V. Dubonos, and A. A. Firsov. Two-dimensional gas of massless Dirac fermions in graphene. *Nature*, 438(7065):197–200, November 2005.

[86] S. J. Coleman and R. Van Noorden. The Trials of new carbon. *Nature*, 469:14–16, 2011.

[87] D. Toma´nek, W. Zhong, and E. Krastev. Stability of multishell fullerenes. *Phys. Rev. B*, 48:15461–15464, Nov 1993.

[88] Y. Huang, J. Wu, and K. C. Hwang. Thickness of graphene and single-wall carbon nanotubes. *Phys. Rev. B*, 74(61):245413, 2006.

[89] F. Scarpa, S. Adhikari, A. J. Gil, and C. Remillat. The bending of single layer graphene sheets: The lattice versus continuum approach. *Science*, 21:125702, 2010.

[90] B. Yang and V. K. Tewary. Multiscale Green's function for the deflection of graphene lattice. *Phys. Rev.*, 77(62):245442, 2008.

[91] Qiang Lu and Rui Huang. Nonlinear mechanics of single-atomic-layer

graphene sheets. *International Journal of Applied Mechanics*, 01(03):443–467, 2009.

[92] G. Haffenden. *ab intio* modelling of carbon nanotubes. unpublished, 2009.

[93] Y. Gogotsi and S. V. Rotkin. Analysis of non-planar graphitic structures: From arched edge planes of graphite crystals to nanotubes. *Mat Res Innovat*, 5:191 – 200, 2002.

[94] Y. Gogotsi and et. al. Graphite Polyhedral Crystals. *Science*, 290:317, 2000.

[95] L. D. Landau and E. M. Lifshiz. *The classical theory of fields.* Pergamon Press, Oxford, 1975.

[96] S. Timoshenko & J.N. Goodier. *Theory of Elasticity.* McGraw-Hill, New York, 1951.

[97] L. Spanu, S. Sorella, and G. Galli. Nature and strength of interlayer binding in graphite. *Phys. Rev. Lett.*, 103(19):196401, November 2009.

[98] R. W. Lynch and H. G. Drickamer. Effect of high pressure on the lattice parameters of diamond, graphite, and hexagonal boron nitride. *The Journal of Chemical Physics*, 44(1):181–184, 1966.

[99] http://www.substech.com/dokuwiki/doku.php?id=boron_nitride_as_solid_lubricant.

[100] A. Zobelli. Private communication.